BEILSTEIN JOURNAL OF NANOTECHNOLOGY

Emerging technologies and nanomaterials for sustainability

Edited by Viet Van Pham and Hung Nguyen Xuan

Imprint

Beilstein Journal of Nanotechnology
www.bjnano.org
ISSN 2190-4286
Email: journals-support@beilstein-institut.de

The *Beilstein Journal of Nanotechnology* is published by the Beilstein-Institut zur Förderung der Chemischen Wissenschaften.

Beilstein-Institut zur Förderung der
Chemischen Wissenschaften
Trakehner Straße 7–9
60487 Frankfurt am Main
Germany
www.beilstein-institut.de

BEILSTEIN JOURNAL OF NANOTECHNOLOGY

Synthesis of a multicomponent cellulose-based adsorbent for tetracycline removal from aquaculture water

Uyen Bao Tran[1,2], Ngoc Thanh Vo-Tran[1,2], Khai The Truong[1,2], Dat Anh Nguyen[1,2], Quang Nhat Tran[1,2], Huu-Quang Nguyen[3], Jaebeom Lee[3] and Hai Son Truong-Lam*[1,2]

Full Research Paper

Address:
[1]Faculty of Chemistry, University of Science, Ho Chi Minh City 70000, Vietnam, [2]Vietnam National University, Ho Chi Minh City 70000, Vietnam and [3]Department of Chemistry, Chungnam National University, Daejeon 34134, Republic of Korea

Email:
Hai Son Truong-Lam* - tlshai@hcmus.edu.vn

* Corresponding author

Keywords:
adsorption; aquaculture water; removal efficiency; response surface methodology; tetracycline antibiotic

Beilstein J. Nanotechnol. **2025,** *16,* 728–739.
https://doi.org/10.3762/bjnano.16.56

Received: 15 February 2025
Accepted: 09 May 2025
Published: 27 May 2025

This article is part of the thematic issue "Emerging technologies and nanomaterials for sustainability".

Guest Editor: V. V. Pham

Abstract

Excessive use of tetracycline (TC) antibiotics in aquaculture, particularly in Vietnam, has contributed to environmental contamination and economic losses. To address this problem, we developed a novel cellulose-based multicomponent adsorbent material (PGC) synthesized from sodium carboxymethyl cellulose and investigated factors influencing its TC adsorption capacity. The synthesis process was optimized using parameters derived from the response surface methodology. The surface and structural properties of PGC were characterized, and the TC adsorption efficiency of PGC was assessed using high-performance liquid chromatography–mass spectroscopy (HPLC-MS). Elemental analysis of PGC identified four key mechanisms governing its endothermic TC adsorption mechanism: surface complexation, electrostatic interactions, hydrogen bonding, and CH–π interactions, with surface complexation between Ca^{2+} and TCs being dominant. Batch adsorption experiments conducted to examine the factors influencing adsorption capacity revealed that PGC achieved up to 70% TC removal efficiency at an adsorbent dosage of 40 mg and an initial TC concentration of 60 $mg \cdot L^{-1}$ at pH 6–7, reaching equilibrium after 12 h. The surface characteristics and structural properties of PGC were determined using various material characterization techniques, including FTIR, SEM, EDX, and BET. Verification experiments under optimal conditions confirmed that the adsorption process followed second-order kinetics and the Langmuir adsorption isotherm model. Under optimal experimental conditions, a maximum adsorption capacity (q_m) of 123.2 $mg \cdot g^{-1}$ was estimated using the Langmuir isotherm model. These findings indicate that PGC demonstrates strong potential as an effective adsorbent for the removal of average 70% TC antibiotic residues, particularly oxytetracycline, chlortetracycline, TC, and doxycycline.

Introduction

The aquaculture industry plays a crucial role in the global economy, particularly for coastal nations, including Vietnam. However, its multibillion dollar contributions are accompanied by the growing problem of excess antibiotic usage, notably tetracyclines (TCs), a widely used class of antibiotics in recent years [1-4]. Recent studies indicate that oxytetracycline (OTC), a TC derivative, is the predominant antibiotic used in Vietnam's white leg shrimp farming industry, particularly during the 10–30 day and 30–45 day rearing periods [5]. The extensive use of OTC is primarily attributed to its broad-spectrum activity, rendering it effective in controlling various bacterial infections in shrimp. However, unregulated antibiotic usage poses significant risks, including the presence of antibiotic residues in seafood, which threaten human health. More broadly, overuse of antibiotics diminishes aquatic biodiversity and leads to substantial economic losses.

Nowadays, various methods, including adsorption, biological processing, photocatalysis, and electrochemical methods, have been used to remove antibiotics from contaminated water. However, these conventional treatment methods are restricted by costs, prolonged treatment durations, low adsorption efficiency, water matrices, and secondary pollutant formation, limiting their overall efficiency. A promising method for tackling tetracycline antibiotics involves membrane technologies such as osmosis membrane technology [6,7]. However, this approach presents significant upfront investment and recurring maintenance costs, while the contents of organic material and dissolved salts significantly affect the function of the membranes. Furthermore, challenges related to the draw solution and the necessity for integrating additional membrane processes for its regeneration remain key hurdles. Photochemical processes have also garnered significant research interest for tetracycline antibiotic removal, leveraging UV radiation [8,9]. While this approach offers cost-effectiveness, simplicity, and environmental benefits, its efficacy is strongly influenced by the compound's adsorption spectrum, the sample matrix, and the radiation intensity. Activated carbon is a conventional approach [10,11], however, a major drawback of activated carbon is its incomplete recovery after adsorption. Because adsorption primarily relies on physical interactions such as hydrogen bonding interactions, electrostatic forces, and van der Waals forces, adsorbed antibiotics may desorb and reenter aquatic environments [12]. Moreover, activated carbon exhibits low selectivity and adsorption capacity. Among novel adsorbents, metal-organic frameworks [13] and molecularly imprinted polymers (MIPs) [14] are particularly notable for their high target specificity. Although MIPs are effective, their synthesis requires exceptional precision and is time-intensive. Meanwhile, magnetic solid-phase extraction columns [15] have been explored for TC removal; however, they are impractical for processing large sample volumes. These limitations have spurred the development of more effective and versatile adsorbents.

Modern adsorbents are available in diverse compositions. Moreover, they are easy to manufacture and generally both cost-effective and environmentally friendly. Cellulose-based adsorbents, in particular, have garnered increasing attention in recent years. For instance, Yao et al. used three-dimensional cellulose-based materials to remove various antibiotics from water, including TC, exhibiting high adsorption capacity and good reusability [16]. Moreover, three-dimensional cellulose-based aerogels, which feature high porosity and a large specific surface area, have demonstrated adsorption efficiency across a wide pH range [17].

Although previous studies have offered valuable insights, further research is needed to optimize the structural and compositional properties of materials to improve their performance. For instance, carboxymethyl cellulose (CMC), an anionic derivative of cellulose, is a linear polysaccharide consisting of anhydroglucose units linked by β-1,4-glycosidic bonds. The key distinction between CMC and cellulose is that some hydroxy groups in cellulose are replaced by carboxymethyl ($-CH_2COOH$) groups. The introduction of carboxymethyl groups greatly enhances the water solubility of CMC relative to that of cellulose. CMC, recognized as one of the most promising cellulose derivatives, was first synthesized in 1918 [18]. Owing to its unique surface properties, high mechanical strength, abundance of raw materials, and cost-effective synthesis, CMC is now widely used in food, textile, pharmaceutical, and wastewater treatment industries.

This study aims to synthesize a cellulose-based multicomponent adsorbent material (PGC) using commercial sodium CMC, cross-linked with glutaraldehyde (GA) and polyvinyl alcohol (PVA); and cationized with Ca^{2+} and Zn^{2+} for the removal of TC from aquaculture effluents. Our approach involves optimizing the material's synthesis using the response surface methodology, and a wide range of characterization methods was performed to assess the surface characteristics and morphology of the synthesized adsorbent. Additionally, the study examines the adsorption mechanism of TC on the material's surface and evaluates the effects of pH value, adsorbent dosage, and matrix composition.

As a biodegradable and easily recoverable material derived from natural cellulose, this adsorbent offers a sustainable alternative to synthetic materials that pose environmental risks. In addition to wastewater treatment, this material could be utilized in medicine, pharmaceuticals, air purification, and environmental monitoring.

Results and Discussion

Experimental optimization

Conventional production and modification methods typically involve the manipulation of a single independent variable while holding all other variables constant [19]. However, chemical processes frequently involve a multitude of interacting factors, necessitating the simultaneous evaluation of potential interrelationships. To address this challenge, statistical experimental design methodologies, notably response surface methodology (RSM), have been developed. RSM, a robust integration of mathematical and statistical techniques, is extensively employed for process optimization and the elucidation of interactions among experimental variables, ultimately leading to enhanced results [20,21]. The application of RSM enables researchers to substantially decrease the number of experiments needed while simultaneously achieving a more thorough comprehension of the process under investigation and the identification of optimal operating parameters.

A response surface plot (Figure 1) was used to visualize variable interactions and determine optimal process parameters. As depicted in Figure 1a, the TC removal efficiency of the adsorbent decreases when both CMC mass (X1) and PVA mass (X2) increase simultaneously. This decline is expected, as increasing both CMC and PVA concentrations results in a highly viscous and non-homogeneous mixture, which deteriorates material quality and reduces adsorption capacity. When evaluating X2 independently, the optimal PVA concentration is determined to be below 2.0 g. When the PVA concentration exceeds this threshold, TC adsorption efficiency declines. This is because higher PVA levels hinder dissolution and mixing, particularly as viscosity increases. Similarly, TC adsorption efficiency also declines as GA concentration increases. At high concentrations, GA can dissolve PVA, compromising the material's stability. This interaction significantly influences the model (p-value < 0.05), particularly through the GA volume (X3). The interaction of the mole ratio between Ca^{2+} and Mg^{2+} (X4) with other factors also has a significant effect on the model, yielding an optimal value of approximately 0.1. A substantial decrease in X4 leads to a corresponding decline in the dependent variable Y, particularly in the X1–X4 and X3–X4 interactions. This effect arises because a reduction in X4 decreases water solubility and hinders the formation of a homogeneous cellulose mixture. Additionally, lower Ca^{2+} concentrations impede chelate formation between Ca^{2+} and TC (Figure 1b). Response surface methodology (RSM) optimization in MODDE 5.0 identified the following optimal values for maximizing the objective function: X1 = 1.5 g, X2 = 1.0 g, X3 = 0.01 mL, and X4 = 0.1. These optimized parameters will be applied in the synthesis of an adsorbent for TC removal from water.

Material characterization

FE-SEM and FTIR results

Figure 2 presents comparative field-emission SEM (FE-SEM) images and FTIR spectra of commercial CMC and PGC. Notably, the FE-SEM analysis of PGC (Figure 2d–f) reveals significant morphological changes compared to pristine CMC (Figure 2a–c). Specifically, the PGC surface exhibits numerous, uniformly distributed spherical nanoparticles (≈200 nm in diam-

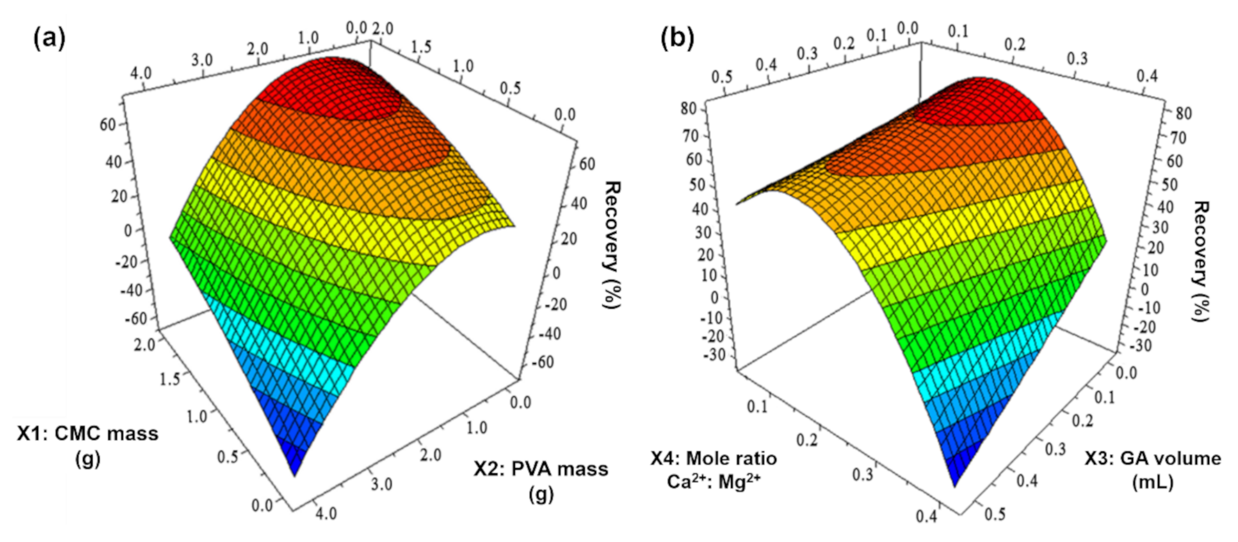

Figure 1: Response surface methodology (RSM) plots for synthesis optimization. (a) RSM plot showing the effect of X1 (CMC mass), X2 (PVA mass) and (b) RSM plot showing the effect of X3 (mole ratio Ca^{2+}/Mg^{2+}) and X3 (GA volume) on the optimum efficiency of the synthesis.

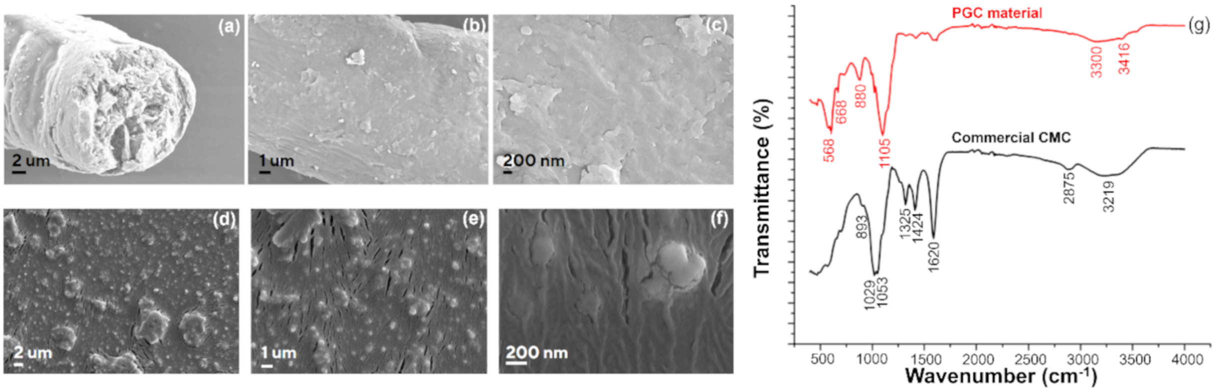

Figure 2: (a–c) FE-SEM images of commercial CMC, (d–f) FE-SEM images of PGC, and (g) FTIR spectra of commercial CMC and PGC.

eter), attributed to ZnO nanoparticles. The initial tubular structure of CMC is converted into a film-like structure owing to the lateral bonding effect of GA and PVA, as well as the dissolution of cellulose by Zn^{2+}. The rough, wrinkled surface and cracks are likely due to the focused high-energy electron beam during the FE-SEM imaging process [22]. Larger agglomerates, possibly $ZnSO_4$ residues, are also apparent, which aligns with the subsequent EDX results.

The FTIR spectrum (Figure 2g) of commercial CMC displays distinct adsorption bands at 3219, 2875, 1424, 1325, 1053, 1029 and 893 cm^{-1}. The broad band from 3219 to 3406 cm^{-1} corresponds to O–H stretching vibrations, reflecting the abundance of hydroxy and carboxyl groups in commercial CMC. The adsorption band at 2875 cm^{-1} represents symmetric stretching vibrations of the $–CH_2$ group. The strong peak at 1620 cm^{-1} likely corresponds to asymmetric C=O stretching vibrations in carboxyl groups such as –COONa. The sharp, symmetric peaks at 1424 and 1325 cm^{-1} correspond to symmetric stretching vibrations of alkyl groups in CMC. The doublet at 1029 and 1053 cm^{-1} represents vibrations of pyranose rings formed during cellulose synthesis, as well as C–O stretching vibrations. Meanwhile, the peak at 893 cm^{-1} corresponds to C–O–C stretching vibrations, which are characteristic of cellulose. These results are consistent with previous findings on commercial CMC [23,24].

Owing to lateral bonding, the characteristic peaks of CMC remain observable but exhibit shifts. For example, the alkyl group vibration peak shifts to 1424 cm^{-1}, while the C–O–C stretching vibration peaks shift to 883 and 1105 cm^{-1}. Meanwhile, the hydroxy group vibration peak becomes broader and less intense, shifting to the 3240–3386 cm^{-1} region, suggesting the involvement of –OH groups in cross-linking. The intensity of the peak at 1325 cm^{-1} decreases significantly, while the peak at 1620 cm^{-1}, corresponding to carbonyl (–C=O) stretching in carboxyl groups, nearly disappears, indicating lateral bonding between PVA and GA. Additionally, the appearance of the peak at 668 cm^{-1} indicates the presence of a Zn–O bond, while the peaks at 880 and 3416 cm^{-1} correspond to Zn–OH vibrations, suggesting the involvement of Zn^{2+} in dissolving CMC. The sharp peak at 568 cm^{-1} corresponds to a Ca–O bond [25].

EDX

EDX analysis revealed the elemental composition of the PGC material, as detailed in Figure 3a,b. Notably, the detection of elements, particularly Zn, in PGC confirms the role of Zn^{2+} ions in cellulose dissolution via hydrate bridge formation. Additionally, the presence of Zn enhances the TC adsorption capacity of PGC through a chemical adsorption mechanism.

According to our findings, Zn content increased significantly from 12.45% in pristine CMC to 22.24% in PGC, aligning with FTIR outcomes confirming the presence of Zn–O and Zn–OH bonds. Furthermore, the Ca content increased from 0.03% to 2.82%, accompanied by a rise in oxygen content. This increase suggests the involvement of GA and PVA in the cross-linking process, where the –OH groups in PVA and –CHO groups in GA contribute to the rise in oxygen content. Additionally, the detection of sulfur in PGC indicates the potential presence of residual $ZnSO_4$ precursor. Figure 3c–l present significant changes in the elemental distribution of O, S, Zn, and Ca in PGC compared to pristine CMC. These elements display a higher density on the surface of PGC.

Brunauer–Emmett–Teller method

Surface area characterizations of PGC determinded by the Brunauer–Emmett–Teller (BET) method are shown in Table 1. Specifically, the specific surface area of PGC is 1.3543 $m^2 \cdot g^{-1}$; the pore volume is 0.000641 $cm^3 \cdot g^{-1}$ and the average pore diameter is 18.93 Å.

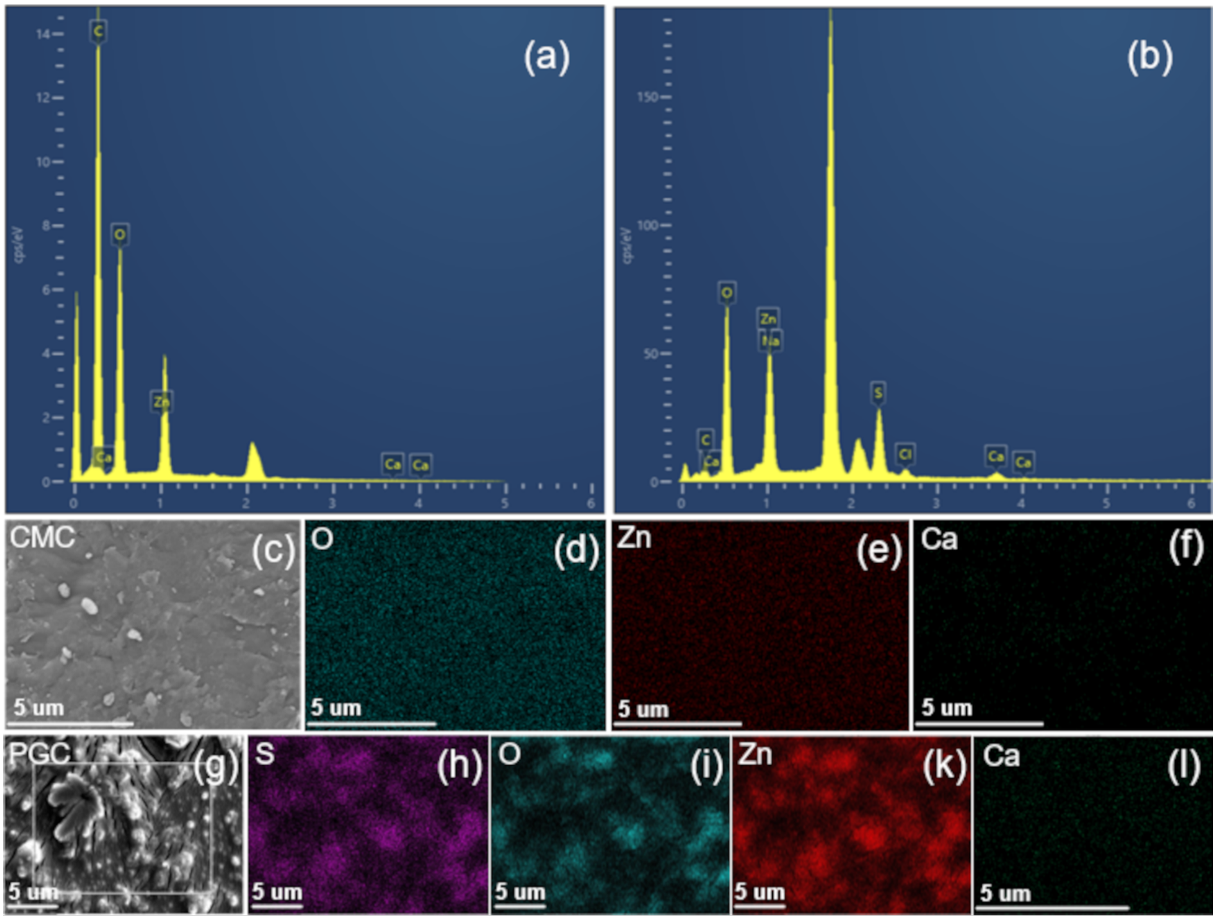

Figure 3: (a, b) EDX spectra and elemental compositions of commercial CMC and PGC, respectively; (c) morphology image of CMC; (d–f) elemental mapping images of commercial CMC; (g) morphology image of PGC; and (h–l) elemental mapping images of PGC.

Table 1: Surface area characterizations of PGC determinded by BET method.

Surface area (m^2/g)	
Single point surface area at P/P_0 = 0.249674088	1.2965
BET surface area	1.3543
t-Plot micropore area	0.2295
t-Plot external surface area	1.1248
Pore volume (cm^3/g)	
Single point adsorption total pore volume of pores less than 34.994 Å diameter at P/P_0 = 0.398928826	0.000641
t-Plot micropore volume	0.000101
BJH adsorption cumulative volume of pores between 17.000 Å and 3,000.000 Å diameter	0.000461
Pore size (Å)	
Adsorption average pore diameter	18.930
BJH adsorption average pore diameter	20.758

Investigation of factors influencing the maximum TC adsorption capacity of the synthetic material

Effect of initial pH

The effect of pH on the TC adsorption capacity of PGC is illustrated in Figure 4c. Specifically, the adsorption capacity increases significantly between pH 3 and 7, peaking at pH 7. Beyond this point, it decreases rapidly, with the sharpest decline observed between pH 10 and 11.

This occurs because, as pH increases, particularly around pH 6.8, keto-enol groups serve as preferential sites for chelate formation between TC and Ca^{2+} in a 1:3 ratio of Ca^{2+} to TC [26]. In this pH range, reduced competition between H^+ ions and TC for adsorption sites, along with the ionization of hydroxy groups and the subsequent formation of hydrogen bonds with TC molecules, results in a rapid increase in adsorption capacity. Beyond pH 7, adsorption capacity decreases sharply as TC transforms into negatively charged anions, causing repulsive interactions with oxygen-containing functional groups on the PGC surface.

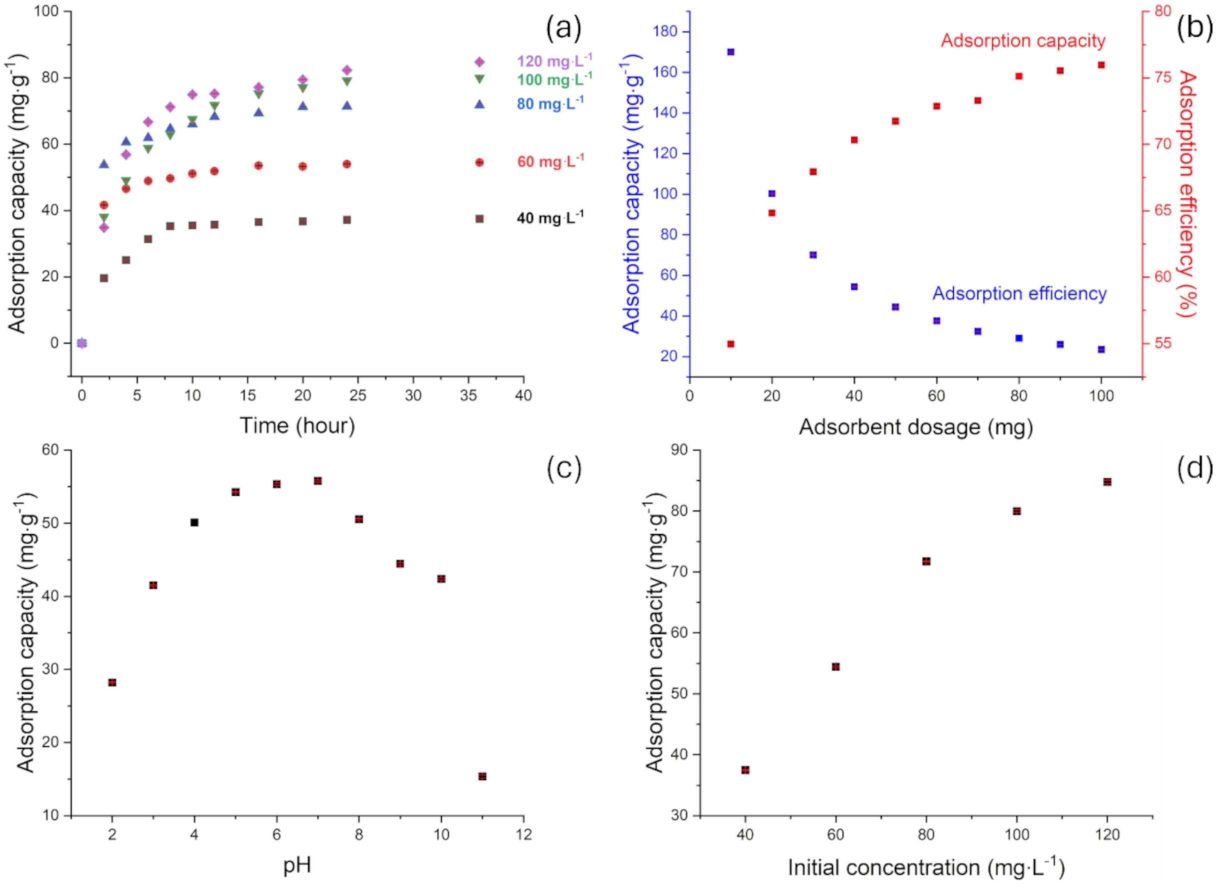

Figure 4: (a) Effect of adsorption time and initial concentration on the adsorption capacity of PGC. (b) Effect of adsorbent dosage on the adsorption capacity and adsorption efficiency of PGC. (c) Effect of pH on the adsorption capacity of PGC. (d) Effect of initial concentration on the adsorption capacity of PGC.

Further, at pH 7.5 and above, the chelate complex between Ca^{2+} and TC preferentially forms at a 1:1 ratio [27]. Hence, the pH range between 6 and 7 is selected as optimal for TC adsorption and will be used in subsequent investigations.

Effect of initial TC concentration and time

As depicted in Figure 4a, the adsorption capacity (q_e) increases with higher initial concentrations of TC. Specifically, at low initial concentrations, adsorption capacity is low owing to the incomplete diffusion of TC molecules into the material structure. However, at higher initial concentrations, a larger concentration gradient drives TC diffusion into the PGC surface, resulting in a rapid increase in adsorption capacity. Notably, most of the adsorption occurs within the first 12 h, during which 89–95% of TC is adsorbed. In the first 8 h, the adsorption rate of TC increases rapidly at all concentrations but decreases significantly afterward. This occurs because, during the initial stage, numerous vacant adsorption sites on the surface allow for the easy adsorption of TC. As TC molecules fill the vacant adsorption sites, the adsorption rate decreases over time until equilibrium is reached after 12–16 h.

As depicted in Figure 4a, the adsorption efficiency at 60 mg·L^{-1} TC increases more rapidly in the first 12 h than at other concentrations. Therefore, a concentration of 60 mg·L^{-1} was selected for further investigations.

Effect of adsorbent dosage

An adsorption experiment was performed using 10 different adsorbent dosages at an initial TC concentration of 60 mg·L^{-1} and pH 6–7. Figure 4b presents the effect of adsorbent dosage on the TC adsorption capacity and efficiency of PGC. Notably, as the adsorbent dosage increases, TC adsorption capacity decreases, whereas adsorption efficiency improves owing to the greater surface area available for TC adsorption. Adsorption efficiency increases rapidly as the adsorbent dosage rises from 10 to 40 mg, but beyond this point, the rate of increase becomes negligible. Doubling the adsorbent dosage to 80 mg results in an increase of no more than 10% in both TC adsorption capacity and removal efficiency. However, the amount of TC adsorbed per unit mass of adsorbent decreases as dosage increases. Therefore, an adsorbent dosage of 40 mg is selected for subsequent studies.

Adsorption isotherms

An adsorption test was conducted at pH 6–7 using a 40 mg adsorbent dosage with varying initial TC concentrations. Linear regression analysis was applied to C_e/q_e and C_e for the Langmuir model (Figure 5a) and to ln q_e and ln C_e for the Freundlich model (Figure 5b). To assess whether TC adsorption onto PGC follows the monolayer adsorption mechanism described by the Langmuir model, the degree of fit was evaluated using the equilibrium coefficient R_L. Notably, the R_L values, calculated in Table 2 and presented in Figure 5c, range from 0.167 to 0.334, indicating that TC adsorption onto PGC is favorable and conforms to the Langmuir isotherm model.

The higher R^2 value for the Langmuir model compared to that for the Freundlich model (Table 2, Figure 5a,b) suggests that the Langmuir model better describes TC adsorption onto PGC. This finding indicates that TC adsorption onto PGC occurs as monolayer adsorption on a homogeneous surface.

Adsorption kinetics

Experimental data derived from the analysis of the effect of contact time and initial TC concentration on adsorption capacity were used to study the kinetics of TC adsorption using first-order and second-order kinetic models. Table 3 and Table 4 present the first-order and second-order kinetic equations, respectively. Although the first-order kinetic model yields relatively high R^2 values (0.89–0.98), the equilibrium adsorption capacity calculated based on the model equations deviates significantly from experimental values. Therefore, the first-order kinetic model is unsuitable for describing TC adsorption onto PGC.

Table 3: First-order kinetics equations and R^2 values.

Concentration (mg·L^{-1})	First-order kinetics equations	R^2
40	$y = -0.1850x + 3.0307$	0.9206
60	$y = -0.1651x + 3.0311$	0.8987
80	$y = -0.1951x + 3.6012$	0.9514
100	$y = -0.1746x + 4.2163$	0.9840
120	$y = -0.1285x + 3.9464$	0.9242

In contrast, the pseudo-second-order kinetic model exhibits high R^2 values (>0.99) and excellent agreement between calculated and experimental equilibrium adsorption capacities, indicating that it better describes TC adsorption onto PGC. This suggests that the adsorption process is predominantly chemisorption.

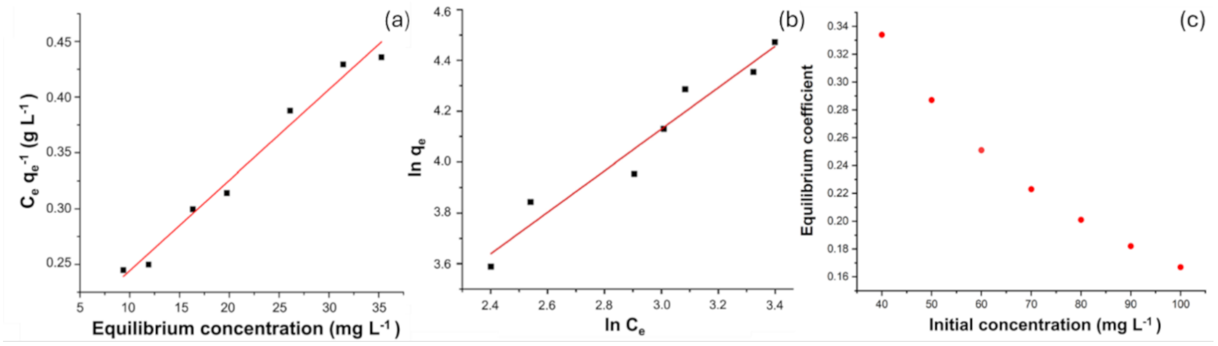

Figure 5: (a) Langmuir adsorption isotherms. (b) Freundlich adsorption isotherms. (c) Variation of the equilibrium constant R_L as a function of initial concentration.

Table 2: Characteristic parameters and R^2 coefficients of the Langmuir and Freundlich models according to the linearized models.

		Langmuir model				Freundlich model	
Adsorbent	R^2	q_m (mg·g^{-1})	K_L (L·mg^{-1})	R_L	R^2	K_F (L·g^{-1})	n
PGC	0.9823	123.2	0.05	0.167–0.334	0.9495	5.36	1.23

Table 4: Second-order kinetics equations and R^2 values.

Concentration (mg·L^{-1})	Second-order kinetics equations	R^2
40	$y = 0.0275x + 0.0303$	0.9971
60	$y = 0.0181x + 0.0113$	0.9995
80	$y = 0.0137x + 0.0103$	0.9992
100	$y = 0.0118x + 0.0245$	0.9946
120	$y = 0.0113x + 0.0212$	0.9952

Mechanism

Elemental analysis of the synthesized PGC material confirmed the presence of Ca^{2+}, indicating the potential formation of Ca^{2+}–TC complexes. Notably, the formation of these complexes depends on pH, as specific sites on the TC structure undergo protonation before ionic bonding with Ca^{2+} in the PGC matrix. Among the four ionizable functional groups in TC, the primary site remains predominantly protonated (86%) at pH 6.8 [26,28,29]. However, Ca^{2+} coordination at this site is expected to shift the ionization equilibrium toward the β-keto enolate form, leading to the deprotonation of TC molecules and complex formation with Ca^{2+}. Experimental results indicate that a 1:3 Ca^{2+}/TC complex is favored at pH 6.8 (Figure 6a) [29].

The adsorption mechanism of TC onto PGC is illustrated in Figure 6b,c,d. This mechanism involves van der Waals forces, which primarily represent electrostatic interactions. Notably, TC is an aromatic organic compound with an amino group that can accept protons (H^+) from the environment, acquiring a positive charge. The CMC network within PGC includes oxygen-containing functional groups (–OH, –C=O, and –COOH), which confer a negative charge, enabling electrostatic interactions (Figure 6b). FTIR spectroscopy (Figure 2g) confirms the presence of these oxygen-containing functional groups on PGC, supporting this explanation. Thus, electrostatic attraction between the positively charged TC–N$^+$ complex and the negatively charged PGC material drives the adsorption process. Additionally, hydroxy groups may facilitate hydrogen bond forma-

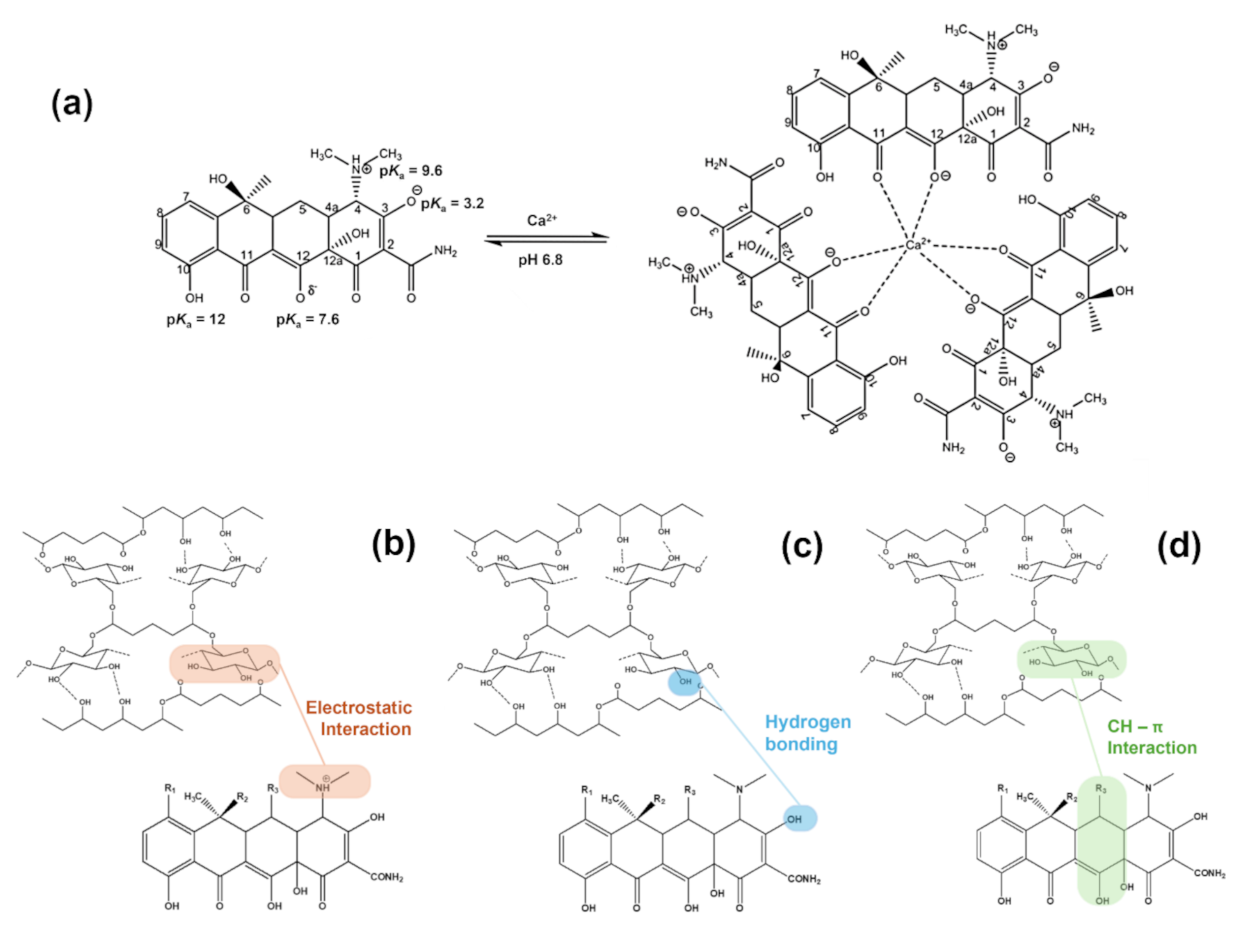

Figure 6: (a) Structure of the Ca^{2+}–TC complex formed at pH 6.8. Adsorption mechanism of TC onto the PGC surface through (b) electrostatic interaction, (c) hydrogen bonding, and (d) CH–π interaction.

tion between PGC and TC (Figure 6c). Furthermore, the aromatic ring of TC contains conjugated double bonds, while the hexagonal network of PGC contains –CH groups, enabling CH–π dispersion interactions [30] (Figure 6d).

Removal of antibiotics from water sample via PGC material

As shown in Table 5, approximately 70% and 60% of antibiotics content (including tetracyline (TC), oxytetracycline (OTC), chlortetracycline (CTC), and doxycycline (DOX)) in standard solution and sample solution, respectively, was successfully eliminated from water during a single-stage PGC treatment.

Table 5: Antibiotics treatment performance in water sample after one stage of the PGC process.

Matrix	Removal efficiency (%)	
standard solution	OTC	71.03 ± 0.96
	TC	72.24 ± 1.21
	CTC	82.68 ± 0.85
	DOX	86.98 ± 0.36
sample solution	OTC	46.07 ± 2.31
	TC	66.39 ± 0.52
	CTC	65.84 ± 1.53
	DOX	86.39 ± 0.67

PGC material ultilization promotes the valorization of agricultural waste, offering an effective strategy for its reuse, particularly relevant for agricultural countries like Vietnam. This provides an abundant and low-cost source of raw materials and mitigates environmental issues linked to the burning or improper handling of agricultural by-products. Notably, PGC also shows strong potential for commercialization as an efficient water treatment solution. Nonetheless, the presence of humic and fulvic acids in the sample matrix may interfere with the adsorption process, presenting a significant obstacle to the effective use of PGC for TC removal.

Conclusion

This study developed and implemented a synthesis strategy for a cellulose-derived adsorbent material (PGC) to remove TC antibiotics (tetracyline, oxytetracycline, chlortetracycline, and doxycycline) from aquaculture water. RSM was used to determine the optimal synthesis parameters for PGC, which were CMC mass (1.5 g), PVA mass (1.0 g), GA volume (0.01 mL), and Ca^{2+}/Zn^{2+} molar ratio (0.1). FTIR, EDX, FE-SEM, and BET analyses were used to assess the cross-linking performance of GA and PVA and to elucidate the role of Zn^{2+} in cellulose dissolution. The adsorption of TC onto PGC was explained by the formation of Ca^{2+}–TC chelate complexes, as well as electrostatic interactions, CH–π interactions, and hydrogen bonding interactions between the material surface and TC. Additionally, the effects of contact time, pH, initial concentration, and adsorbent dosage on the TC adsorption capacity of PGC were investigated. The results indicated that equilibrium was reached after 12 h, with an optimal pH of 6–7, an adsorbent dosage of 40 mg, and an initial concentration of 60 $mg{\cdot}L^{-1}$ TC. TC adsorption onto PGC followed pseudo-second-order kinetics and conformed to the Langmuir isotherm model. Additionally, preliminary tests in real water samples revealed that fulvic acid and humic acid in the water matrix affected the adsorption process. Owing to its high efficiency, eco-friendliness, versatility, and up to 70% removal efficiency of tetracyline, oxytetracycline, chlortetracycline, and doxycycline, the synthesized PGC material shows great potential for addressing environmental challenges and promoting sustainable development. The PGC adsorbent, with higher porosity, enhanced selectivity, more hydrophobicity, and a simple synthesis process, along with cost-efficiency and high adsorption capacity, holds promise as an effective adsorbent for the treatment of aquaculture wastewater. Overall, this study lays the groundwork for future research on synthesizing adsorbents from sustainable, cellulose-based materials derived from agricultural waste.

Experimental

Materials

Tetracycline hydrochloride (97.2%), oxytetracycline dihydrate (98%), and chlortetracycline hydrochloride (94.6%), all sourced from the Institute of Drug Quality Control, Ho Chi Minh City (Vietnam), were used as reference antibiotics in this study. Additional reagents included ciprofloxacin and enrofloxacin (both from Pharmaceutical Joint Stock Company of February 3rd, Vietnam), methanol (Merck, Germany), sodium carboxymethyl cellulose (Zhanyun, China), PVA (95.5–96.5% hydrolyzed, $M_W \approx 85{,}000–124{,}000$, Thermo Scientific Chemicals, USA), GA (50%) (Zhanyun, China), calcium chloride anhydrous (Xilong, China), and zinc sulfate heptahydrate (Xilong, China). All reagents were of analytical grade, and deionized water was used for all experiments.

Experimental optimization

MODDE 5.0 software was employed to identify key influencing factors and optimize the synthesis process using RSM. The independent variables included CMC mass (X1) [31], PVA mass (X2), and GA volume (X3) [32], along with the molar ratio of Ca^{2+} and Zn^{2+} (X4) [25].

Polyvinyl alcohol (PVA), characterized by a high density of hydroxy groups attached to its polymer chain, is widely used as a binding agent in material synthesis. PVA promotes chemical cross-linking between CMC molecules by interacting with acidic and/or basic functional groups under thermal conditions [33,34]. This cross-linking occurs when the polymer's free hydroxy groups interact with the functional groups of the cross-linking agent, reducing the polymer's water solubility while increasing its stiffness and chemical stability [35,36].

Glutaraldehyde (GA), a linear five-carbon dialdehyde, is regarded as a more effective cross-linking agent compared to monoaldehydes (e.g., formaldehyde) and other dialdehydes (C_2 to C_6) [37]. GA and PVA have been used as cross-linking agents in CMC-based materials to enhance selectivity, stability, and mechanical properties [38]. This method is both cost-effective and highly efficient in strengthening materials while improving their mechanical strength and hydrophobicity.

Recent studies have revealed that inorganic salt mixtures, such as zinc chloride and calcium chloride, effectively dissolve cellulose, facilitating the fabrication of cellulose membranes for gas separation and organic pollutant removal [38,39]. Specifically, in a cellulose solution, Ca^{2+} cross-linking with Zn–cellulose chains enhance the mechanical properties of the resulting membranes. These ions can be incorporated into the cellulose polymer matrix with an appropriate ratio, forming a controlled hydrogen bonding network that strengthens connectivity in the overall polymer network [40].

Preparation of PGC

As illustrated in Figure 7, CMC was selected as the base material for the synthesis of PGC, in combination with the presence of the following agents: PVA, which acts as a binder by facilitating chemical cross-linking of CMC molecules through interactions with functional acidic and basic groups, the cross-linking agent glutaraldehyde (GA), and an inorganic ion mixture (Ca^{2+} and Zn^{2+}), which enhances the mechanical properties of the material by promoting the formation of a controlled hydrogen bonding network, thereby reinforcing the polymer matrix. To prepare PGC, 1.5 g of CMC, 0.25 g of $CaCl_2$, and 3.637 g of $ZnSO_4$ were added to a beaker containing 30 mL of distilled water, where they were completely dissolved under magnetic stirring at 800 rpm for 30 min, forming solution A. Subsequently, 1.0 g of PVA and 0.1 mL of 1% H_2SO_4 were added, and the solution was stirred until a homogeneous mixture was obtained. Next, 0.01 mL of GA was added, and the stirring speed was increased to 1,000 rpm, continuing for 4 h. Finally, the solution was dried at 65 °C for 24 h, yielding the PGC adsorbent material for further use.

Characterization of PGC

FE-SEM and EDX

Field-emission SEM analysis was performed using a Merlin Compact instrument (Carl Zeiss, Jena, Germany) with an SE2 detector. The sample was mounted on a clean silicon wafer and coated with a nanoscale platinum layer using an ion sputter coater (Q150T Plus, Quorum Technologies, UK). EDX analysis was conducted using an Aztec Energy X-MaxN system (Oxford Instruments, UK) at an acceleration voltage of 5 kV and a working distance of 8.5 mm.

FTIR

FTIR analysis was performed using a Spectrum Two FTIR spectrometer (PerkinElmer, MA, USA) equipped with a $LiTaO_3$ detector and an attenuated total reflectance sampling accessory. The scanning range was 400–4000 cm^{-1}, with a total acquisition time of 60 s.

Brunauer–Emmett–Teller method

A 0.27 g PGC sample was analyzed at the Institute of Chemical Technology, Ho Chi Minh City, over 3 h. The specific surface area of this sample was determined using N_2 adsorption–desorption isotherms at 77.3 K under controlled pressure conditions. Before analysis, the sample was degassed at 150 °C for 2 h and 30 min under an N_2 atmosphere.

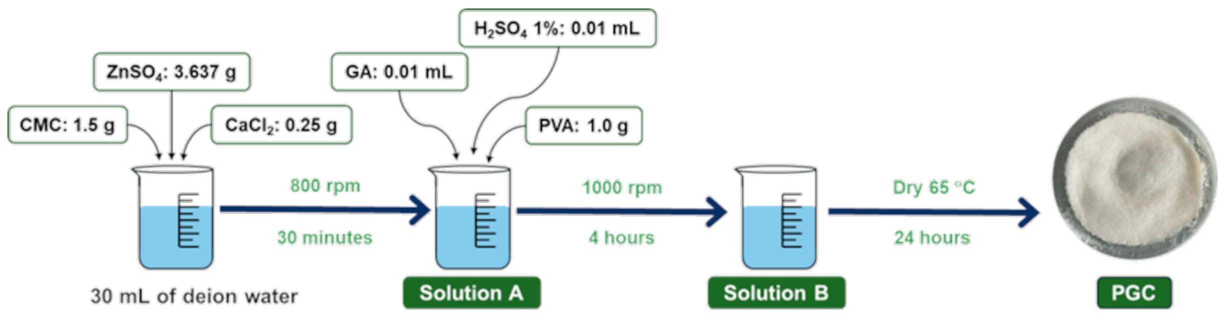

Figure 7: Synthesis procedure for PGC.

High-performance liquid chromatography-mass spectroscopy (HPLC–MS/MS)

The HPLC-MS/MS system consisted of an AB Sciex 4000 QTRAP mass spectrometer equipped with a Turbo Ion Spray source, which was operated in both positive mode and negative mode (QTRAP®4000, AB SCIEX, Framingham, MA, USA). The analyses of the tetracyclines were performed using a Sunfire C18 column (150 × 2.1 mm i.d., 5.0 mm particle size) from Waters (Milford, MA, USA), and the mobile phase consisted of ACN and 0.1% FA, delivered at 0.25 $\text{mL}\cdot\text{min}^{-1}$.

Factors influencing adsorption capacity

Experiments were conducted to evaluate factors affecting the adsorption capacity of PGC and determine optimal conditions. The investigated factors included initial pH, initial concentration and time, adsorbent dosage, adsorption isotherms, and adsorption kinetics.

Funding

This work was supported by the National Research Foundation of Korea (NRF), grant funded by the Korea government (MSIT) number RS-2023-00219710 and RS-2024-00333541. This research is funded by the University of Science, VNU-HCM, under grant number T2024-112.

Author Contributions

Uyen Bao Tran: data curation; formal analysis; investigation; methodology; validation; writing – original draft; writing – review & editing. Ngoc Thanh Vo-Tran: formal analysis; investigation; writing – original draft; writing – review & editing. Khai The Truong: formal analysis; investigation; writing – original draft; writing – review & editing. Dat Anh Nguyen: formal analysis; investigation; writing – original draft; writing – review & editing. Quang Nhat Tran: conceptualization; formal analysis; investigation; methodology; validation; writing – review & editing. Huu-Quang Nguyen: conceptualization; formal analysis; investigation; methodology; resources; writing – review & editing. Jaebeom Lee: conceptualization; formal analysis; funding acquisition; writing – review & editing. Hai Son Truong-Lam: conceptualization; data curation; formal analysis; investigation; methodology; supervision; validation; writing – original draft; writing – review & editing.

ORCID® iDs

Uyen Bao Tran - https://orcid.org/0009-0007-1621-4459
Huu-Quang Nguyen - https://orcid.org/0000-0002-8609-3038
Hai Son Truong-Lam - https://orcid.org/0000-0003-2435-6039

Data Availability Statement

The data collected during the current study will be available from the corresponding author on reasonable request.

Preprint

A non-peer-reviewed version of this article has been previously published as a preprint: https://doi.org/10.3762/bxiv.2025.9.v1

References

1. Luu, Q. H.; Nguyen, T. B. T.; Nguyen, T. L. A.; Do, T. T. T.; Dao, T. H. T.; Padungtod, P. *Aquacult. Rep.* **2021,** *20,* 100711. doi:10.1016/j.aqrep.2021.100711
2. Holmström, K.; Gräslund, S.; Wahlström, A.; Poungshompoo, S.; Bengtsson, B.-E.; Kautsky, N. *Int. J. Food Sci. Technol.* **2003,** *38,* 255–266. doi:10.1046/j.1365-2621.2003.00671.x
3. Phillips, M. The use of chemicals in carp and shrimp aquaculture in Bangladesh, Cambodia, Lao PDR, Nepal, Pakistan, Sri Lanka and Viet Nam. In *Use of Chemicals in Aquaculture in Asia: Proceedings of the Meeting on the Use of Chemicals in Aquaculture in Asia,* Tigbauan, Iloilo, Philippines, May 20–22, 1996; Arthur, J. R.; Lavilla-Pitogo, C. R.; Subasinghe, R. P., Eds.; Aquaculture Department, Southeast Asian Fisheries Development Center, 2000; pp 75–86. http://hdl.handle.net/10862/605
4. Long, L. M.; Brix, H.; Huong, D. T. T.; Trang, N. T. D. *J. Sci. Technol.* **2014,** *52,* 330–335.
5. Tuan, L. C.; Loc, N. H.; Hoa, T. T.; Son, T. M.; Chi, L. T. T.; Chau, M. N.; Tuan, T. N.; Chi, L. T. P.; Khoi, P. Q. A.; Dan, T. V. *Hue Univ. J. Sci.: Agric. Rural Dev.* **2021,** *130,* 131–145. doi:10.26459/hueunijard.v130i3d.6181
6. Pan, S.-F.; Zhu, M.-P.; Chen, J. P.; Yuan, Z.-H.; Zhong, L.-B.; Zheng, Y.-M. *Sep. Purif. Technol.* **2015,** *153,* 76–83. doi:10.1016/j.seppur.2015.08.034
7. Košutić, K.; Dolar, D.; Ašperger, D.; Kunst, B. *Sep. Purif. Technol.* **2007,** *53,* 244–249. doi:10.1016/j.seppur.2006.07.015
8. Jiao, S.; Zheng, S.; Yin, D.; Wang, L.; Chen, L. *Chemosphere* **2008,** *73,* 377–382. doi:10.1016/j.chemosphere.2008.05.042
9. Kim, I.; Yamashita, N.; Tanaka, H. *J. Hazard. Mater.* **2009,** *166,* 1134–1140. doi:10.1016/j.jhazmat.2008.12.020
10. Takdastan, A.; Mahvi, A. H.; Lima, E. C.; Shirmardi, M.; Babaei, A. A.; Goudarzi, G.; Neisi, A.; Heidari Farsani, M.; Vosoughi, M. *Water Sci. Technol.* **2016,** *74,* 2349–2363. doi:10.2166/wst.2016.402
11. Pouretedal, H. R.; Sadegh, N. *J. Water Process Eng.* **2014,** *1,* 64–73. doi:10.1016/j.jwpe.2014.03.006
12. Fu, H.; Li, X.; Wang, J.; Lin, P.; Chen, C.; Zhang, X.; Suffet, I. H. (Mel). *J. Environ. Sci.* **2017,** *56,* 145–152. doi:10.1016/j.jes.2016.09.010
13. Pang, Y.-H.; Lv, Z.-Y.; Sun, J.-C.; Yang, C.; Shen, X.-F. *Food Chem.* **2021,** *355,* 129411. doi:10.1016/j.foodchem.2021.129411
14. Sánchez-Polo, M.; Velo-Gala, I.; López-Peñalver, J. J.; Rivera-Utrilla, J. *Microporous Mesoporous Mater.* **2015,** *203,* 32–40. doi:10.1016/j.micromeso.2014.10.022
15. Tang, H.-z.; Wang, Y.-h.; Li, S.; Wu, J.; Gao, Z.-x.; Zhou, H.-y. *J. Food Sci. Technol.* **2020,** *57,* 2884–2893. doi:10.1007/s13197-020-04320-w
16. Yao, Q.; Fan, B.; Xiong, Y.; Jin, C.; Sun, Q.; Sheng, C. *Sci. Rep.* **2017,** *7,* 45914. doi:10.1038/srep45914
17. Chen, M.; Yan, Z.; Luan, J.; Sun, X.; Liu, W.; Ke, X. *Chem. Eng. J.* **2023,** *454,* 140300. doi:10.1016/j.cej.2022.140300
18. Heinze, T.; Pfeiffer, K. *Angew. Makromol. Chem.* **1999,** *266,* 37–45. doi:10.1002/(sici)1522-9505(19990501)266:1<37::aid-apmc37>3.0.co;2-z
19. Bezerra, M. A.; Santelli, R. E.; Oliveira, E. P.; Villar, L. S.; Escaleira, L. A. *Talanta* **2008,** *76,* 965–977. doi:10.1016/j.talanta.2008.05.019

20. Şener, M.; Reddy, D. H. K.; Kayan, B. *Ecol. Eng.* **2014,** *68,* 200–208. doi:10.1016/j.ecoleng.2014.03.024
21. Rathika, R.; Byung-Taek, O.; Vishnukumar, B.; Shanthi, K.; Kamala-Kannan, S.; Janaki, V. *e-Polym.* **2018,** *18,* 287–295. doi:10.1515/epoly-2017-0215
22. Joy, D. C. *Microsc. Microanal.* **2003,** *9* (Suppl. 2), 1556–1557. doi:10.1017/s1431927603447788
23. Chen, M.; Yan, Z.; Luan, J.; Sun, X.; Liu, W.; Ke, X. *Chem. Eng. J.* **2023,** *454,* 140300. doi:10.1016/j.cej.2022.140300
24. Ning, J.; Luo, X.; Wang, F.; Huang, S.; Wang, J.; Liu, D.; Liu, D.; Chen, D.; Wei, J.; Liu, Y. *Sensors* **2019,** *19,* 5482. doi:10.3390/s19245482
25. Tanpure, S.; Ghanwat, V.; Shinde, B.; Tanpure, K.; Lawande, S. *Polycyclic Aromat. Compd.* **2022,** *42,* 1322–1340. doi:10.1080/10406638.2020.1776740
26. Leeson, L. J.; Krueger, J. E.; Nash, R. A. *Tetrahedron Lett.* **1963,** *4,* 1155–1160. doi:10.1016/s0040-4039(01)90794-4
27. Jin, L.; Amaya-Mazo, X.; Apel, M. E.; Sankisa, S. S.; Johnson, E.; Zbyszynska, M. A.; Han, A. *Biophys. Chem.* **2007,** *128,* 185–196. doi:10.1016/j.bpc.2007.04.005
28. Duarte, H. A.; Carvalho, S.; Paniago, E. B.; Simas, A. M. *J. Pharm. Sci.* **1999,** *88,* 111–120. doi:10.1021/js980181r
29. Lertvorachon, J.; Kim, J.-P.; Soldatov, D. V.; Boyd, J.; Roman, G.; Cho, S. J.; Popek, T.; Jung, Y.-S.; Lau, P. C. K.; Konishi, Y. *Bioorg. Med. Chem.* **2005,** *13,* 4627–4637. doi:10.1016/j.bmc.2005.04.032
30. Spiwok, V. *Molecules* **2017,** *22,* 1038. doi:10.3390/molecules22071038
31. Van Nguyen, T. T.; Yang, G. X.; Phan, A. N.; Nguyen, T.; Ho, T. G.-T.; Nguyen, S. T.; Ky Phuong, H. H. *RSC Adv.* **2022,** *12,* 19225–19231. doi:10.1039/d2ra02944h
32. Hou, T.; Guo, K.; Wang, Z.; Zhang, X.-F.; Feng, Y.; He, M.; Yao, J. *Cellulose* **2019,** *26,* 5065–5074. doi:10.1007/s10570-019-02433-w
33. Zhang, H.; Jiang, D.; Zhang, B.; Hong, J. G.; Chen, Y. *Electrochim. Acta* **2017,** *239,* 65–73. doi:10.1016/j.electacta.2017.04.008
34. Kumar, M.; Singh, S.; Shahi, V. K. *J. Phys. Chem. B* **2010,** *114,* 198–206. doi:10.1021/jp9082079
35. Sonker, A. K.; Rathore, K.; Nagarale, R. K.; Verma, V. *J. Polym. Environ.* **2018,** *26,* 1782–1794. doi:10.1007/s10924-017-1077-3
36. González-Guisasola, C.; Ribes-Greus, A. *Polym. Test.* **2018,** *67,* 55–67. doi:10.1016/j.polymertesting.2018.01.024
37. Bowes, J. H.; Cater, C. W. *Biochim. Biophys. Acta, Protein Struct.* **1968,** *168,* 341–352. doi:10.1016/0005-2795(68)90156-6
38. Gao, M.; Xie, X.; Huang, T.; Zhang, N.; Wang, Y. *Res. Square* **2022**. doi:10.21203/rs.3.rs-1329529/v1
39. Xu, Q.; Chen, C.; Rosswurm, K.; Yao, T.; Janaswamy, S. *Carbohydr. Polym.* **2016,** *149,* 274–281. doi:10.1016/j.carbpol.2016.04.114
40. Sen, S.; Losey, B. P.; Gordon, E. E.; Argyropoulos, D. S.; Martin, J. D. *J. Phys. Chem. B* **2016,** *120,* 1134–1141. doi:10.1021/acs.jpcb.5b11400

License and Terms

BEILSTEIN JOURNAL OF NANOTECHNOLOGY

Supramolecular hydration structure of graphene-based hydrogels: density functional theory, green chemistry and interface application

Hon Nhien Le*[1,2], Duy Khanh Nguyen[3,4], Minh Triet Dang[5], Huyen Trinh Nguyen[2,6],
Thi Bang Tam Dao[1,2], Trung Do Nguyen[1,2], Chi Nhan Ha Thuc*[1,2] and Van Hieu Le*[1,2,7]

Full Research Paper

Open Access

Address:
[1]Faculty of Materials Science and Technology, University of Science, Ho Chi Minh City, 700000, Vietnam, [2]Vietnam National University, Ho Chi Minh City, 700000, Vietnam, [3]Laboratory for Computational Physics, Institute for Computational Science and Artificial Intelligence, Van Lang University, Ho Chi Minh City, 700000, Vietnam, [4]Faculty of Mechanical – Electrical and Computer Engineering, School of Technology, Van Lang University, Ho Chi Minh City, 700000, Vietnam, [5]School of Education, Can Tho University, Can Tho City, 90000, Vietnam, [6]Faculty of Chemistry, University of Science, Ho Chi Minh City, 700000, Vietnam and [7]Multifunctional Materials Laboratory, University of Science, Ho Chi Minh City, 700000, Vietnam

Email:
Hon Nhien Le* - lhnhien@hcmus.edu.vn; Chi Nhan Ha Thuc* - htcnhan@hcmus.edu.vn; Van Hieu Le* - lvhieu@hcmus.edu.vn

* Corresponding author

Keywords:
antibacterial coating; bioinspired hydration; density functional theory; graphene-based hydrogel; supramolecular structure

Beilstein J. Nanotechnol. **2025,** *16,* 806–822.
https://doi.org/10.3762/bjnano.16.61

Received: 21 January 2025
Accepted: 08 May 2025
Published: 04 June 2025

This article is part of the thematic issue "Emerging technologies and nanomaterials for sustainability".

Guest Editor: V. V. Pham

Abstract

Natural hydration shells are discovered to play an essential role in the structure and function of biomolecules (deoxyribonucleic acid, protein, and phospholipid membrane). Hydration layers are also important to the structure and property of artificial graphene-based materials. Our recent works prove that graphene-based hydrogels are supramolecular hydration structures that preserve graphene nanosheets from the restacking through hydrophobic force, van der Waals force, and π–π interaction. In this manuscript, density functional theory and high-performance computing (HPC) are used for modeling and calculating van der Waals force between graphene nanosheets in water-intercalated AB bilayer graphene structures. A layer of water molecules significantly decreases the intersheet van der Waals force. A novel hydrogel of graphene oxide–silica gel–zinc hydroxide (GO-SG-ZH) is experimentally synthesized to demonstrate the advantages of hydrated hydrogel structure in comparison with dry powder structure. The synthesis of graphene-based hydrogels is a green chemistry approach to attain extraordinary properties of graphene-based nanostructures. Analytical characterizations exhibited moisture contents, water evaporation rates, three-dimensional structures, elemental compositions, aqueous dispersibility, and antibacterial activities. Hydration shells on graphene-based nanosheets in the hydrogel increase intersheet distances to prevent the stacking of the nanostructures. Hydration layers in the GO-SG-ZH hydrogel was also lubricative for direct brush coating on polymer substrates, typically polylactide films. Interfacial adhesion of graphene-based nanosheets on polylactide substrates made the antibacterial coating stable for several application purposes. In general, supramolecular graphene-based hydrogels are bioinspired hydration structures to advance nanoscale properties and nanotechnology applications.

Introduction

Biological cells are assemblies of biomolecules that are hydrated with water molecules. The cell content includes about 70–95% water that creates an aqueous environment for biological processes. Water molecules are bound to biomolecular surfaces and participate in the structuring and functioning of biomolecules, typically the folding of protein and the twisting of the double helix of deoxyribonucleic acid (DNA) [1]. Water molecules and their hydrogen bonding network function as lubricants for biomolecular dynamics. Recent scientific works have analyzed the important role of hydration shells on DNA, proteins, and phospholipid membranes [2-4]. The first hydration shell (about 3.5 Å) at the interface of biomolecules has considerably slower dynamics than water molecules in the bulk. Besides, the first water layer on the interface is responsible for hydration forces between biomolecular structures [5]. The rearrangement of water molecules through hydrogen bonding on hydrated surfaces generates repulsive hydration forces when another surface perturbs the hydration layers [6-8]. Hydration shells and hydration forces keep the hydrated structures stable and functional in the natural concert of biological processes.

In the aspect of artificial nanomaterials, it is proposed that hydration also plays an important role in the stability and functionality of nanoscale structures. Van der Waals forces are supramolecular intermolecular interactions that govern the agglomeration of nanomaterials. Carbon nanostructures with π-conjugated systems (fullerene, carbon nanotube, and graphene) have π–π interactions, a type of van der Waals force, for supramolecular attraction [9]. Particularly, graphene sheets with a large surface area and π-conjugated network are likely to stack together through hydrophobic agglomeration and π–π interaction. Although π–π interactions are generally weaker than hydrogen bonding, two graphene sheets in face-to-face geometry have a large interaction surface area to multiply the van der Waals force per unit area, resulting in strong binding energy of total attraction forces. The restacking of graphene-based nanosheets, including pristine graphene, graphene oxide (GO), and reduced graphene oxide (RGO), causes the drawbacks of small effective surface area and low dispersibility in media [10]. Several approaches have been reported to prevent the irreversible stacking of graphene-based nanosheets, including electrostatic repulsion, nanoparticle intercalation, three-dimensional assembly, and surface hydration [10-12]. In our previous works, a number of graphene-based hydrogels (RGO-SnO_2, RGO-ZnO, and RGO) were synthesized to evidence the reversible self-assembly of graphene-based nanosheets thanks to water intercalation in the hydrated ensembles [13-17]. Therefore, supramolecular graphene-based hydrogels with hydration intercalation and hydration force are quite useful for preserving and generating graphene-based nanosheets for many applications.

In this manuscript, we calculated van der Waals forces in bilayer graphene structures using density functional theory modeling (DFT) and dispersion energy correction functional (DFT-D3). The theoretical work aimed to elucidate the relationship between water intercalation and intersheet binding energy in quantum mechanical level. The computational calculations quantified intersheet distance, van der Waals force, bandgap energy, and formation energy of the molecular system of bilayer graphene intercalated with a water layer. In the experimental aspect, green chemistry methods were applied for synthesizing GO nanosheets, rice-husk-derived silica gel (SG), nano-silica–zinc hydroxide nanoparticles (SG-ZH), and graphene oxide–nanosilica–zinc hydroxide nanocomposites (GO-SG-ZH). Graphite oxidation reaction in a cascade design gives good efficiency values of energy, chemical reaction, and reaction time [14,15]. The recycling of rice husk ash waste into nanosilica products is eco-friendly and sustainable for circular economy [18-21]. Especially, GO nanosheets decorated with SG-ZH nanoparticles have hydrophilic surfaces to retain hydration layers in the hydrogel structure of the GO-SG-ZH nanocomposite. Hydration layers in the GO-SG-ZH hydrogel also function as lubricants at the nanomaterials interfaces, leading to facile brush coating on plastic films of polylactide (PLA). Dehydrated GO-SG-ZH coating is adhered to the PLA substrate through interfacial interactions. Furthermore, antibacterial activities, coating stability, and mechanical properties of the nanocomposite materials were investigated and described in the results and discussion.

Methods

Computation method of density functional theory

First-principles calculations based on DFT were conducted using the Vienna ab initio simulation software (VASP) and a high-performance computing system (HPC). The projector-augmented wave method (PAW) was implemented in electronic structure calculations. Generalized gradient approximation of Perdew–Burke–Ernzerhof (GGA-PBE) was used for describing exchange-correlation energy of electron–electron interactions. The correction of van der Waals dispersion energy was applied using the DFT-D3 method proposed by Grimme [22-24]. The modeling of infinite graphene sheets was extrapolated from periodic supercells. The supercell of bilayer graphene structure includes 16 carbon atoms (two graphene sheets with eight carbon atoms per sheet). The modeling of water-intercalated bilayer graphene structure used the supercell of 16 carbon atoms, one oxygen atom, and two hydrogen atoms (two graphene sheets and one water molecule).

Preparation of graphene oxide from natural graphite

The improved cascade-design synthesis of graphite oxide (GrO) was reported in our previous papers [15,16]. Briefly, 5 g of raw material of natural graphite (Shanghai Zhanyun Chemical) was soaked and agitated in 50 mL of 98% sulfuric acid. The solution of Mn(VII) compound was prepared by dissolving 10 g of potassium permanganate in 100 mL of 98% sulfuric acid. The graphite/H_2SO_4 suspension was slowly poured into the Mn(VII) solution. A cooling water bath and an infrared thermometer were used for controlling the reactor temperature below 55 °C (the peak of the reactor temperature is about 50 °C). After agitation in room-temperature conditions for 4 h, the graphite/Mn(VII)/H_2SO_4 suspension was slowly poured into 360 mL of water (the exothermic heat increased the reactor temperature to above 90 °C). After 2 h of agitation, the reaction was mixed with 150 mL of a 5% H_2O_2 solution and kept stirring for one day. After washing to neutral pH, the material was dried and ground to produce a GrO powder (moisture ≈20%). Next, the GrO powder was dispersed in water and sonicated for 1 h. After natural sedimentation overnight, the suspension was decanted to collect the supernatant dispersion of GO nanosheets.

Preparation of nanosilica from rice husk ash waste

Rice husk ash that was discarded from industrial boilers was collected for recycling experiments. Our method of nanosilica synthesis using potassium hydroxide and acetic acid was mentioned in a recent paper [21]. Raw material from rice husk ash waste was dispersed in a 7% potassium hydroxide solution. The suspension was agitated for 1 h at a temperature range of 80–90 °C. After careful filtration, a clear yellow solution of potassium silicate was obtained and neutralized with a 15% acetic acid solution. After that, the suspension of precipitated nanosilica was incubated overnight and then thoroughly washed with water. The obtained product of silica gel (SG) was used for subsequent synthesis and brush coating experiments.

Synthesis of graphene oxide–nanosilica–zinc hydroxide hydrogel

The suspension of 0.625 g GrO and 250 mL of water was agitated and then sonicated for 1 h. The suspension was decanted to collect about 250 mL of GO dispersion. An amount of 4.4 g of $Zn(CH_3COO)_2{\cdot}2H_2O$ was dissolved in 250 mL of water to prepare a 250 mL Zn^{2+} solution. The Zn^{2+} solution was slowly dropped into the GO solution under stirring. The obtained GO/Zn^{2+} dispersion was sonicated for 30 min. Besides, 20 g of the SG material (moisture ≈95%) was mechanically dispersed in 480 mL of water for 15 min and then sonicated for 15 min. A volume of 500 mL of the as-prepared GO/Zn^{2+} dispersion was dropped into the 500 mL SG dispersion. The mixture was agitated for 15 min and sonicated for 15 min. Then, the reaction was adjusted to pH 10 using ammonia solution for $Zn(OH)_2$ precipitation and kept stirring for 1 h. After sedimentation, the material was filtered and thoroughly washed with water. A hydrogel of graphene oxide–nanosilica–zinc hydroxide (GO-SG-ZH hydrogel) was collected and analyzed.

To produce a GO-SG-ZH product in powder form, the GO-SG-ZH hydrogel was dried at 80 °C and ground to obtain the GO-SG-ZH powder. The graphene-based nanocomposites in hydrogel form and in powder form were comparatively characterized using moisture analysis, scanning electron microscopy (SEM), energy-dispersive X-ray spectroscopy (EDS), and aqueous dispersibility.

Brush coating of graphene oxide–nanosilica–zinc hydroxide hydrogel on polylactide film

At first, commercial polylactide granules (PLA Luminy LX175, TotalEnergies Corbion) was put in a steel mold for thermal compression at 190 °C to produce a PLA plate. A piece of the PLA plate was put in a thin plastic mold (polyethylene terephthalate) for thermal compression at 190 °C. As a result, thin and transparent PLA films were made with the average thickness of 0.2 mm.

In the next stage, the GO-SG-ZH nanocomposite in hydrogel form (≈95% water) was used as an aqueous paint for brush coating on PLA thin films. After brush coating, the coated films were left to air dry for 3 h and were mildly dried using a hair dryer. The obtained coated films were denoted as GO-SG-ZH/PLA. Besides, the as-synthesized SG hydrogel (≈95% water) was also suitable for direct brush coating on PLA films. A similar procedure of brush coating was applied to produce PLA thin films coated with nanosilica. The nanosilica-coated films were denoted as SG/PLA.

Materials characterization

Materials weight and moisture values were measured using a laboratory balance (Ohaus Pioneer, 220 g/0.0001 g) and a moisture analyzer (A&D Weighing MX-50, 51 g/0.001 g), respectively. Scanning electron microscopy and energy-dispersive X-ray spectroscopy were performed using a JSM-IT200 system (JEOL). Samples were coated with Pt before the SEM-EDS analysis. X-ray diffraction was performed on a D8 Advance instrument (Bruker). Fourier-transform infrared spectroscopy (FTIR) was characterized with a FT/IR-6600 instrument (Jasco). Ultraviolet–visible absorption spectroscopy (UV–vis) and light transmittance spectroscopy were recorded using a V-670 spectrophotometer (Jasco). Microscopic texture and imaging were observed by a stereo zoom microscope (Optika SZM). Agar diffusion assays were used for testing antibacterial activity against *E. coli* and *S. aureus* (the positive control was the antibiotic penicillin). Inhibition zone assays were used to evaluate antibiofilm properties of uncoated and coated plastic films [14,25]. Coating stability of plastic films in an environment simulating aqueous food was tested using the method reported in our previous paper [14,26]. Measurement of tensile properties was conducted using a universal tensile testing machine (Yang Yi Technology, 500-N load cell) and the ASTM D882-18 standard [14,27].

Results and Discussion

Density functional theory calculations of intersheet distances, van der Waals forces and bandgaps

The van der Waals force between two graphene nanosheets arises from the π–π interaction between π orbitals of carbon atoms in one graphene sheet and π orbitals of carbon atoms in the other graphene sheet. The van der Waals force is responsible for AB graphene stacking in natural multilayer graphite [28]. Production processes convert multilayer graphite into single-layer graphene sheets dispersed in solvent medium. However, after the drying process, solvation shells of graphene sheets are removed, resulting in smaller distances between graphene sheets and larger interaction surfaces. With a short intersheet distance and large interaction surface area, van der Waals forces between graphene sheets increase to a higher binding energy which accounts for the restacking of graphene sheets. The restacking of graphene materials at dry state is the main cause of lower aqueous dispersibility and reduced surface area of graphene-based materials in many applications, such as aqueous dispersions, polymer nanocomposites, and water-based paints. Our previous works demonstrated that in graphene-based hydrogel structures, the intercalation of water molecules between graphene-based sheets maintains large intersheet distances and low interaction surface area, which leads to reduced binding energy of van der Waals force [14,15]. The simple method of water intercalation in hydrogel structures is an effective bioinspired approach to prevent nanosheet stacking and preserve graphene-based nanostructures.

Herein, DFT calculations were performed to quantify the van der Waals dispersion interactions in pristine bilayer graphene and water-intercalated bilayer graphene structures. In natural multilayer graphite, graphene sheets stack together in an AB configuration. Figure 1a shows the modeling of a bilayer graphene structure that mimics the AB stacking in multilayer graphite. DFT optimization calculation presented that pristine bilayer graphene has the formation energy of −9.3778 eV/supercell, intersheet distance of 3.459 Å, and van der Waals binding energy of 0.064 eV/atom (Figure 1a and Table 1). The intersheet distance is comparable to the values reported in other papers [29-31]. The bilayer graphene structure has a small bandgap of 0.06 eV which is slightly open in comparison to the zero bandgap of a single-layer graphene sheet.

Besides, DFT modeling of the water-intercalated AB bilayer graphene structure was also calculated by HPC. The resulting formation energy is −10.6414 eV/supercell (Table 1). In the optimal structure (Figure 1c and 1d), hydrogen atoms of the water molecule are oriented toward graphene sheets due to the hydrogen–π interaction. It is noteworthy that the enlarged intersheet distance of 6.626 Å led to the intersheet binding energy of 0.04 eV/atom. A layer of water molecules in between two graphene sheets significantly declined the van der Waals force by 37.5% (from 0.064 to 0.040 eV). The bandgap of the water-intercalated bilayer graphene structure increased to 0.09 eV. Although the opening of the bandgap is still small, it is suggested that the bandgap of the AB bilayer graphene can be further opened by increasing molecular water layers in the intersheet spacing as well as the spacing distance. The approach of water intercalation in graphene-based structures is effective for lowering van der Waals force and opening the bandgap. Therefore, water-intercalated structures of graphene-based nanosheets should be experimentally synthesized to ameliorate the nanostructures and properties for various applications in science and industry.

Supramolecular hydration structure of graphene oxide–nanosilica–zinc hydroxide hydrogel

The computational DFT results confirm the importance of supramolecular interaction of water intercalation in graphene-

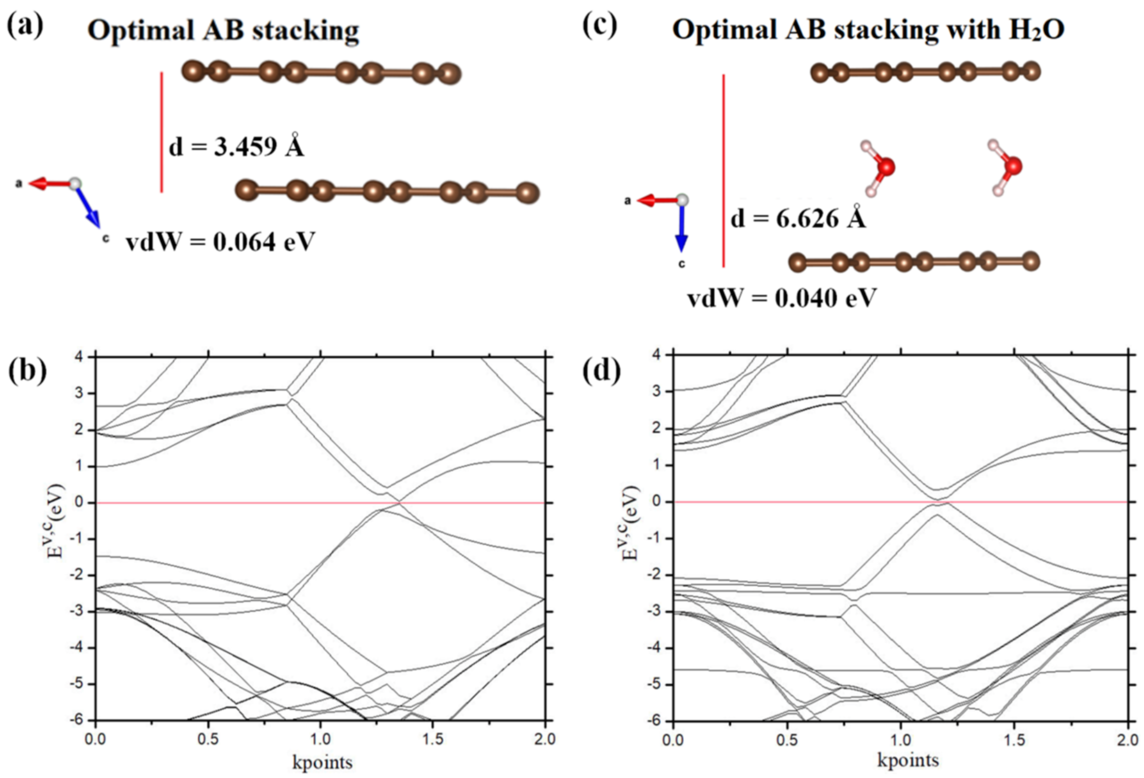

Figure 1: DFT modelling of AB bilayer graphene structures. The AB bilayer graphene with the intersheet distance of 3.459 Å (a), and its valence–conduction band structure in hexagonal Brillouin zone (b). The AB bilayer graphene structure intercalated with a layer of water molecules and the intersheet distance of 6.626 Å (c), and its electronic band structure in hexagonal Brillouin zone (d).

Table 1: Formation energies, intersheet distances, van der Waals forces, and band gaps of bilayer graphene structures.

Configuration	Formation energy (eV)	C–C bond length (Å)	Intersheet distance (Å)	van der Waals force (eV)	Bandgap (eV)
Pristine AB bilayer graphene	−9.3778	1.42	3.459	0.064	0.06
AB bilayer graphene intercalated with a water layer	−10.6414	1.42	6.626	0.040	0.09

based structures. In this research, we synthesized graphene-based hydrogels of graphene oxide–nanosilica–zinc hydroxide nanocomposite (GO-SG-ZH hydrogel) as a supramolecular hydration structure. Figure 2a describes the supramolecular hydration assembly of the GO-SG-ZH hydrogel. GO nanosheets have brown color, and the hydration shells of water molecules is highlighted with blue color. Hydrophilic functional groups on GO nanosheets, SG nanoparticles, and ZH nanostructures are attractive to water molecules to form hydration shells on the surfaces. In addition to hydration layers, the three-dimensional assembly of graphene-based nanosheets provides high porosity as water reservoirs which supply water to intersheet spacings. High water content and large spacing distance in the hydrogel structure are key factors that prevent van der Waals and π–π interactions between graphene-based sheets.

Figure 2b depicts the hydrated assembly of biological cells in nature. The natural hydrated structure includes intracellular water, cell wall water, and intercellular water [32]. Hydration shells on the cellular walls or biomembranes are important to maintain cellular shape. The first bound water molecules on the biomembranes is a biointerfacial water layer (≈2.6 Å) which is responsible for primary hydration force [33-37]. Hydration forces in the range of 4–5 water layers contribute with repulsive energy to the biological system. Supramolecular hydrogen bonding between biostructures and water molecules leads to

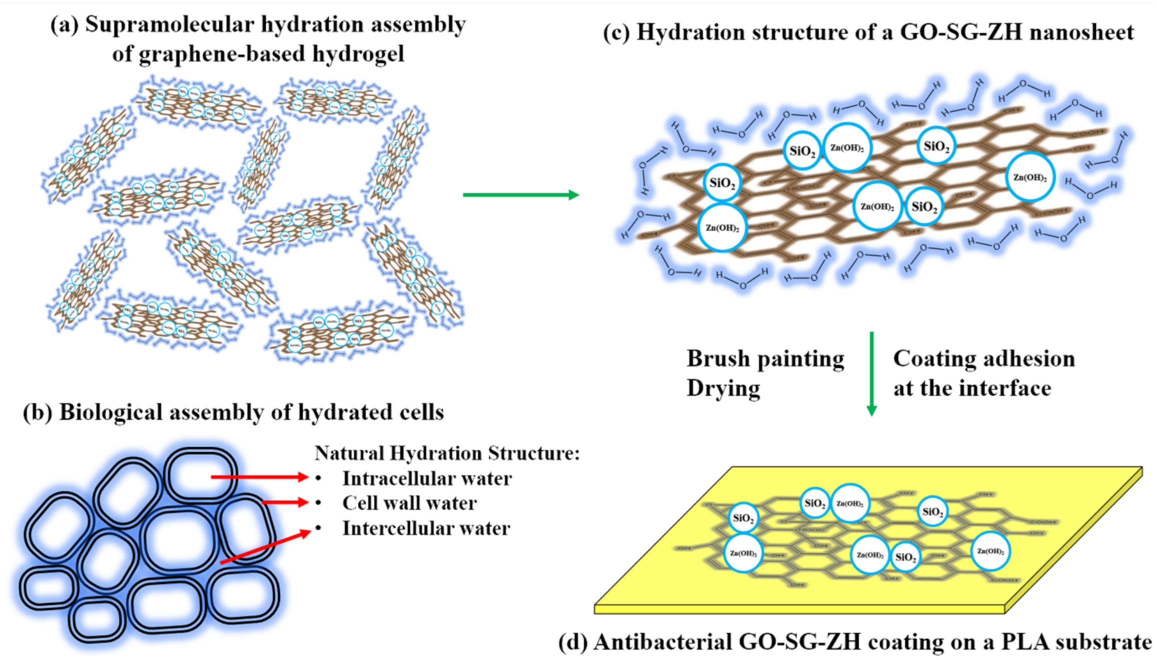

Figure 2: (a) Illustration of supramolecular self-assembly of a graphene-based hydrogel. (b) Depiction of a natural assembly of biological cells stabilized by hydration structures (water molecules on cell wall membranes are highlighted with blue color). (c) Drawing of a synthetic graphene-based nanosheet (GO-SG-ZH) covered by a hydration shell. (d) Presentation of a graphene-based coating (antibacterial GO-SG-ZH) that adheres to a substrate (PLA film).

repulsive hydration forces when the surfaces are closely approached. The artificial structure of graphene-based hydrogel in Figure 2a is biomimetic to the natural system of biological cells described in Figure 2b. Hydration shells on GO-SG-ZH nanosheets, particularly the first interfacial water layer, generate hydration forces to maintain intersheet distances and nanoscale structures in the artificial system. The drawing in Figure 2c is the presentation of a graphene-based nanosheet with a first bound water layer which is responsible for the primary hydration force. In the next stage, after brush coating of the GO-SG-ZH hydrogel on a polylactide film, hydration shells are evaporated in the drying process, and the graphene-based nanosheets adhere to the substrate through electrostatic interaction, hydrogen bonding, and van der Waals interaction (Figure 2d).

Experimentally, GO nanosheets, SG, nanoparticles, and SG-ZH nanoparticles were synthesized and separately characterized as exhibited in SEM images in Figure 3a–c. Particularly, artificial nanocomposites of GO-SG-ZH powder (Figure 3d–f) and GO-SG-ZH hydrogel (Figure 3g–i) were prepared for comparative analysis. While the GO-SG-ZH powder is a dry solid (moisture ≈10%), the GO-SG-ZH hydrogel has a moisture content of 95% and viscoelastic behavior. The hydrogel was elastic to resist the deformation under gravitational force and also viscous to slowly deform (see Supporting Information File 1, Figure S2). The moisture content of the GO-SG-ZH hydrogel is comparable with those of natural cellular systems (moisture content of apple tissues is about 90%) [32]. In Figure 3e and 3f, SEM images of GO-SG-ZH powder show a macroscopic particle and its microscopic structure. Since the material was dehydrated, graphene-based nanostructures could be covalently cross-linked through esterification reaction of carboxyl and hydroxyl groups on GO nanosheets [38]. The GO-SG-ZH nanosheets agglomerated and stacked together to form big particles (size of hundreds of micrometers, Figure 3e). The GO-SG-ZH particles had low porosity or small spacing between graphene-based nanosheets (Figure 3f). Besides, the GO-SG-ZH hydrogel was spread on a carbon tape and dehydrated for SEM imaging (Figure 3h and 3i). Although GO-SG-ZH nanosheets agglomerated into microstructures (Figure 3h), the self-assembly of graphene-based nanosheets was different from the stacked morphology of the GO-SG-ZH powder. At a higher magnification of 20,000×, SEM image in Figure 3i revealed the porous structure with large spacing between graphene-based nanosheets. As a result, the GO-SG-ZH hydrogel is a three-dimensional assembly of water-intercalated graphene-based nanosheets.

Results of EDS analysis in Table 2 disclose the elemental contents of the as-prepared GO-SG-ZH powder and hydrogel. Accordingly, atomic proportions of carbon, oxygen, silicon, and zinc elements in both nanocomposites are relatively similar.

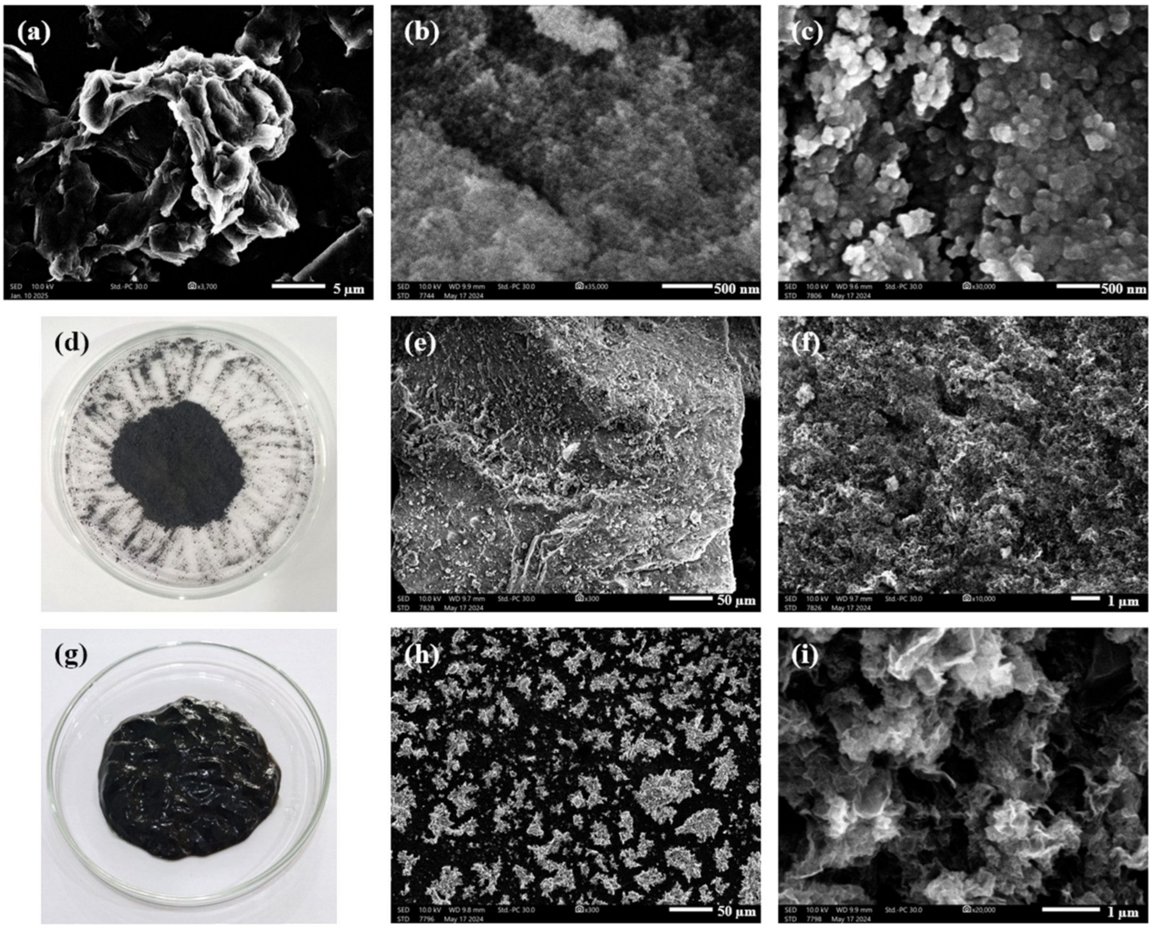

Figure 3: SEM images of GO nanosheets (a), SG nanoparticles (b), and SG-ZH nanoparticles (c). (d) Photograph of graphene oxide–nanosilica–zinc hydroxide powder. SEM images of particles and nanostructures in GO-SG-ZH powder with the scale bars of 50 µm (e) and 1 µm (f). (g) Photograph of hydrogel of graphene oxide–nanosilica–zinc hydroxide. SEM images of micro- and nanostructures in GO-SG-ZH hydrogel with the scale bars of 50 µm (h) and 1 µm (i).

Table 2: EDS analysis of elemental compositions of GO nanosheets, SG nanoparticles, SG-ZH nanoparticles, GO-SG-ZH powder, and GO-SG-ZH hydrogel.

Materials	C (atom %)	O (atom %)	Si (atom %)	Zn (atom %)
GO	66.36 ± 2.13	33.64 ± 2.85	–	–
SG	–	76.44 ± 2.79	23.56 ± 1.36	–
SG-ZH	–	61.51 ± 4.68	22.31 ± 2.57	16.18 ± 1.57
GO-SG-ZH powder	18.78 ± 1.22	57.53 ± 2.03	12.64 ± 0.84	11.04 ± 0.58
GO-SG-ZH hydrogel	23.66 ± 1.59	51.90 ± 2.30	11.63 ± 0.95	12.81 ± 0.73

Theoretical contents of SiO_2 and $Zn(OH)_2$ in the GO-SG-ZH nanocomposite powder are estimated to be 37.92% and 33.12%, respectively, so the remaining content of GO nanosheets is about 28.96%. Similarly, SiO_2, $Zn(OH)_2$, and GO contents derived from the GO-SG-ZH hydrogel are calculated to be 34.89%, 38.43%, and 26.68%, respectively. In Figure 4, the elemental mapping of the three-dimensional structure of the GO-SG-ZH hydrogel showed the presence and distribution of carbon, oxygen, silicon, and zinc atoms on the graphene-based surfaces. SG-ZH nanoparticles and oxygen-containing functional groups on GO nanosheets are hydrophilic nanostructures which retain hydration layers on the graphene-based nanosheets, leading to the supramolecular hydration structure of the GO-SG-ZH hydrogel.

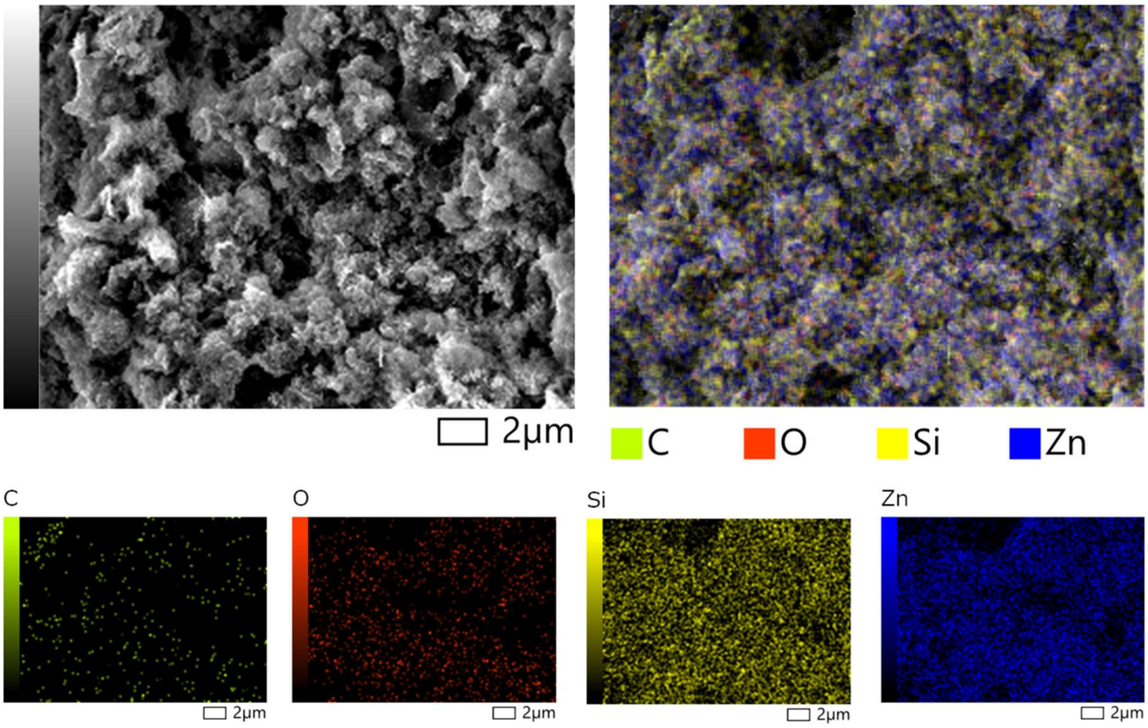

Figure 4: SEM-EDS elemental mapping of carbon atoms (green dots), oxygen atoms (red dots), silicon atoms (yellow dots), and zinc atoms (blue atoms) on the graphene-based nanostructure of GO-SG-ZH hydrogel after dehydration.

Water evaporation characteristics of the GO-SG-ZH hydrogel were recorded and analyzed during drying processes in the moisture analyzer (MX-50, resolution of 0.01%). Figure 5a describes the moisture curves during the drying process at 70, 85, and 100 °C, corresponding to the drying times of 170, 100, and 70 min, respectively. Although the corresponding drying times were different, the curves of cumulative evaporated water had a similar shape and amounted to 1.87 g (93.5% moisture, Figure 5b). The lower drying temperature of 70 °C was sufficient to evaporate the hydration layers in the hydrogel. A scientific report by Khan et al. demonstrated that the drying of apple tissues at 70 °C is critical to the rupturing of cell membranes, resulting in dehydration of the biological tissues [32]. In the drying process, water at the outer surface evaporated first, followed by the evaporation of intracellular water. Figure 5c and 5d exhibit the water evaporation rates as a function of drying time and water content in the GO-SG-ZH hydrogel. In the first period, the water evaporation rates increased to a plateau of constant drying rate, corresponding to the evaporation of free water molecules at the outer surface [39]. Then, the water evaporation curves entered into the decreasing rate period where there is deficiency of free water at the outer surface and water transport from the interior to the surface. The critical water content at which the first decreasing rate period began was identified to be about 40% (the left dashed line in Figure 5d). It is noticeable that at the water content of 20% (the middle dashed line in Figure 5d), the water evaporation rates at 70, 85, and 100 °C were approximately half the initial water evaporation rates at 5 min. There is a second decreasing rate period which occurred at the critical water content of 4% (the right dashed line in Figure 5d). Interestingly, in biological tissues, interfacial water integrated in cell walls is also about 2–5% [32]. It is explained that the significantly slower rates of water evaporation in the decreasing rate period are due to water movement from the interior to the surface and the hydrogen bonding of interfacial hydration layers on the hydrophilic nanostructures.

Crystallography, functional group, aqueous dispersibility and hydration lubrication

Dry powder of the GO-SG-ZH nanocomposite was analyzed using XRD and FTIR. In Figure 6a, the XRD pattern exhibited sharp characteristic peaks of the $Zn(OH)_2$ crystal at $2\theta = 20.2°$, 20.94°, 25.07°, 27.23°, 27.83°, and 32.97° [40-42]. Zinc hydroxide nanocrystals (ZH) were formed on the nanocomposite during the precipitation by alkaline ammonia in the synthesis process (see Methods section). The constituents of GO and SG nanomaterials had amorphous structures which did not give obvious peaks in the XRD pattern. Regarding the FTIR spectrum in Figure 6b, most of obvious peaks are attributed to func-

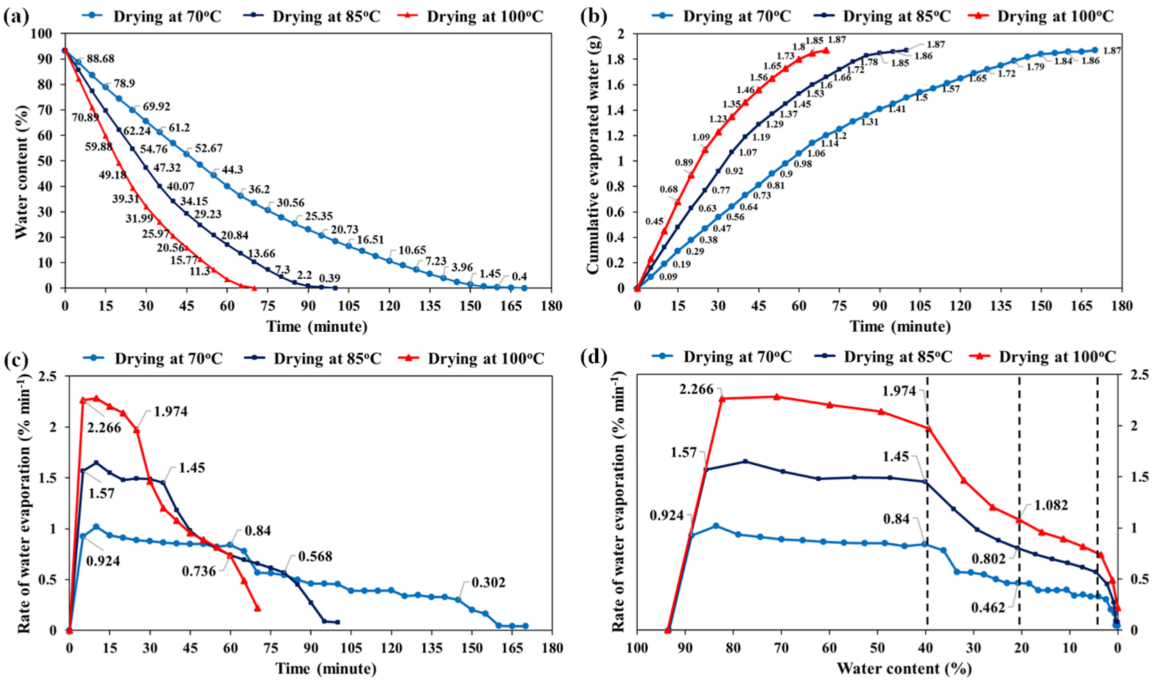

Figure 5: Analysis of moisture content and water evaporation of GO-SG-ZH hydrogel. (a) Curves of changing moistures of GO-SG-ZH hydrogel at different drying temperatures (70, 85, and 100 °C). (b) Curves of cumulative amount of evaporated water during drying at 70, 85, and 100 °C. (c) Plot of water evaporation rates with respect to drying time. (d) Plot of water evaporation rates with respect to water content in GO-SG-ZH hydrogel.

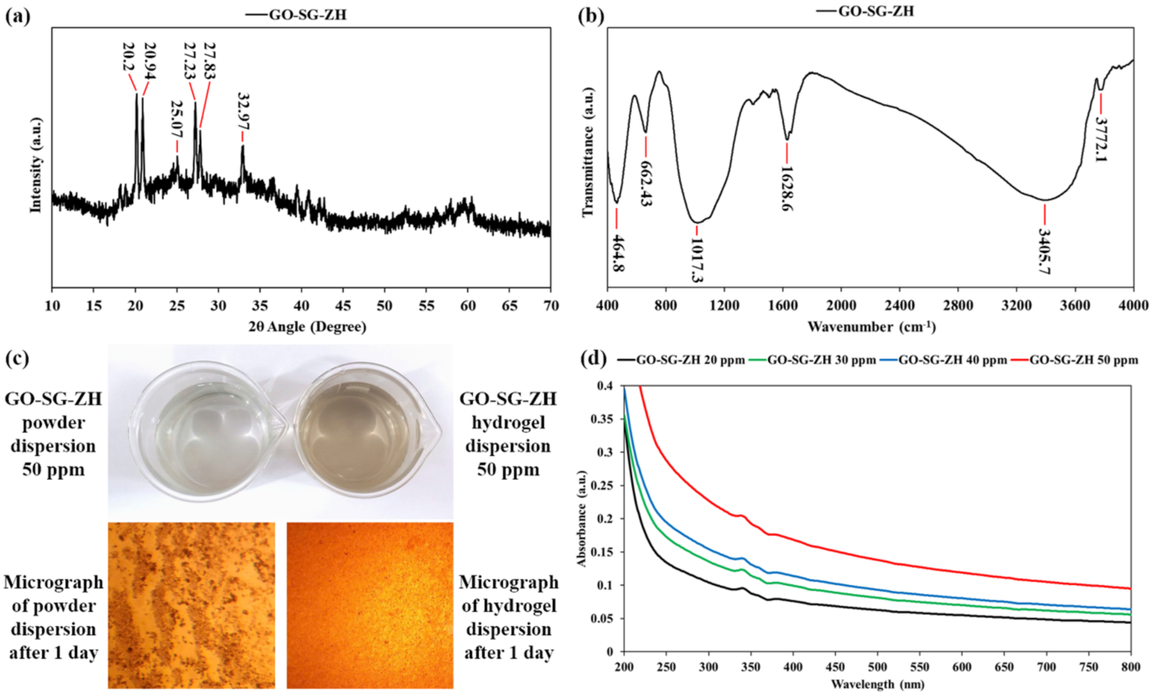

Figure 6: (a) XRD pattern of GO-SG-ZH powder. (b) FTIR spectrum of GO-SG-ZH powder. (c) Aqueous dispersions of GO-SG-ZH powder and hydrogel (concentrations of 50 ppm) and their sedimented particles after 1 day (visualized by the optical microscope). (d) UV–vis spectra of aqueous dispersions of GO-SG-ZH hydrogel.

tional groups of nanosilica. The vibration band at 3772.1 cm^{-1} is assigned to silanol groups on the nanosilica surface (Si–OH). The bands at 3405.7 and 1628.6 cm^{-1} are characteristic of stretching and bending modes, respectively, of water molecules adsorbed on the surface [43]. The bands at 1017.3 and 464.8 cm^{-1} represent the stretching vibrations of siloxane groups (Si–O–Si). Particularly, the FTIR band at 662.43 cm^{-1} is attributed to the bending vibration of Zn-O-Si bonds in the GO-SG-ZH nanocomposite [44].

Supramolecular systems with non-covalent interactions and reversible cross-links are recognized to provide extraordinary properties and applications [45-47]. Reversible self-assembly is an advantage of supramolecular graphene-based hydrogels in comparison with the powder form [13-16]. Hydration layers in between graphene-based sheets not only reduce intersheet binding energy (van der Waals force) but also generate repulsive forces for exfoliating the macroscopic assembly into nanoscale structures especially under external sonication and mechanical stimuli. Reversible self-assembly of graphene-based nanosheets in water is essential to many applications, such as adsorption, photocatalysis, biosensing, drug delivery, aqueous paints, and multifunctional coatings [48-50]. Figure 6c exhibits the aqueous dispersions derived from the sonication of GO-SG-ZH hydrogel and powder in water (see Supporting Information File 1, Figure S3). Ultrasound waves vibrated water molecules and created cavitation in the hydrogel structure, leading to the exfoliation of graphene-based nanosheets in water. It is notable that low concentrations (≤50 ppm) are necessary to obtain homogenous dispersions. The ultrasonic dispersion of GO-SG-ZH hydrogels was faster and clearer due to the high content of water intercalation. The GO-SG-ZH powder contained about 10% of water and approximate 60% of nanosilica and zinc hydroxide nanoparticles, which functioned as spacing layers between graphene-based nanosheets. Therefore, the ultrasonic treatment of GO-SG-ZH powder in water also yielded a homogeneous dispersion. However, the aqueous dispersion of GO-SG-ZH powder was not completely exfoliated in the aqueous environment and quickly settled down. Stacked agglomerates of GO-SG-ZH powder at the bottom of the dispersion were observed in the micrograph of Figure 6c, while the micrograph of the dispersion of GO-SG-ZH hydrogel showed the absence of stacked structures. In Figure 6d, UV–vis spectra of aqueous dispersions of GO-SG-ZH hydrogel present light absorption in the ultraviolet range (200–400 nm) that was proportional to the colloidal concentrations (50, 40, 30, and 20 ppm). Small absorption peaks at 340 and 360 nm correspond to nanosilica and zinc hydroxide nanoparticles, respectively [21,43]. In addition, hydration lubrication in supramolecular graphene-based hydrogels is important to applications in paints and coatings [51,52]. While the GO-SG-ZH powder could not be directly used for brush painting, the GO-SG-ZH hydrogel can be easily coated on various substrates using a simple brush. In the scientific literature, it is elucidated that water layers between graphene-based nanosheets significantly lower the interfacial frictions of the nanomaterials [53-55]. In this study, hydration lubrication makes supramolecular graphene-based hydrogels suitable for direct brush coating on PLA films.

Light transmittance spectroscopy, microscopic structure and elemental composition of graphene oxide–nanosilica–zinc hydroxide coating on polylactide films

Nanosilica hydrogels and graphene oxide–nanosilica–zinc hydroxide hydrogels were utilized as aqueous paints for brush coating on PLA films. After drying, thin coatings of SG and GO-SG-PLA were formed on the plastic substrates. Regarding appearance, while the blank PLA film was clearly transparent (Figure 7a), the SG/PLA film was slightly opaque (Figure 7b), and the GO-SG-ZH/PLA film was stripy with black lines of GO color (Figure 7c). Light transmittance spectra in Figure 7d show the transparency levels of the plastic films. In the visible light range of 400–700 nm, the average light transmittance values of blank PLA, SG/PLA, and GO-SG-ZH/PLA films are 94%, 90%, and 75% respectively. The SG coating made the transparency decrease 4%, and the GO-SG-ZH coating resulted in the transparency decline of 19% due to the white color of ZH nanoparticles and black color of GO nanosheets.

Microscopic structures of the GO-SG-ZH coating on a PLA film were observed and imaged using the optical stereo microscope. Since the PLA substrate was almost transparent, pictures in Figure 8a–c showed GO nanosheets, SG nanoparticles, and ZH nanostructures of the GO-SG-ZH coating. Reflected light from the GO-SG-ZH coating gave a three-dimensional vision of the coating texture. The nanostructures in the coating morphology are well-distributed. In Figure 8c, two-dimensional shapes of GO nanosheets are visualized. In Figure 8d–f, SEM provided high-resolution images of the GO-SG-ZH/PLA film. The brush-coated layer of the GO-SG-ZH nanocomposite was not completely uniform since rough coating morphology was observed on the substrate surface. Two-dimensional graphene-based sheets appeared in Figure 8e, and nanoparticles of SG and ZH were shown in Figure 8f. Integrated EDS analysis presented the elemental composition on the surface of the GO-SG-ZH/PLA film (Table 3). With the atomic contents of 8.13% of silicon and 6.36% of zinc, the atomic proportions of SiO_2 and $Zn(OH)_2$ in the nanocomposite were estimated to be 24.39% and 19.08%, respectively.

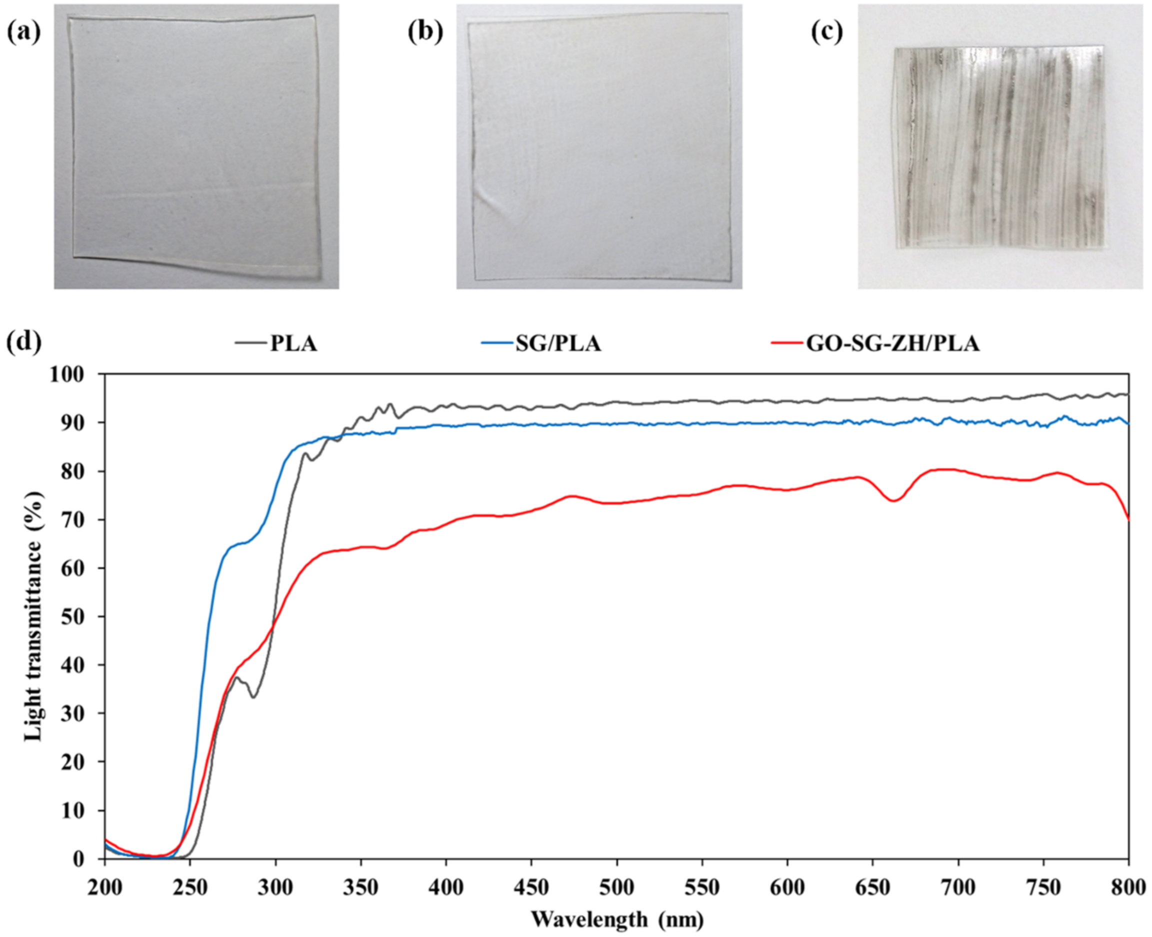

Figure 7: (a) A blank polylactide film (PLA). (b) A polylactide film coated with nanosilica (SG/PLA). (c) A polylactide film coated with graphene oxide–nanosilica–zinc hydroxide (GO-SG-ZH/PLA). (d) Light transmittance spectroscopy of thin films of PLA, SG/PLA, and GO-SG-ZH/PLA.

Antibacterial properties of graphene oxide–nanosilica–zinc hydroxide in hydrogel and in coating structures

The EDS analysis in Table 2 showed that the solid nanocomposite of GO-SG-ZH hydrogel was composed of 12.81% zinc atoms (derived from the $Zn(OH)_2$ constituent). ZH nanoparticles and GO nanosheets in the GO-SG-ZH hydrogel are antibacterial and antibiofilm agents with low toxicity for food packaging and biomedical applications [56,57]. The main antibacterial mechanism of GO nanosheets is cell membrane damage caused by direct contact of GO sharp edges with bacterial membranes [57,58]. The crucial antibacterial activity of ZH nanostructures is the delivery of Zn^{2+} ions to disrupt bacterial membranes and intracellular processes [59,60]. Antibacterial activity of the GO-SG-ZH hydrogel was tested in agar well diffusion assays (Figure 9). The photographic results showed inhibition zones against *E. coli* (Figure 9a) and *S. aureus* (Figure 9b). The inhibition zones resulted from the diffusion of ZH nanoparticles and Zn^{2+} cations from the hydrogel to the surrounding agar. As the GO-SG-ZH hydrogel is antibacterial, the brush coating of the GO-SG-ZH hydrogel on PLA films produced an antibacterial coating on the substrate.

Antibacterial tests of uncoated and coated PLA films are described in Figure 10, where the interfaces between PLA films and agar/*E. coli* plates are displayed. Before the incubation process, *E. coli* bacteria did not grow to biofilms (Figure 10a–c). After incubation at 37 °C for 24 h, stripy biofilms of *E. coli* bacteria were formed on the agar plates (Figure 10d–f). While stripy patterns were observed in the areas of blank PLA film (Figure 10d) and SG/PLA film (Figure 10e), the GO-SG-ZH/PLA film presented an inhibition zone at the vicinity of its boundary (Figure 10f). PLA and SG/PLA were not antibacterial materials, and the GO-SG-ZH coating was effective against the growth of *E. coli* biofilm on the coating surface. The antibiofilm result is attributed to the antibacterial activities of GO nanosheets and ZH nanoparticles. Regarding the antibacterial mechanism of the nanocomposite coating, direct contact of bacterial cells with sharp nanostructures of the coating is the cause of membrane damage and cell inactivation.

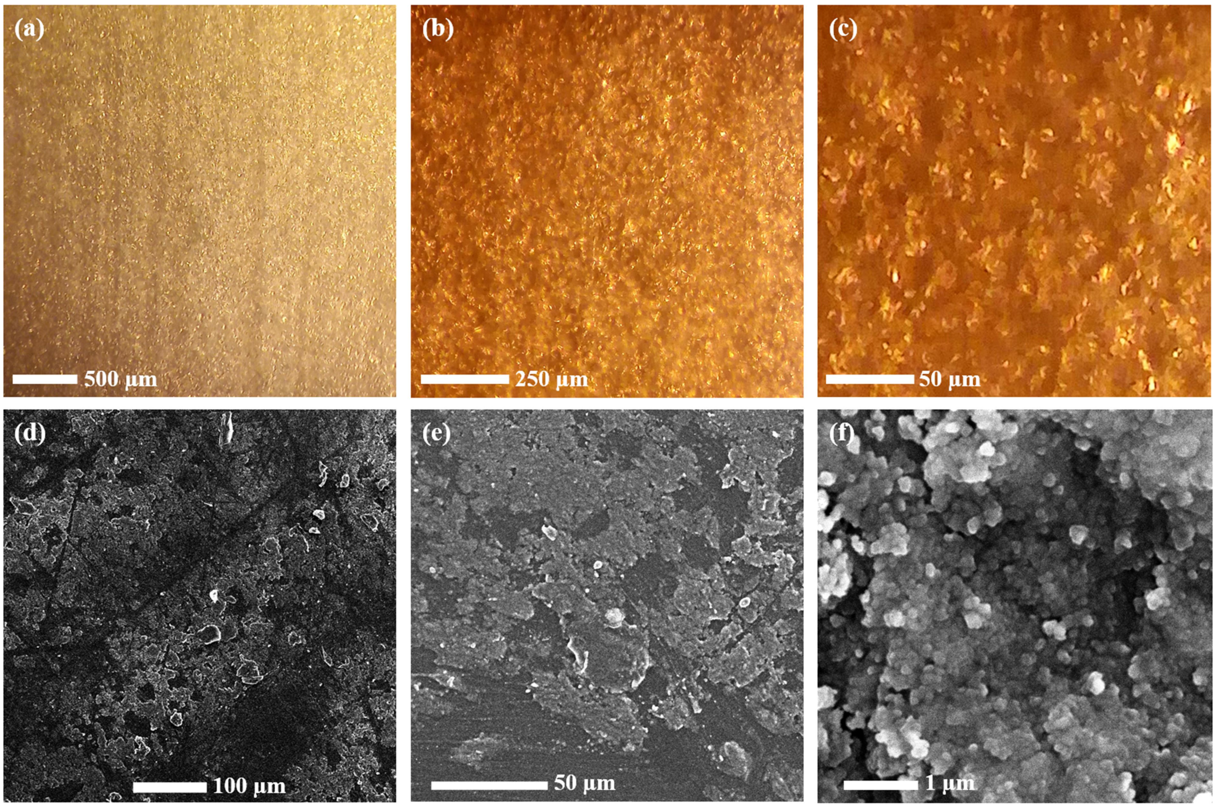

Figure 8: (a, b, c) Micrographs of morphology and structure of GO-SG-ZH coating on a PLA film. (d, e, f) SEM images of GO-SG-ZH coating on a PLA film.

Table 3: EDS elemental composition of the GO-SG-ZH coating on the PLA substrate.

Materials	C (atom %)	O (atom %)	Si (atom %)	Zn (atom %)
SG-GO-ZH/PLA film	45.86 ± 1.84	39.64 ± 1.98	8.13 ± 0.70	6.36 ± 0.47

Zn^{2+} cations released from ZH nanoparticles and reactive oxygen species generated by ZH nanoparticles and GO nanosheets are effective bactericidal agents that disrupt bacterial cells [56-60]. The antibacterial actions and results are meaningful for preventions of biofilm formation and surface-mediated infections [14,25,61]. GO-SG-ZH/PLA is a good material for packaging and biomedical applications thanks to its antibiofilm, safety, and biodegradability properties.

Stability of graphene oxide–nanosilica–zinc hydroxide coatings on polylactide films in aqueous environments

SG/PLA and GO-SG-ZH/PLA films were immersed in an environment simulating aqueous food for one month. The stability of the coatings in aqueous environments was measured by calculating the loss of coating weight. These experimental tests are useful for studying packaging materials and chemical releases over a time period in environments simulating food [14,27]. Line charts in Figure 11 report the weight losses of SG (Figure 10a) and GO-SG-ZH/PLA (Figure 10b) coatings after 1, 3, 5, 7, 10 and 30 days in aqueous solutions containing water, 3% acetic acid, 10% ethanol, and 50% ethanol. Both coatings were quite stable in pure water as the weight losses were insignificant even after 30 days. However, acidic and alcoholic solutions gave more notable effects on coating stability. Especially, the weight losses of SG coating in 50% ethanol were 0.32 mg/cm^2 after 3 days and 1.48 mg/cm^2 after 30 days. The high coating weight loss indicated that the coating of silica nanoparticles was not stable in 50% ethanol solution (equivalent to a fatty food environment). Besides, the coating of GO-SG-ZH nanocomposite showed weight losses of 0.3 mg/cm^2 after 3 days and 0.62 mg/cm^2 after 30 days in 50% ethanol. Although the coating weight losses were considerable in the first 3 days, the trend curve became steady in the period from 3 to 30 days. The GO-SG-ZH coating was more stable than the SG coating on PLA films. As demonstrated in our previous

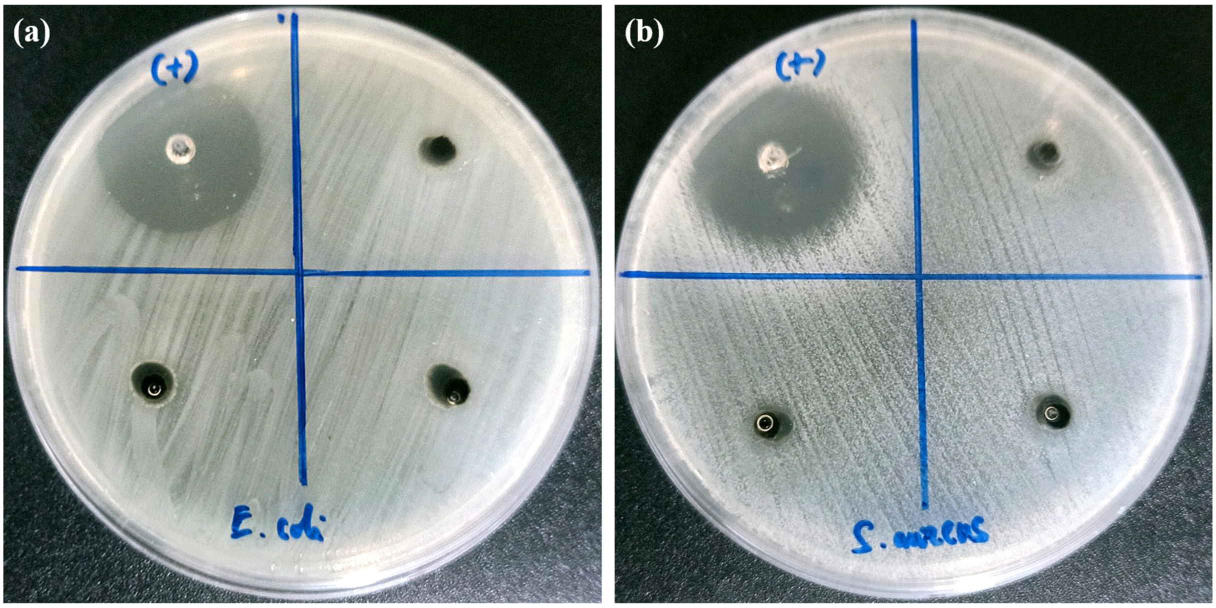

Figure 9: Agar well diffusion assay of the GO-SG-ZH hydrogel presents antibacterial activities of the GO-SG-ZH hydrogel against *E. coli* (a) and *S. aureus* (b).

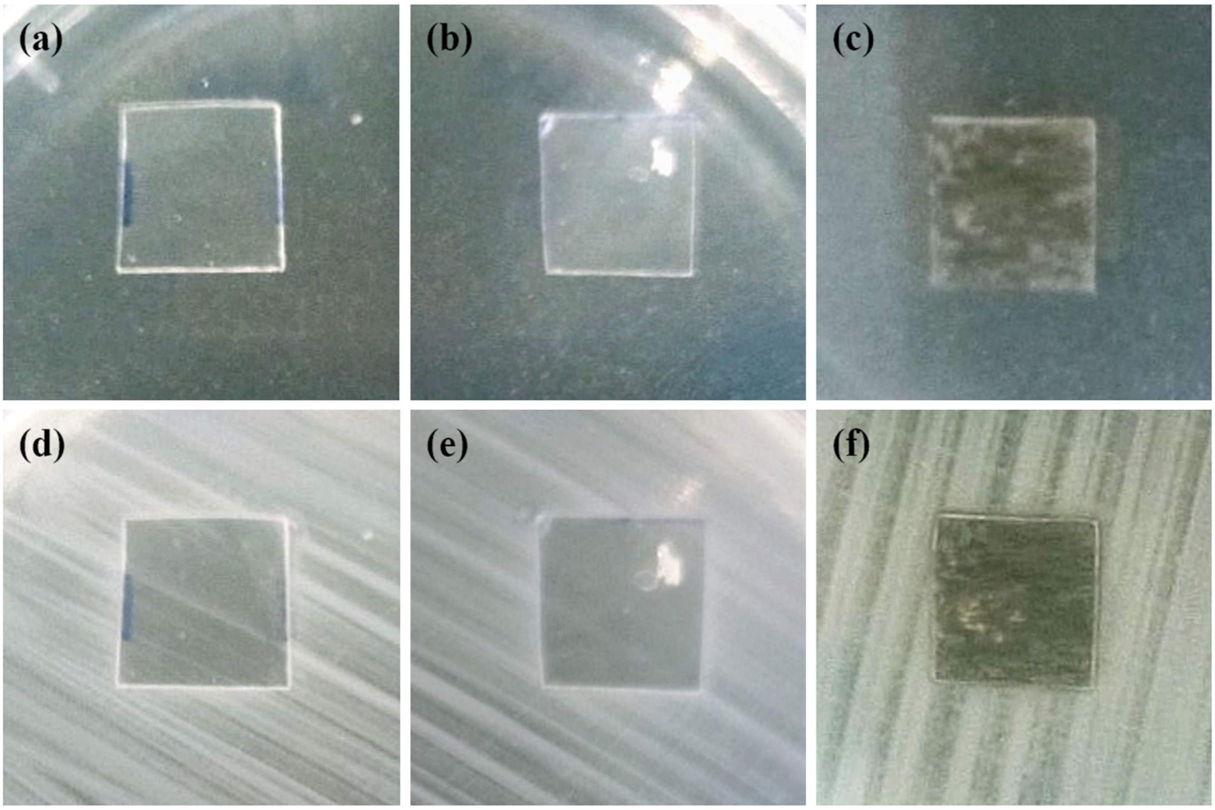

Figure 10: Antibacterial test of uncoated and coated PLA films against the growth of *E. coli* biofilm. (a, b, c) Pictures of a PLA film (a), an SG/PLA film (b), and a GO-SG-ZH/PLA film (c) on agar plates inoculated with *E. coli* bacteria (before incubation). (d, e, f) Pictures of the PLA film (d), SG/PLA film (e), and GO-SG-ZH/PLA film (f) on the agar/biofilm plates after incubation at 37 °C for 24 h.

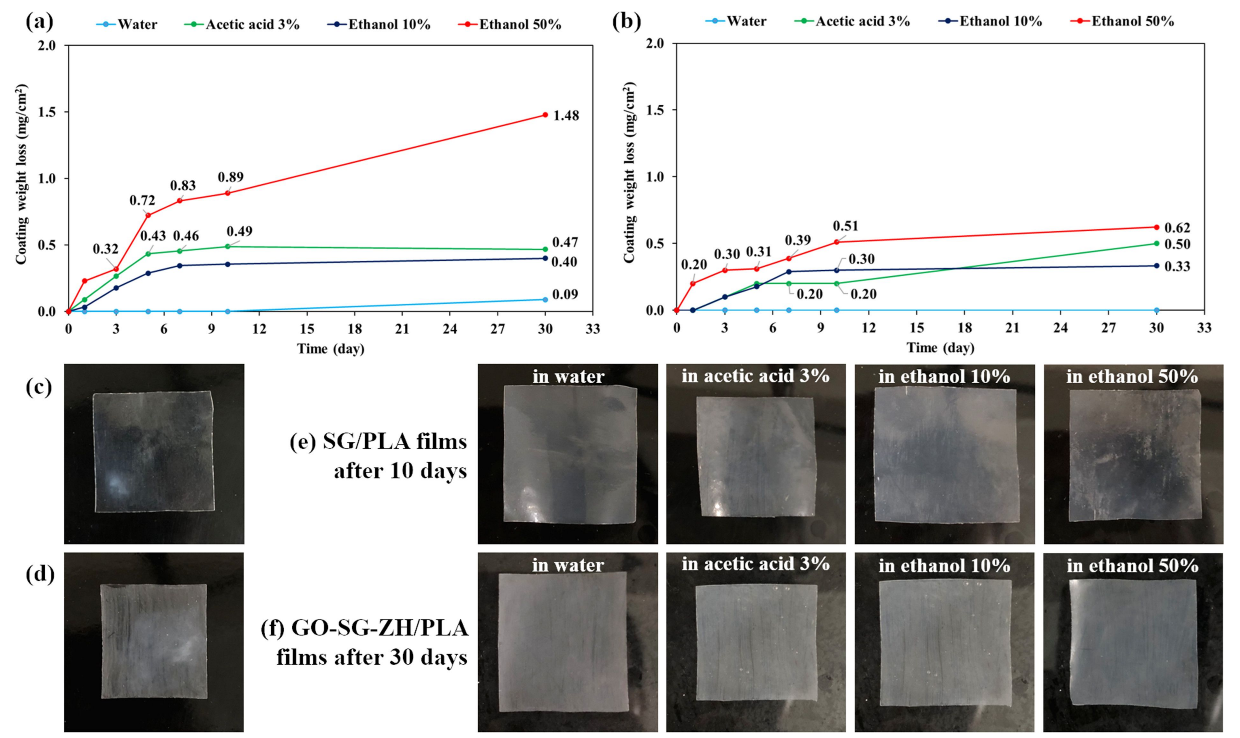

Figure 11: Stability testing of SG/PLA and GO-SG-ZH/PLA films in an environment simulating aqueous food (water, 3% acetic acid, 10% ethanol, and 50% ethanol). (a, b) Graphs of weight losses of SG coating (a) and GO-SG-ZH coating (b) in the period of 30 days in aqueous solutions. (c, d) Initial SG/PLA film (c) and GO-SG-ZH/PLA film (d). (e, f) Pictures of SG/PLA films after 10 days (e) and GO-SG-ZH/PLA films after 30 days (f) in aqueous environments.

paper, the coating of zinc hydroxide nanoparticles was not stable in aqueous solutions [14]. In this study, the stability of GO-SG-ZH coating is attributed to the role of graphene-based nanosheets. Large GO nanosheets are important to provide effective surface area for coating adhesion to the flat substrate and cross-linking in the coating network. Interactions at the interface between the coating and substrate include electrostatic interaction, hydrogen bonding, and van der Waals attraction. In the molecular dynamics simulations by Hasheminejad et al., the interfacial interaction energy between graphene oxide nanosheet and polylactide matrix is assigned to van der Waals forces and hydrogen bonds [62]. The bonding network of GO-SG-ZH nanosheets in the coating is another reason for the coating stability in environments simulating aqueous food.

Mechanical properties of polylactide films with nanosilica-based and graphene-based coatings

The thin coatings of SG and GO-SG-ZH considerably affected the mechanical properties of plastic films. Tensile testing results of blank PLA, SG/PLA, and GO-SG-ZH/PLA films are described in Figure 12 and summarized in Table 4. Additional data of measurement values and stress–strain curves are given in Supporting Information File 1, Table S1, Figure S4, Table S2, and Figure S5. Our previous paper presented that GO-ZnO coating on PLA film led to an increase of elastic modulus and a decrease of tensile elongation [14]. Similar trends were also noted in the tensile properties of coated PLA films in this study. Elastic moduli of SG/PLA and GO-SG-ZH/PLA films rose to 2447.08 ± 27.71 MPa and 2232.7 ± 105.52 MPa, which were respectively 31.89% and 20.34% higher than that of blank PLA film. Nanosilica and graphene-based nanosheets were nanostructures with high elastic modulus for reinforcement of PLA films through load transfer mechanism. High elasticity of SG and GO-SG-ZH coatings led to the increases in elastic moduli of the coated films. Besides, considerable decrease of elongation was observed due to the propagation of cracks from the coatings to the substrate. The tensile strength of the GO-SG-ZH/PLA film (54.22 ± 2.86 MPa) was slightly higher than that of the blank PLA film. The enhancement of tensile strength of the GO-SG-ZH/PLA film is explained due to the load transfer from the polylactide substrate to the graphene-based coating during the tensile process. Effective coating adhesion to the substrate and high elastic modulus of graphene-based nanosheets contributed to the higher tensile properties. Supporting Information File 1, Figure S6 shows SEM images of surfaces at the fracture of a GO-SG-ZH/PLA film generated by the tensile measurement.

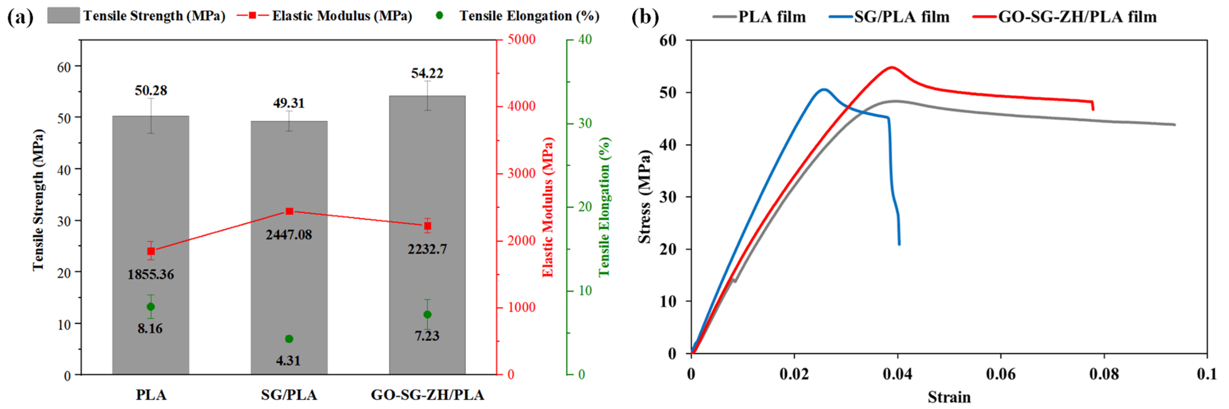

Figure 12: (a) Graph of tensile strength, elastic modulus, and tensile elongation. (b) Typical stress–strain curves of PLA, SG/PLA, and GO-SG-ZH/PLA films.

Table 4: Mechanical properties of blank PLA, SG/PLA, and GO-SG-ZH/PLA thin films.

Materials	Tensile strength (MPa)	Elastic modulus (MPa)	Tensile elongation (%)
PLA	50.28 ± 3.4	1855.36 ± 138.56	8.16 ± 1.43
SG/PLA	49.31 ± 1.93	2447.08 ± 27.71	4.31 ± 0.36
GO-SG-ZH/PLA	54.22 ± 2.86	2232.7 ± 105.52	7.23 ± 1.77

Conclusion

Supramolecular graphene-based hydrogels are bioinspired structures which are biomimetic to natural hydration structures of cellular membranes, proteins, and other biomolecules. While hydration shells participate in the shaping and dynamics of biological structures, water intercalation in graphene-based hydrogels is proposed to reduce intersheet van der Waals interaction, generate repulsive hydration forces, and facilitate hydration lubrication of graphene-based nanosheets. DFT calculations showed that a water layer in AB bilayer graphene enlarges the intersheet distance from 3.459 to 6.626 Å, and consequently leads to a reduction of 37.5% in intersheet binding energy of the van der Waals force. In our experiments, sustainable green chemistry approaches are used to synthesize graphene oxide, silica gel, nanosilica–zinc hydroxide, and graphene oxide–nanosilica–zinc hydroxide nanocomposites. The chemical methods used saved chemical reagents and production energy, converted rice hush ash waste into nanosilica, improved materials quality, and contributed to environmental sustainability. The GO-SG-ZH hydrogel is a supramolecular hydration structure with the advantages of aqueous dispersibility, antibacterial activity, and hydration lubrication. Water evaporation analysis suggested that the last 4% of water in the GO-SG-ZH hydrogel are interfacial hydration shells on graphene-based nanosheets. The first water shell is crucially responsible for primary hydration forces between nanostructures. Additionally, hydration lubrication is another interesting effect of water-intercalated graphene-based systems. As graphene-based nanosheets in the hydrogel structure are in non-stacking state, they can slide on each other owing to water lubrication and low interfacial friction. After brush coating and water evaporation, the graphene-based coating is adhered to the polylactide substrate through interfacial interactions. The GO-SG-ZH/PLA films showed antibacterial activity, coating stability, and enhanced tensile properties. In summary, the supramolecular hydration structure of graphene-based hydrogels is a prospective nanotechnology approach to advance nanoscale structures and interfaces for a variety of applications.

Supporting Information

Figure of SEM-EDS analyses of graphene-based powder and hydrogel, figures of nanocomposite hydrogel and its dispersions in water, figures and tables of tensile testing of coated polylactide films, and figure of SEM images of fractured polylactide nanocomposite films.

Supporting Information File 1

Additional figures and tables.
[https://www.beilstein-journals.org/bjnano/content/supplementary/2190-4286-16-61-S1.pdf]

Acknowledgements

The authors would like to acknowledge the research collaborations of Fundamental Materials Science Laboratory and Multifunctional Materials Laboratory (Faculty of Materials Science and Technology, University of Science, Vietnam National University Ho Chi Minh City), Laboratory for Computational Physics (Institute for Computational Science and Artificial Intelligence, Van Lang University), and School of Education (Can Tho University).

Author Contributions

Hon Nhien Le: conceptualization; data curation; formal analysis; funding acquisition; investigation; methodology; project administration; supervision; visualization; writing – original draft; writing – review & editing. Duy Khanh Nguyen: data curation; resources; software; writing – review & editing. Minh Triet Dang: resources; software. Huyen Trinh Nguyen: formal analysis; investigation. Thi Bang Tam Dao: data curation; resources. Trung Do Nguyen: data curation; resources. Chi Nhan Ha Thuc: resources; supervision; validation. Van Hieu Le: investigation; resources; supervision; validation; writing – review & editing.

ORCID® iDs

Hon Nhien Le - https://orcid.org/0000-0001-5397-7665
Minh Triet Dang - https://orcid.org/0000-0003-1769-4873

Data Availability Statement

Data generated and analyzed during this study is available from the corresponding author upon reasonable request.

Preprint

A non-peer-reviewed version of this article has been previously published as a preprint: https://doi.org/10.3762/bxiv.2025.4.v1

References

1. Chaplin, M. *Nat. Rev. Mol. Cell Biol.* **2006,** *7,* 861–866. doi:10.1038/nrm2021
2. Bellissent-Funel, M.-C.; Hassanali, A.; Havenith, M.; Henchman, R.; Pohl, P.; Sterpone, F.; van der Spoel, D.; Xu, Y.; Garcia, A. E. *Chem. Rev.* **2016,** *116,* 7673–7697. doi:10.1021/acs.chemrev.5b00664
3. Laage, D.; Elsaesser, T.; Hynes, J. T. *Chem. Rev.* **2017,** *117,* 10694–10725. doi:10.1021/acs.chemrev.6b00765
4. Konstantinovsky, D.; Perets, E. A.; Santiago, T.; Velarde, L.; Hammes-Schiffer, S.; Yan, E. C. Y. *ACS Cent. Sci.* **2022,** *8,* 1404–1414. doi:10.1021/acscentsci.2c00702
5. Valle-Delgado, J. J.; Molina-Bolívar, J. A.; Galisteo-González, F.; Gálvez-Ruiz, M. J. *Curr. Opin. Colloid Interface Sci.* **2011,** *16,* 572–578. doi:10.1016/j.cocis.2011.04.004
6. Donaldson, E. C.; Alam, W. Surface Forces. *Wettability;* Gulf Publishing: Houston, TX,USA, 2008; pp 57–119. doi:10.1016/b978-1-933762-29-6.50008-9
7. Israelachvili, J. N. Interactions of Biological Membranes and Structures. *Intermolecular and Surface Forces,* 3rd ed.; Academic Press: Burlington, MA, USA, 2011; pp 577–616. doi:10.1016/b978-0-12-375182-9.10021-1
8. West, A. Intermolecular Forces and Solvation. In *Interface Science and Technology;* Ball, V., Ed.; Self-Assembly Processes at Interfaces, Vol. 21; Academic Press: London, UK, 2018; pp 49–130. doi:10.1016/b978-0-12-801970-2.00002-1
9. Pérez, E. M.; Martín, N. *Chem. Soc. Rev.* **2015,** *44,* 6425–6433. doi:10.1039/c5cs00578g
10. Luo, J.; Kim, J.; Huang, J. *Acc. Chem. Res.* **2013,** *46,* 2225–2234. doi:10.1021/ar300180n
11. Li, J.; Östling, M. *Crystals* **2013,** *3,* 163–190. doi:10.3390/cryst3010163
12. Yang, X.; Zhu, J.; Qiu, L.; Li, D. *Adv. Mater. (Weinheim, Ger.)* **2011,** *23,* 2833–2838. doi:10.1002/adma.201100261
13. Le, N. H.; Seema, H.; Kemp, K. C.; Ahmed, N.; Tiwari, J. N.; Park, S.; Kim, K. S. *J. Mater. Chem. A* **2013,** *1,* 12900. doi:10.1039/c3ta12735d
14. Le, H. N.; Nguyen, T. B. Y.; Nguyen, D. T. T.; Dao, T. B. T.; Nguyen, T. D.; Ha Thuc, C. N. *Nanotechnology* **2024,** *35,* 305601. doi:10.1088/1361-6528/ad40b8
15. Le, H. N.; Dao, T. B. T.; Nguyen, T. D.; Dinh, D. A.; Ha Thuc, C. N.; Le, V. H. *RSC Adv.* **2024,** *14,* 30844–30858. doi:10.1039/d4ra05385k
16. Le, H. N.; Thai, D.; Nguyen, T. T.; Dao, T. B. T.; Nguyen, T. D.; Tieu, D. T.; Ha Thuc, C. N. *J. Mater. Res. Technol.* **2023,** *24,* 4440–4453. doi:10.1016/j.jmrt.2023.04.050
17. Le, H. N.; Nguyen, H. D.; Do, M. H.; Nguyen, T. M. H.; Nguyen, T. D.; Dao, T. B. T.; Dinh, D. A.; Thuc, C. N. H. *Polym.-Plast. Technol. Mater.* **2024,** *63,* 1421–1437. doi:10.1080/25740881.2024.2335186
18. Varma, R. S. *ACS Sustainable Chem. Eng.* **2016,** *4,* 5866–5878. doi:10.1021/acssuschemeng.6b01623
19. Mor, S.; Manchanda, C. K.; Kansal, S. K.; Ravindra, K. *J. Cleaner Prod.* **2017,** *143,* 1284–1290. doi:10.1016/j.jclepro.2016.11.142
20. Abdul Razak, N. A.; Othman, N. H.; Mat Shayuti, M. S.; Jumahat, A.; Sapiai, N.; Lau, W. J. *J. Environ. Chem. Eng.* **2022,** *10,* 107322. doi:10.1016/j.jece.2022.107322
21. Le, H. N.; Dang, T. M. T.; Le, T. T.; Dao, T. B. T.; Nguyen, T. D.; Ha Thuc, C. N. *Nat. Sci.* **2025,** in press.
22. Berland, K.; Cooper, V. R.; Lee, K.; Schröder, E.; Thonhauser, T.; Hyldgaard, P.; Lundqvist, B. I. *Rep. Prog. Phys.* **2015,** *78,* 066501. doi:10.1088/0034-4885/78/6/066501
23. Grimme, S.; Antony, J.; Schwabe, T.; Mück-Lichtenfeld, C. *Org. Biomol. Chem.* **2007,** *5,* 741–758. doi:10.1039/b615319b
24. Grimme, S.; Antony, J.; Ehrlich, S.; Krieg, H. *J. Chem. Phys.* **2010,** *132,* 154104. doi:10.1063/1.3382344
25. Kumar, A.; Vemula, P. K.; Ajayan, P. M.; John, G. *Nat. Mater.* **2008,** *7,* 236–241. doi:10.1038/nmat2099
26. Thi Nguyen, T.; Pham, B.-T. T.; Nhien Le, H.; Bach, L. G.; Thuc, C. N. H. *Food Packag. Shelf Life* **2022,** *32,* 100830. doi:10.1016/j.fpsl.2022.100830
27. Le, H. N.; Nguyen, L. N. L.; Dao, T. B. T.; Nguyen, T. D.; Ha Thuc, C. N. *Int. J. Nanotechnol.* **2025,** in press.
28. Yildiz, G.; Bolton-Warberg, M.; Awaja, F. *Acta Biomater.* **2021,** *131,* 62–79. doi:10.1016/j.actbio.2021.06.047
29. Birowska, M.; Milowska, K.; Majewski, J. A. *Acta Phys. Pol., A* **2011,** *120,* 845–848. doi:10.12693/aphyspola.120.845
30. Song, R.; Feng, W.; Jimenez-Cruz, C. A.; Wang, B.; Jiang, W.; Wang, Z.; Zhou, R. *RSC Adv.* **2015,** *5,* 274–280. doi:10.1039/c4ra13736a

31. Rêgo, C. R. C.; Oliveira, L. N.; Tereshchuk, P.; Da Silva, J. L. F. *J. Phys.: Condens. Matter* **2015,** *27,* 415502. doi:10.1088/0953-8984/27/41/415502
32. Khan, M. I. H.; Farrell, T.; Nagy, S. A.; Karim, M. A. *Sci. Rep.* **2018,** *8,* 15191. doi:10.1038/s41598-018-33159-7
33. Israelachvili, J.; Wennerström, H. *Nature* **1996,** *379,* 219–225. doi:10.1038/379219a0
34. Liang, Y.; Hilal, N.; Langston, P.; Starov, V. *Adv. Colloid Interface Sci.* **2007,** *134–135,* 151–166. doi:10.1016/j.cis.2007.04.003
35. Parsegian, V. A.; Zemb, T. *Curr. Opin. Colloid Interface Sci.* **2011,** *16,* 618–624. doi:10.1016/j.cocis.2011.06.010
36. Lang, X.; Shi, L.; Zhao, Z.; Min, W. *Nat. Commun.* **2024,** *15,* 5271. doi:10.1038/s41467-024-49404-9
37. Harrellson, S. G.; DeLay, M. S.; Chen, X.; Cavusoglu, A.-H.; Dworkin, J.; Stone, H. A.; Sahin, O. *Nature* **2023,** *619,* 500–505. doi:10.1038/s41586-023-06144-y
38. Huang, H.; Park, H.; Huang, J. *Chem* **2022,** *8,* 2432–2441. doi:10.1016/j.chempr.2022.05.016
39. Vijayan, S.; Arjunan, T. V.; Kumar, A. Fundamental Concepts of Drying. In *Solar Drying Technology;* Prakash, O.; Kumar, A., Eds.; Green Energy and Technology; Springer: Singapore, 2017; pp 3–38. doi:10.1007/978-981-10-3833-4_1
40. Wang, M.; Jiang, L.; Kim, E. J.; Hahn, S. H. *RSC Adv.* **2015,** *5,* 87496–87503. doi:10.1039/c5ra17024a
41. Otis, G.; Ejgenberg, M.; Mastai, Y. *Nanomaterials* **2021,** *11,* 238. doi:10.3390/nano11010238
42. Wang, M.; Zhou, Y.; Zhang, Y.; Hahn, S. H.; Kim, E. J. *CrystEngComm* **2011,** *13,* 6024. doi:10.1039/c1ce05502j
43. Song, X.; Boily, J.-F. *Environ. Sci. Technol.* **2013,** *47,* 7171–7177. doi:10.1021/es400147a
44. Liu, Y.; Shen, J.; Zhao, L.; Wang, W.; Gong, W.; Zheng, F. *RSC Adv.* **2020,** *10,* 9146–9154. doi:10.1039/d0ra00308e
45. Wang, Y.; Chen, S.; Qiu, L.; Wang, K.; Wang, H.; Simon, G. P.; Li, D. *Adv. Funct. Mater.* **2015,** *25,* 126–133. doi:10.1002/adfm.201402952
46. Zhan, H.; Xiong, Z.; Cheng, C.; Liang, Q.; Liu, J. Z.; Li, D. *Adv. Mater. (Weinheim, Ger.)* **2020,** *32,* 1904562. doi:10.1002/adma.201904562
47. Ikura, R.; Park, J.; Osaki, M.; Yamaguchi, H.; Harada, A.; Takashima, Y. *NPG Asia Mater.* **2022,** *14,* 10. doi:10.1038/s41427-021-00349-1
48. Su, L.; Sun, J.; Ding, F.; Gao, Y.; Gao, X.; Zheng, L. *Appl. Surf. Sci.* **2021,** *567,* 150840. doi:10.1016/j.apsusc.2021.150840
49. Bepete, G.; Anglaret, E.; Ortolani, L.; Morandi, V.; Huang, K.; Pénicaud, A.; Drummond, C. *Nat. Chem.* **2017,** *9,* 347–352. doi:10.1038/nchem.2669
50. Suter, J. L.; Coveney, P. V. *Sci. Rep.* **2021,** *11,* 22460. doi:10.1038/s41598-021-01626-3
51. Klein, J. *Friction* **2013,** *1,* 1–23. doi:10.1007/s40544-013-0001-7
52. Ma, L.; Gaisinskaya-Kipnis, A.; Kampf, N.; Klein, J. *Nat. Commun.* **2015,** *6,* 6060. doi:10.1038/ncomms7060
53. Soler-Crespo, R. A.; Gao, W.; Mao, L.; Nguyen, H. T.; Roenbeck, M. R.; Paci, J. T.; Huang, J.; Nguyen, S. T.; Espinosa, H. D. *ACS Nano* **2018,** *12,* 6089–6099. doi:10.1021/acsnano.8b02373
54. Ma, P.; Liu, Y.; Han, K.; Tian, Y.; Ma, L. *Friction* **2024,** *12,* 591–605. doi:10.1007/s40544-023-0750-x
55. Ge, X.; Chai, Z.; Shi, Q.; Liu, Y.; Wang, W. *Friction* **2023,** *11,* 1953–1973. doi:10.1007/s40544-022-0681-y
56. Cao, G.; Yan, J.; Ning, X.; Zhang, Q.; Wu, Q.; Bi, L.; Zhang, Y.; Han, Y.; Guo, J. *Colloids Surf., B* **2021,** *200,* 111588. doi:10.1016/j.colsurfb.2021.111588
57. Palmieri, V.; Lauriola, M. C.; Ciasca, G.; Conti, C.; De Spirito, M.; Papi, M. *Nanotechnology* **2017,** *28,* 152001. doi:10.1088/1361-6528/aa6150
58. Han, W.; Wu, Z.; Li, Y.; Wang, Y. *Chem. Eng. J.* **2019,** *358,* 1022–1037. doi:10.1016/j.cej.2018.10.106
59. Srivastava, M.; Singh, K. R.; Singh, T.; Asiri, M.; Suliman, M.; Sabia, H.; Deen, P. R.; Chaube, R.; Singh, J. *Int. J. Biol. Macromol.* **2023,** *253,* 126886. doi:10.1016/j.ijbiomac.2023.126886
60. Mendes, C. R.; Dilarri, G.; Forsan, C. F.; Sapata, V. d. M. R.; Lopes, P. R. M.; de Moraes, P. B.; Montagnolli, R. N.; Ferreira, H.; Bidoia, E. D. *Sci. Rep.* **2022,** *12,* 2658. doi:10.1038/s41598-022-06657-y
61. Bartoli, M.; Cardano, F.; Piatti, E.; Lettieri, S.; Fin, A.; Tagliaferro, A. *Beilstein J. Nanotechnol.* **2024,** *15,* 1041–1053. doi:10.3762/bjnano.15.85
62. Hasheminejad, K.; Montazeri, A. *Appl. Surf. Sci.* **2020,** *502,* 144150. doi:10.1016/j.apsusc.2019.144150

License and Terms

BEILSTEIN JOURNAL OF NANOTECHNOLOGY

Facile one-step radio frequency magnetron sputtering of Ni/NiO on stainless steel for an efficient electrode for hydrogen evolution reaction

Ha Huu Do[1], Khac Binh Nguyen[1], Phuong N. Nguyen[2] and Hoai Phuong Pham*[1]

Full Research Paper

Open Access

Address:
[1]NTT Hi-Tech Institute, Nguyen Tat Thanh University, Ho Chi Minh City 700000, Vietnam and [2]Institute of Applied Materials Science, Vietnam Academy of Science and Technology (VAST), 29TL Street, Ward Thanh Loc, District 12, Ho Chi Minh City 700000, Vietnam

Email:
Hoai Phuong Pham* - phphuong@ntt.edu.vn

* Corresponding author

Keywords:
electrocatalysts; magnetron sputtering; nickel; nickel oxide; water electrolysis

Beilstein J. Nanotechnol. **2025,** *16,* 837–846.
https://doi.org/10.3762/bjnano.16.63

Received: 12 February 2025
Accepted: 20 May 2025
Published: 06 June 2025

This article is part of the thematic issue "Emerging technologies and nanomaterials for sustainability".

Guest Editor: V. V. Pham

Abstract

The advancement of affordable, ultrastable, and efficient electrode materials for basic hydrogen evolution reaction (HER) plays a crucial role in industrial hydrogen manufacture, resolving problems caused by carbon dioxide emissions. Ni-based electrocatalysts have been well accepted as potential candidates to replace Pt-based electrocatalysts for HER because of their suitable Gibbs free hydrogen adsorption energy, good intrinsic catalytic properties, and high stability. However, solution-based synthetic approaches can be highly harmful to human beings. In this study, Ni/NiO nanolayers were prepared on stainless steel (SS) via a facile one-step radio frequency magnetron sputtering with various O_2 flow rates. The O_2 flow rate not only changed the crystal phase but also affected the morphology and atomic ratio of materials, leading to optimized HER efficiency. The evaluation of catalytic activities revealed that the optimal sample of Ni/NiO/SS-10 displayed a higher HER performance than bare SS. To produce H_2 at a current density of 10 $mA\cdot cm^{-2}$, this electrode required a low overpotential of 184 mV and demonstrated remarkable durability over 12 h of operation. The high efficiency is attributed to the collaborative work of the NiO and Ni metal components and the good electrical conductivity of SS, which is advantageous for dissociative adsorption of water molecules, recombination of hydrogen atoms, and improvement of electronic/ionic motion. This work may introduce a facile and eco-friendly strategy for fabricating noble metal-free, efficient nanomaterials for electrocatalytic HER.

Introduction

The world is facing a critical challenge through the increasing consumption of fossil fuels, causing CO_2 emissions and resulting in climate change [1]. Hydropower can be harnessed to provide sustainable energy for future generations because there are no harmful emissions with only water vapor as a byproduct [2-4]. Also, hydropower offers better energy efficiency compared to gasoline, coal, and natural gas. Currently, hydrogen produced by water electrolysis is well accepted as an ecologically clean, sustainable method compared to other techniques, such as coal gasification and steam methane reforming [5-10]. According to reported works, Pt catalysts were recognized as the best material for electrochemical hydrogen evolution reaction (HER) [11-13]. However, it is challenging to use Pt-based nanomaterials for industrial applications because of their non-abundance and high cost. As a result, many studies have explored Pt-free catalysts, such as MoS_2, WS_2, $CoSe_2$, and $NiSe_2$, which displayed potential performance in acidic media [14-16]. However, their HER efficacy is poor in alkaline environments because of the lack of available protons, resulting in a high required voltage to cleave H–OH bonds. To resolve this problem, many groups fabricated metal/metal oxide-based nanomaterials using various solution-based methods for alkaline HER because of the efficacy of metal oxides in breaking water molecules. In this context, Ni/NiO-based nanomaterials were evaluated as promising catalysts for industrial applications because of their Gibbs free energy of hydrogen/water adsorption. Also, inexpensiveness and high durability are positive aspects regarding large-scale applications. For instance, Oshchepkov and coworkers revealed that the efficacy of NiO in cleaving H–OH bonds accelerated the formation of hydrogen on a Ni metal catalyst [17]. Yan and coworkers prepared Ni/NiO nanosheets via a hydrothermal process and annealing, which gave a high HER efficiency [18]. Wang et al. found that Ni metal plays a crucial role in NiO_x-based material for water electrolysis [19]. However, using chemical methods to fabricate Ni/NiO-based nanomaterials is accompanied by toxic solvents and gases, influencing the environment and people's health. One of the most significant current discussions in water electrolysis is finding green methods to prepare high-efficiency electrocatalysts. Thus, vacuum physical techniques have gained considerable attention in synthesizing electrode materials in recent years because they offer a cleaner pathway than solution-based synthetic processes [20-22]. Among vacuum deposition methods, magnetron sputtering has been widely applied in industrial applications for fabricating thin films because of its advantages, such as good adhesion and uniform distribution of materials on various substrates [23-25]. For instance, Ren et al. used the magnetron sputtering method to introduce Si into an iridium electrode to achieve efficient water electrolysis [26]. Additionally, this technique's fast deposition rate and high level of the preserved substrate are definite advantages. Although studies have recognized the effectiveness of magnetron sputtering, research has yet to systematically investigate the effect of the O_2 flow rate on the HER efficiency of Ni/NiO catalysts.

Commercial stainless steel (SS) costs less than other conductive substrates such as nickel foam (NF), carbon cloth, and fluorine-doped tin oxide [27-29]. Also, SS displays high electrical conductivity, outstanding chemical stability, and good mechanical properties. Therefore, numerous researchers have used SS as a template to deposit nanomaterials using various electrocatalytic applications [30]. For instance, Wang et al. deposited nickel–iron on SS, which was used as a high-performance electrode for water oxidation [31]. Hence, in this study, we utilized commercial 304 SS and coated it with the Ni/NiO catalyst through a one-step radio frequency (RF) magnetron sputtering route with various O_2 flow rates, including 5, 10, 15, and 20 sccm. The electrode showed a higher HER efficacy than SS and Ni/SS, indicating the crucial role of NiO in water splitting. Moreover, the optimal sample Ni/NiO/SS-10 exhibited remarkable durability after 12 h of operation, suggesting great potential regarding industrial application.

Results and Discussion

Crystal structure and phase of the as-synthesized electrodes were verified by X-ray diffraction (XRD) measurements with 2θ ranging from 20° to 80°. Figure 1 displays the XRD patterns

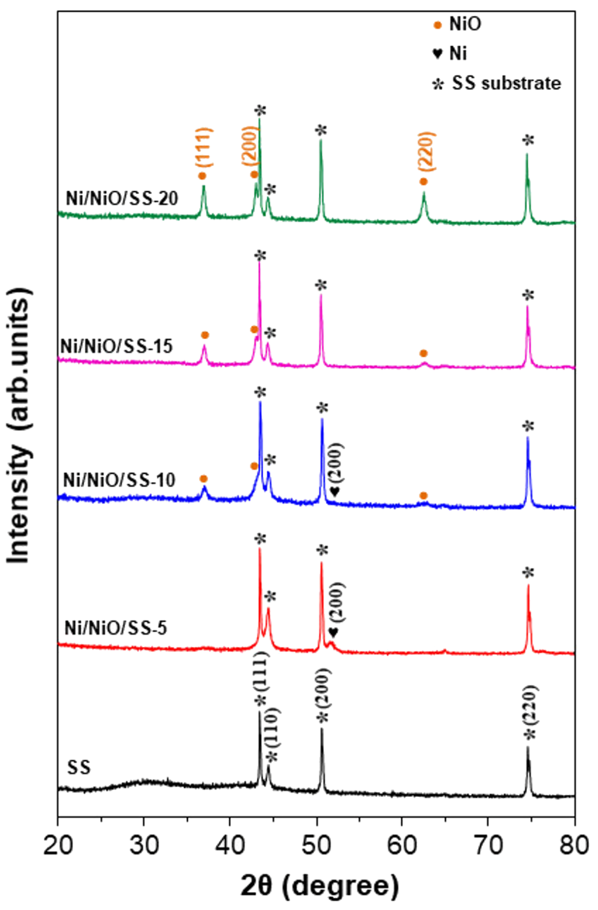

Figure 1: XRD patterns of SS, Ni/NiO/SS-5, Ni/NiO/SS-10, Ni/NiO/SS-15, and Ni/NiO/SS-20 electrodes.

of SS, Ni/NiO/SS-5, Ni/NiO/SS-10, Ni/NiO/SS-15, and Ni/NiO/SS-20 electrodes. Regarding the commercial 304 SS sample, the typical peaks at 43.64°, 50.68°, and 74.56° were indexed to the (111), (200), and (220) crystal planes of the cubic γ-Ni–Cr–Fe phase [27-33]. At a low O_2 flow rate (5 sccm), a Ni metal phase appeared, visible by the peak at 51.9°, identical to the Ni/SS sample (Supporting Information File 1, Figure S1), whereas the NiO phase also began to appear with low-intensity peaks. When the O_2 flow rate was increased from 10 to 20 sccm in the synthetic process, the peak intensity of the NiO phase was enhanced. More importantly, the XRD image of Ni/NiO/SS-10 presents peaks at 37.20°, 43.21°, and 62.91°, which correspond to the (111), (200), and (220) planes of the NiO phase (PDF 00-004-0835) [34,35]. Meanwhile, the peak of the Ni metal phase still appeared in the Ni/NiO/SS-10 sample, proving the co-existence of metal and metal oxide phases, offering a potential for HER. These outcomes indicated the successful Ni/NiO thin film fabrication on SS substrates. The uniformity of the electrocatalyst material is a vital factor that has a direct effect on electrode performance.

Scanning electron microscopy (SEM) was carried out to analyze the morphology of the Ni/NiO thin film on the SS substrate. The as-synthesized Ni/NiO film at 5 sccm of O_2 flow rate showed uniform and continuous appearance on the entire surface of the SS substrate (Figure 2a,e). However, at high O_2 flow rates, the surface of Ni/NiO/SS-10, Ni/NiO/SS-15, and Ni/NiO/SS-20 electrodes became rougher, as shown in Figure 2b–d, which was attributed to a higher metal oxide content. More importantly, the composition of the samples (wt %) changed with different O_2 flow rates in the sputtering process. The proportion of O increases when the O_2 flow rate is increased, determined by energy-dispersive X-ray spectroscopy (EDX), as shown in Table 1. Ni/NiO/SS-5 displayed the lowest O content (4.69 wt %). In contrast, Ni/NiO/SS-20 showed the highest O content (22.69 wt %), attributed to the highest O_2 flow rate in the sputtering process. Ni/NiO/SS-10 exhibited a moderate O_2 content (11.96 wt %), which could bring the highest HER efficiency. The Ni/NiO ratio is the most crucial parameter in the Ni/NiO catalyst system, influencing the electrode's HER efficiency, which Yan and coworkers proved [18].

Table 1: Nickel and oxygen fractions from EDX analyses.

Electrodes	Ni (wt %)	O (wt %)
Ni/NiO/SS-5	95.31	4.69
Ni/NiO/SS-10	88.04	11.96
Ni/NiO/SS-15	82.93	17.07
Ni/NiO/SS-20	77.31	22.69

The Raman spectrum of the Ni/NiO/SS-10 electrode displayed the prominent peaks shown in Figure 3. The bands at 200 to 600 cm^{-1} represent one phonon (1P), whereas the bands at 650 to 1100 cm^{-1} could be assigned to two phonons (2P) of NiO species in the electrode. In particular, the Raman peak at 552 cm^{-1} was indexed into the 1P longitudinal optical (LO) mode, whereas the peak at 1052 cm^{-1} is attributed to the $2P_{LO}$ mode of the Ni–O bonds. These peaks indicate the existence of

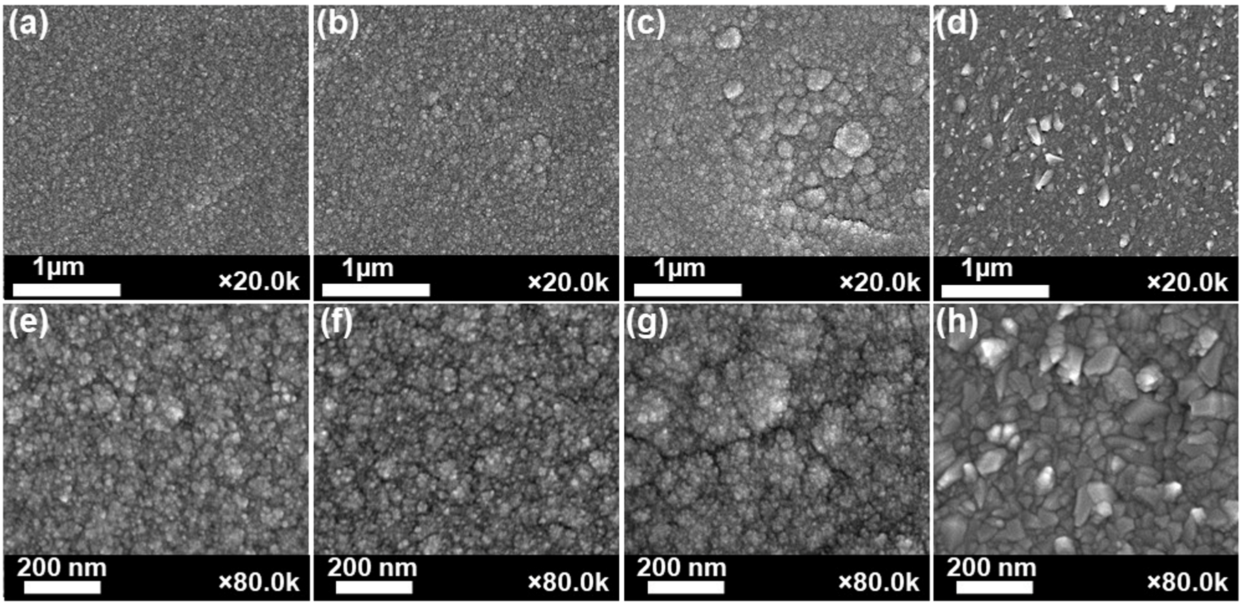

Figure 2: SEM images of (a, e) Ni/NiO/SS-5, (b, f) Ni/NiO/SS-10, (c, g) Ni/NiO/SS-15, and (d, h) Ni/NiO/SS-20 electrodes.

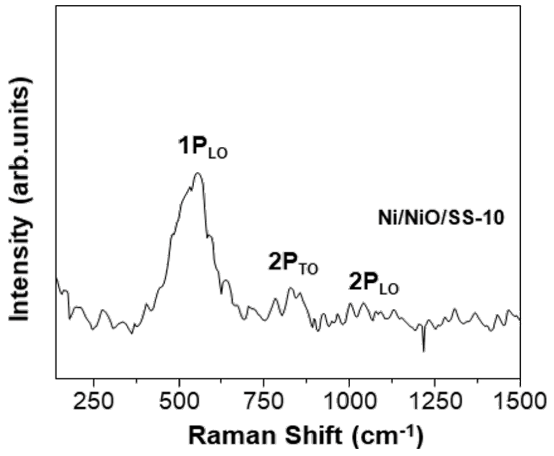

Figure 3: Raman spectrum of the Ni/NiO/SS-10 electrode.

Ni defects in the Ni/NiO/SS-10 sample, which is favorable for electrocatalytic applications [36-38]. Additionally, Figure 4 depicts EDX analysis and proves the uniform distribution of the primary elements (Ni, O) in the Ni/NiO/SS-10 sample. This outcome revealed that catalytic sites were also uniformly distributed on the electrode's surface. Figure 5a exhibits the X-ray photoelectron spectroscopy (XPS) survey of the Ni/NiO/SS-10 sample. It can be seen that Ni/NiO/SS gives Ni and O peaks. The chemical state of Ni is further analyzed by the Ni 2p$_{3/2}$ peaks. As depicted in Figure 5b, the Ni 2p$_{3/2}$ spectrum can be deconvoluted into four peaks. The peaks at 852.8, 853.7, and 855.8 eV correspond to Ni^0, Ni^{2+}, and Ni^{3+}, respectively. Another broad peak at nearly 861 eV is attributed to a satellite peak. The presence of Ni^{3+} can be ascribed to the formation of NiOOH species originating from water adsorption on the surface of NiO. The high-resolution O 1s spectrum can be decon-

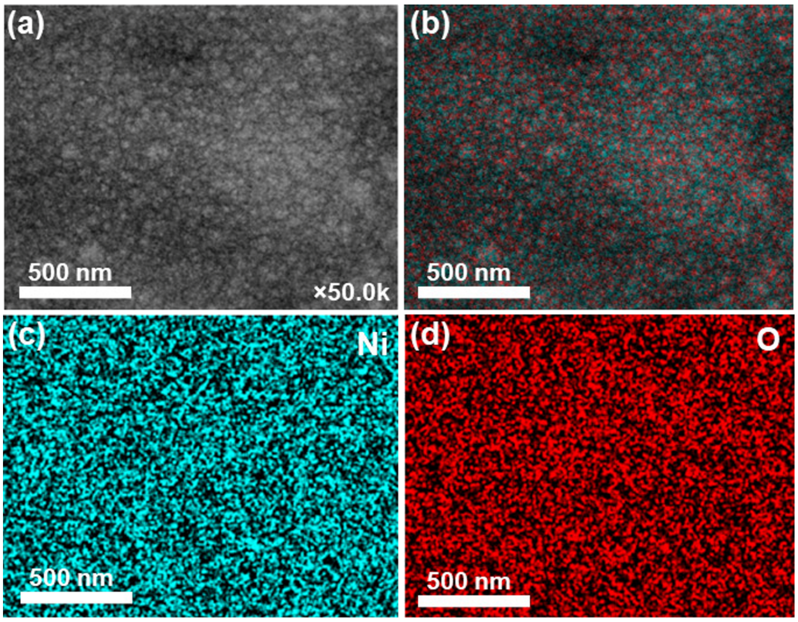

Figure 4: (a) SEM image, (b) overall element mapping, and (c) nickel and (d) oxygen element mapping of the Ni/NiO/SS-10 sample.

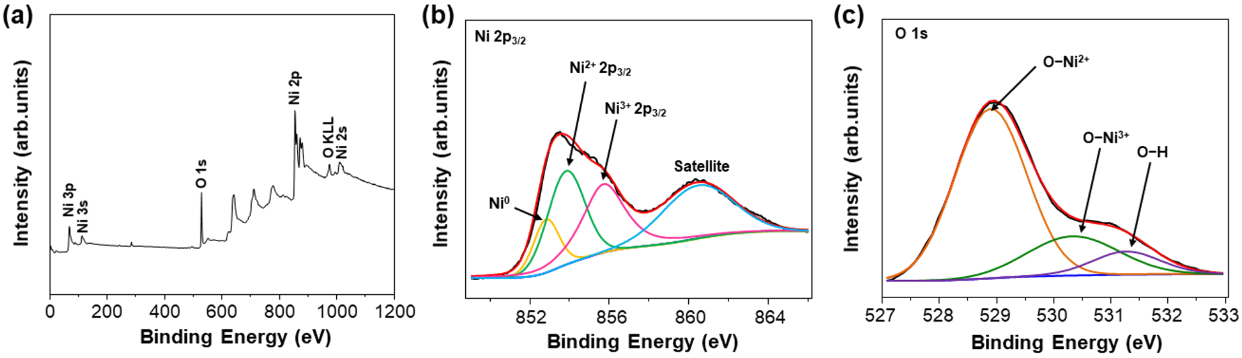

Figure 5: (a) Survey XPS spectrum of Ni/NiO/SS-10. High-resolution XPS spectra of (b) Ni 2p$_{3/2}$ and (c) O 1s.

voluted into three peaks, namely, O–Ni^{2+} (528.9 eV), O–Ni^{3+} (530.5 eV), and O–H (531.4 eV) [39].

To find the optimal O_2 flow rate for HER applications, we evaluated the HER catalytic activities of the SS, Ni/NiO/SS-5, Ni/NiO/SS-10, Ni/NiO/SS-15, and Ni/NiO/SS-20 electrodes. Linear sweep voltammetry (LSV) of electrodes was studied in a solution of 1.0 M KOH. As shown in Figure 6a, Ni/NiO/SS-10 provides better HER efficacy than other as-synthesized catalysts. To reach a cathodic current density of 10 mA·cm^{-2}, SS, Ni/NiO/SS-5, Ni/NiO/SS-10 Ni/NiO/SS-15, and Ni/NiO/SS-20 electrodes needed overpotentials of 431, 247, 184, 326, and 382 mV vs RHE, respectively. A smaller overpotential implies a smaller energy barrier for water electrolysis to produce hydrogen. These outcomes indicate that Ni/NiO/SS-10 shows the highest HER efficiency among the investigated electrodes. Its overpotential is comparable with Ni-based nanomaterials in the literature, as depicted in Table 2 [40-48]. Specifically, the overvoltage of Ni/NiO/SS-10 is lower than those of NiO/C (565 mV) [40], Ni_3S_2/NC (199 mV) [44], NiCoP/rGO (209 mV) [47], and NF-Ni_3Se_2/Ni (203 mV) [48]. Also, the Tafel slopes indicate that the reaction kinetics of the Ni/NiO/SS-10 electrode is faster than those of the other electrodes (Figure 6b). Notably, the Tafel slopes are 161.1, 103.5, 90.5, 109.9, and 129.7 mV·dec^{-1} for SS, Ni/NiO/SS-5, Ni/NiO/SS-10, Ni/NiO/SS-15, and Ni/NiO/SS-20 electrodes, respectively. Moreover, the Tafel slope value of Ni/NiO/SS-10 is lower than the published ones of Ni/NiO (114 mV·dec^{-1}) [41], NiP_2/NiO (94 mV·dec^{-1}) [45], Ni_5P_4 (98 mV·dec^{-1}) [46], and NiCoP/rGO (124.1 mV·dec^{-1}) [47]. Generally, Tafel slopes are used to determine the HER mechanism, which could follow the Volmer–Heyrovsky or Volmer–Tafel pathway [49]. In this work, the Tafel value of Ni/NiO/SS-10 is between 40 and 120 mV·dec^{-1}, revealing that the HER mechanism follows the Volmer–Heyrovsky mechanism.

During the electrocatalytic process, the NiO components are crucial in facilitating the dissociative adsorption of water mole-

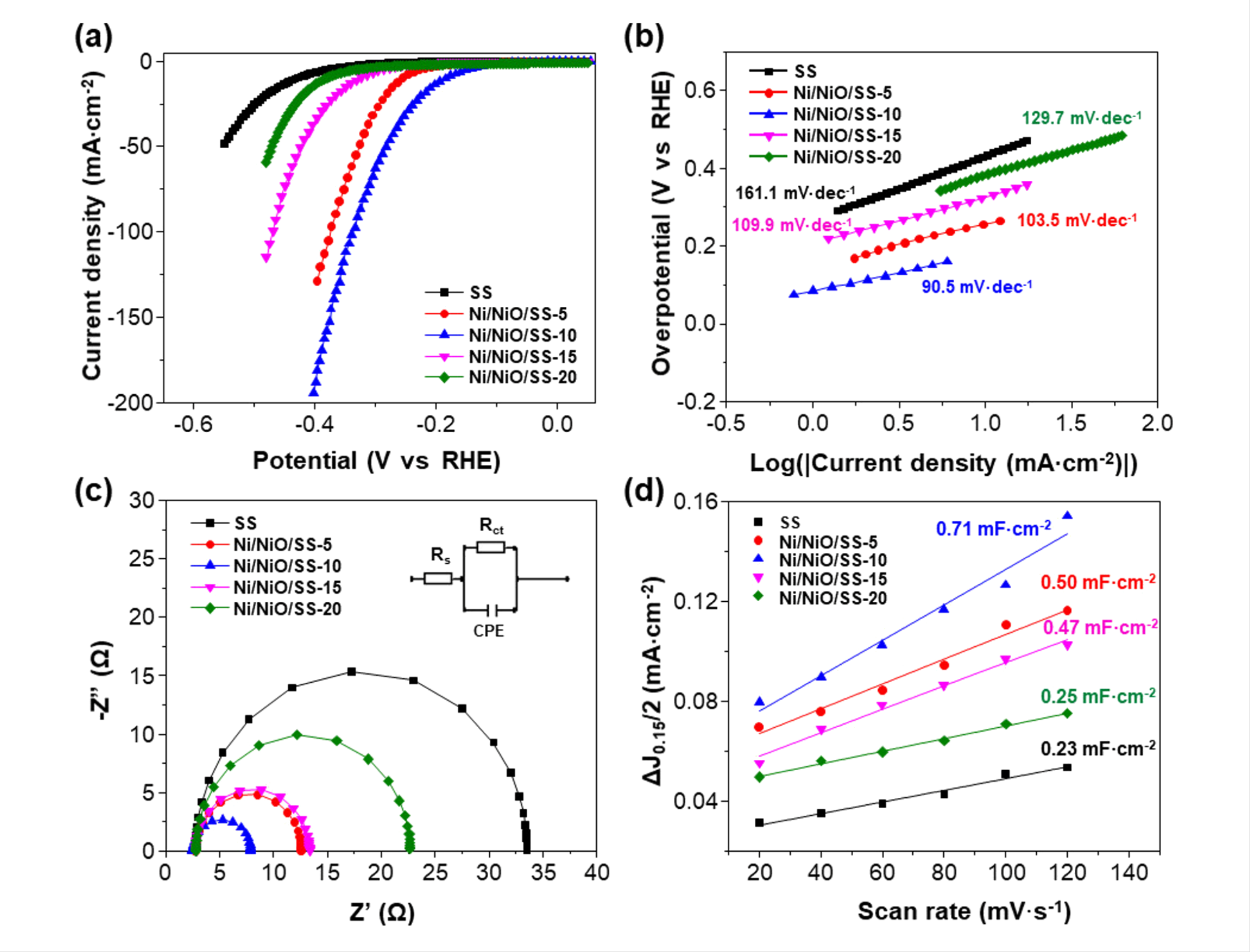

Figure 6: (a) Polarization curves of SS, Ni/NiO/SS-5, Ni/NiO/SS-10, Ni/NiO/SS-15, and Ni/NiO/SS-20 electrodes. (b) Corresponding Tafel slopes of electrodes. (c) Nyquist plots of different samples recorded at a potential of −200 mV vs RHE. (d) Double-layer capacitances obtained using cyclic voltammetry (CV).

Table 2: Summary of alkaline HER performance for various Ni-based electrocatalysts.

Catalysts	Current density (mA·cm^{-2})	Overpotential (mV)	Tafel slope (mV·dec^{-1})	Reference
NiO/C	10	565	77.8	[40]
Ni/NiO	10	120	114	[41]
N-NiO	10	154	90	[42]
Ni_3S_2@2DCo-MOF	10	140	90.3	[43]
Ni_3S_2/NC	10	199	72	[44]
NiP_2/NiO	10	≈131	94	[45]
Ni_5P_4	10	49	98	[46]
NiCoP/rGO	10	209	124.1	[47]
NF-Ni_3Se_2/Ni	10	203	79	[48]
NiO/SnO_2	10	157	155	[50]
NiO@TiO_2	10	144	152.34	[51]
Ni/NiO/SS-10	10	184	90.5	this work

cules to generate adsorbed H atoms (H_{ads}). Also, NiO units are vital in scavenging OH^- ions, which could reduce the catalytic activity of metallic Ni phases [52]. Meanwhile, metallic Ni phases favor the recombination of H_{ads} to produce H_2 gas, implying a perfect pair of Ni/NiO for the HER catalytic process [53-55]. Therefore, the Ni/NiO/SS-10 electrode exhibits higher HER activity than SS and Ni/SS, as shown in Supporting Information File 1, Figure S2. More importantly, the highest HER efficiency of the Ni/NiO/SS-10 electrode could be explained as follows: At a low O_2 flow rate (5 sccm), NiO is formed with low content, resulting in a decrease in the dissociative adsorption of water molecules. In contrast, at high O_2 flow rates (15 and 20 sccm), NiO is produced with a large ratio of NiO/Ni, which is indicated by XRD peaks of NiO with high intensity. A high NiO concentration prefers the dissociative adsorption of water molecules, while hydrogen desorption is limited. Besides, the O content increased in the order of Ni/NiO/SS-5 < Ni/NiO/SS-10 < Ni/NiO/SS-15 < Ni/NiO/SS-20, confirmed by EDX analysis. Overall, the material obtained at 10 sccm O_2 flow rate has the most suitable O/Ni ratio among the four materials and thus exhibited the best HER efficiency [18].

Electrochemical impedance spectroscopy (EIS) was carried out at a voltage of −200 mV to confirm the HER kinetics. Figure 6c shows the Nyquist plots of the various electrodes accompanied by an equivalent circuit (inset of Figure 6c). Ni/NiO/SS-10 has a charge transfer resistance (R_{ct}) of 5.35 Ω, which is much smaller than that of SS (30.75 Ω), Ni/NiO/SS-5 (9.79 Ω), Ni/NiO/SS-15 (10.58 Ω), and Ni/NiO/SS-20 (19.87 Ω). The lowest R_{ct} of Ni/NiO/SS-10 indicates the best electron/ion transfer kinetics for HER, consistent with the Tafel slope analysis. In general, the electrochemical surface area (ECSA) can be predicted by measuring the double-layer capacitance (C_{dl}), which is derived from the CV technique at various scan rates, ranging from 20 to 120 mV·s^{-1}, as depicted in Suporting Information File 1, Figure S4. Notably, the C_{dl} of Ni/NiO/SS-10 is 0.71 mF·cm^{-2}, which is higher than those of Ni/NiO/SS-5 (0.50 mF·cm^{-2}), Ni/NiO/SS-15 (0.47 mF·cm^{-2}), Ni/NiO/SS-20 (0.25 mF·cm^{-2}), and SS (0.23 mF·cm^{-2}), offering its higher ECSA along with a remarkable HER efficacy (Figure 6d).

To assess the intrinsic catalytic properties, the LSV curves were normalized to the ECSA, as displayed in Figure 7a. Ni/NiO/SS-10 presents a better intrinsic HER catalytic activity than the other samples. Also, the turnover frequency (TOF) is a vital factor for investigating the intrinsic catalytic activities of electrodes for the HER [56]. Hence, we determined the TOF of different electrodes at an overpotential of 200 mV for comparison. The TOF of Ni/NiO/SS-10 is 0.051 s^{-1}, which is higher than those of Ni/NiO/SS-5 (0.010 s^{-1}), Ni/NiO/SS-15 (0.008 s^{-1}), and Ni/NiO/SS-20 (0.004 s^{-1}), as shown in Figure 7b. This outcome implies that Ni/NiO/SS-10 exhibits a better efficiency regarding the active sites in the electrocatalytic HER process. Finally, we evaluated the long-term electrochemical stability of the Ni/NiO/SS-10 electrode via three methods, that is, chronopotentiometry, CV, and chronoamperometry. The potential–time response revealed that approximately 91% of the initial voltage is retained after 12 h of continuous hydrogen production at a cathodic current density of 10 mA·cm^{-2} (Figure 7c). Also, the LSV curve of Ni/NiO/SS-10 exhibits minimal changes after 2000 cycles (inset of Figure 7c). Additionally, the current density was maintained during the 12 h testing of chronoamperometry, as depicted in Figure 7d. This indicates the high stability of the Ni/NiO/SS-10 electrode for alkaline water electrolysis. To explain the high HER efficiency of the Ni/NiO/SS-10 electrode, we analyzed SEM and EDX

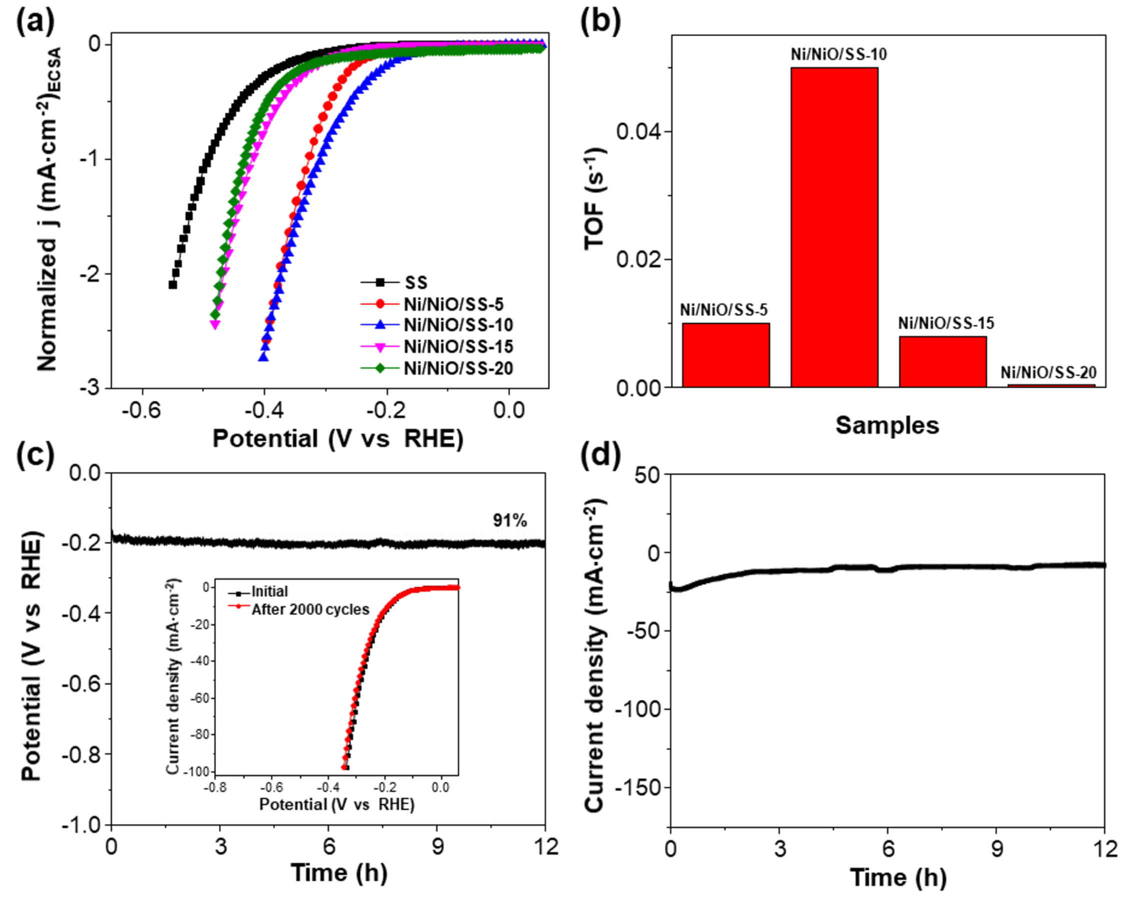

Figure 7: (a) LSV curves (normalized to the ECSA) of SS, Ni/NiO/SS-5, Ni/NiO/SS-10, Ni/NiO/SS-15, and Ni/NiO/SS-20 electrodes. (b) TOFs of Ni/NiO/SS-5, Ni/NiO/SS-10, Ni/NiO/SS-15, and Ni/NiO/SS-20 electrodes at an overpotential of 200 mV. (c) Potential–time response of the Ni/NiO/SS-10 electrode measured over a period of 12 h. Inset: Polarization curves recorded initially and after 2000 CV cycles of the Ni/NiO/SS-10 electrode. (d) Chronoamperometric curve of Ni/NiO/SS-10 electrode recorded for 12 h.

after the stability test (Supporting Information File 1, Figure S5). It is noted that there is no significant change in the morphological structure and elemental distribution of Ni/NiO/SS-10. However, EDX exhibits a slight increase in the weight fraction of oxygen. A possible explanation for this might be that OH^- ions are adsorbed by NiO species [57]. Another possible explanation is that air oxidizes the electrode after chronoamperometry [36].

Conclusion

Ni/NiO/SS self-standing electrodes were successfully prepared through a facile magnetron sputtering technique and were used as high-efficiency cathodes for the HER. By controlling the O_2 flow rate of 10 sccm in the reactor, the HER performance of the Ni/NiO/SS-10 electrode was optimized to a low overpotential of 184 mV at a current density of 10 $mA·cm^{-2}$ and a moderate Tafel slope of 90.5 $mV·dec^{-1}$. Also, remarkable stability was recorded after 12 h continuous hydrogen production by chronopotentiometry and chronoamperometry, and 2000 cycles of CV. This performance was ascribed to the collaborative work of the NiO phases, metallic Ni, and high conductivity of SS, which is advantageous for the Volmer step in alkaline solution, the combination of adsorbed H atoms, and electron transport in the catalytic process. These conclusions guide the fabrication of binder-free, robust, affordable electrocatalysts using magnetron sputtering for basic HER.

Experimental

Chemicals and materials

Nickel target (99.95%), Ar gas (99.9995%), and O_2 gas (99.9995%) were provided by Nippon Sanso company. KOH (99.95%) was provided by Sigma-Aldrich. Deionized water (DI) was created on a Millipore Milli-Q apparatus. Commercial 304 SS with a thickness of 1 mm was used as a substrate for catalyst growth.

Fabrication of the Ni/NiO/SS samples

Grade 304 SS was cut into pieces of 60 mm × 25 mm, washed with soap, and then sonicated in a mixture of acetone and ethanol to remove the impurities left on the SS template. After that, thin films of Ni/NiO were deposited on the SS substrate through reactive RF magnetron sputtering with various O_2 flow rates. In particular, the Ni/NiO nanolayers were deposited using a pure Ni target at a deposition pressure of 5×10^{-3} Torr, sputtering power of 70 W, and substrate temperature of 250 °C. In this process, the Ar flow rate was kept at 80 sccm, whereas the O_2 flow rates were to 0, 5, 10, 15, and 20 sccm to create various electrodes, designated Ni/SS, Ni/NiO/SS-5, Ni/NiO/SS-10 Ni/NiO/SS-15, and Ni/NiO/SS-20, respectively. The obtained products were stored under vacuum for further analysis.

Materials characterization

The crystal structure of materials was confirmed by XRD using Cu Kα radiation with a wavelength of 0.154 nm on a X-ray diffractometer (D8 Advance, Bruker). The morphology of the obtained products was analyzed utilizing SEM on an S-4800 Hitachi. Chemical components and element distribution in materials were studied using EDX. The Raman spectra were studied using a LabRAM-HR Evolution Raman microscope with a laser wavelength of 532 nm. The composition of the thin films was investigated using XPS on a Thermo Scientific K-Alpha XPS system.

Electrochemical measurements

The HER catalytic activities were assessed on an electrochemical workstation (VMP-3e Multichannel Potentiostat, Biologic) in a three-electrode system. A Hg/HgO electrode was used as a reference electrode, while a carbon rod was utilized as the auxiliary electrode. The self-standing Ni/NiO on the SS substrate as a working electrode was cut into pieces of 1 cm × 0.5 cm and a catalyst loading area of 0.5 cm × 0.5 cm. LSV was carried out at a scan rate of $2\ \text{mV}\cdot\text{s}^{-1}$, followed by 85% *iR* compensation, in a solution of 1.0 M KOH. EIS was investigated at a potential of −200 mV vs a reversible hydrogen electrode (RHE) in a frequency zone from 10^5 to 0.1 Hz. C_{dl} values of the samples were obtained by using CV in the non-faradaic potential range at different scan rates. The Nernst equation was used to convert the measured potential relative to Hg/HgO into RHE potential: $E_{\text{RHE}} = E_{\text{Hg/HgO}} + 0.098 + 0.059\text{pH}$.

Supporting Information

Supporting Information File 1

XRD and HER performance of Ni/SS; EDX spectra of various Ni/NiO/SS electrodes; CV curves in non-faradaic zone of electrodes at various scan rates (20–120 $\text{mV}\cdot\text{s}^{-1}$) in 1.0 M KOH.
[https://www.beilstein-journals.org/bjnano/content/supplementary/2190-4286-16-63-S1.pdf]

Conflict of Interest

The authors have no conflicts to disclose.

Author Contributions

Ha Huu Do: formal analysis; investigation; writing – review & editing. Khac Binh Nguyen: data curation; investigation. Phuong N. Nguyen: formal analysis; investigation; writing – original draft. Hoai Phuong Pham: methodology; supervision; writing – original draft.

ORCID® iDs

Hoai Phuong Pham - https://orcid.org/0000-0002-8475-0225

Data Availability Statement

Data generated and analyzed during this study is available from the corresponding author upon reasonable request.

References

1. Fan, X.; Rabelo, M.; Hu, Y.; Khokhar, M. Q.; Kim, Y.; Yi, J. *Trans. Electr. Electron. Mater.* **2023,** *24,* 123–131. doi:10.1007/s42341-022-00427-3
2. Li, X.; Han, S.; Qiao, Z.; Zeng, X.; Cao, D.; Chen, J. *Chem. Eng. J.* **2023,** *453,* 139803. doi:10.1016/j.cej.2022.139803
3. Ma, H.; Yan, W.; Yu, Y.; Deng, L.; Hong, Z.; Song, L.; Li, L. *Nanoscale* **2023,** *15,* 1357–1364. doi:10.1039/d2nr05964a
4. Ding, X.; Yu, J.; Huang, W.; Chen, D.; Lin, W.; Xie, Z. *Chem. Eng. J.* **2023,** *451,* 138550. doi:10.1016/j.cej.2022.138550
5. Sutar, P.; Deshmukh, P.; Jadhav, A.; Kadam, A. V. *Sustainable Energy Fuels* **2025,** *9,* 1073–1083. doi:10.1039/d4se01436g
6. Sapakal, S. N.; Singh, A.; Khan, A.; Gaikwad, M.; Kim, J. H.; Kadam, A. *Catal. Sci. Technol.* **2024,** *14,* 6934–6946. doi:10.1039/d4cy00779d
7. Pol, A.; Khan, A.; Sapakal, S.; Sutar, P.; Mali, S. S.; Hong, C. K.; Kadam, A. *Mol. Catal.* **2025,** *576,* 114929. doi:10.1016/j.mcat.2025.114929
8. Huang, L.; Wei, G.; Wang, J.; Li, D.; Jia, S.; Wu, S.; Jiang, T.; Guo, Y.; Liu, Y.; Ren, F. *Adv. Energy Mater.* **2023,** *13,* 2300651. doi:10.1002/aenm.202300651
9. Yin, H.; Rong, F.; Xie, Y. *Int. J. Hydrogen Energy* **2024,** *52,* 350–375. doi:10.1016/j.ijhydene.2023.08.333
10. Zhang, J.; Ma, C.; Jia, S.; Gu, Y.; Sun, D.; Tang, Y.; Sun, H. *Adv. Energy Mater.* **2023,** *13,* 2302436. doi:10.1002/aenm.202302436
11. Khamgaonkar, S.; Okasha, M.; Maheshwari, V. *Inorg. Chem. Front.* **2023,** *10,* 6812–6848. doi:10.1039/d3qi01656k
12. An, X.; Yao, T.-t.; Liu, Y.; Long, G.; Wang, A.; Feng, Z.; Dupuis, M.; Li, C. *J. Phys. Chem. Lett.* **2023,** *14,* 8121–8128. doi:10.1021/acs.jpclett.3c02142
13. Ma, W.; Zhang, X.; Li, W.; Jiao, M.; Zhang, L.; Ma, R.; Zhou, Z. *Nanoscale* **2023,** *15,* 11759–11776. doi:10.1039/d3nr01940c
14. Sun, L.; Xu, H.; Cheng, Z.; Zheng, D.; Zhou, Q.; Yang, S.; Lin, J. *Chem. Eng. J.* **2022,** *443,* 136348. doi:10.1016/j.cej.2022.136348
15. Shen, S.; Wang, Z.; Lin, Z.; Song, K.; Zhang, Q.; Meng, F.; Gu, L.; Zhong, W. *Adv. Mater. (Weinheim, Ger.)* **2022,** *34,* 2110631. doi:10.1002/adma.202110631
16. Yuan, W.; Li, Y.; Liang, L.; Wang, F.; Liu, H. *ACS Appl. Energy Mater.* **2022,** *5,* 5036–5043. doi:10.1021/acsaem.2c00396

17. Oshchepkov, A. G.; Bonnefont, A.; Saveleva, V. A.; Papaefthimiou, V.; Zafeiratos, S.; Pronkin, S. N.; Parmon, V. N.; Savinova, E. R. *Top. Catal.* **2016,** *59,* 1319–1331. doi:10.1007/s11244-016-0657-0
18. Yan, X.; Tian, L.; Chen, X. *J. Power Sources* **2015,** *300,* 336–343. doi:10.1016/j.jpowsour.2015.09.089
19. Wang, J.; Mao, S.; Liu, Z.; Wei, Z.; Wang, H.; Chen, Y.; Wang, Y. *ACS Appl. Mater. Interfaces* **2017,** *9,* 7139–7147. doi:10.1021/acsami.6b15377
20. Liang, J.; Liu, Q.; Li, T.; Luo, Y.; Lu, S.; Shi, X.; Zhang, F.; Asiri, A. M.; Sun, X. *Green Chem.* **2021,** *23,* 2834–2867. doi:10.1039/d0gc03994b
21. Suhail, H. S.; Abdulridha, A. R. *Trans. Electr. Electron. Mater.* **2024,** *25,* 1–14. doi:10.1007/s42341-023-00490-4
22. Suhail, H. S.; Abdulridha, A. R. *Trans. Electr. Electron. Mater.* **2023,** *24,* 205–216. doi:10.1007/s42341-023-00436-w
23. Ma, Y.; Li, L.; Qian, J.; Qu, W.; Luo, R.; Wu, F.; Chen, R. *Energy Storage Mater.* **2021,** *39,* 203–224. doi:10.1016/j.ensm.2021.04.012
24. Wang, T.; Liu, Q.; Li, T.; Lu, S.; Chen, G.; Shi, X.; Asiri, A. M.; Luo, Y.; Ma, D.; Sun, X. *J. Mater. Chem. A* **2021,** *9,* 884–888. doi:10.1039/d0ta11231c
25. Kuo, D.-H.; Abdullah, H.; Gultom, N. S.; Hu, J.-Y. *ACS Appl. Mater. Interfaces* **2020,** *12,* 35011–35021. doi:10.1021/acsami.0c09358
26. Ren, Z.; Jin, L.; Deng, L.; Ming, R.; Zhang, A.; Zhou, X.; Chai, B.; Zhu, Y. *Sustainable Energy Fuels* **2019,** *3,* 2321–2328. doi:10.1039/c9se00250b
27. Pol, A.; Sapakal, S.; Khan, A.; Kadam, A. V. *Surf. Interfaces* **2023,** *37,* 102706. doi:10.1016/j.surfin.2023.102706
28. Schäfer, H.; Sadaf, S.; Walder, L.; Kuepper, K.; Dinklage, S.; Wollschläger, J.; Schneider, L.; Steinhart, M.; Hardege, J.; Daum, D. *Energy Environ. Sci.* **2015,** *8,* 2685–2697. doi:10.1039/c5ee01601k
29. Yu, F.; Li, F.; Sun, L. *Int. J. Hydrogen Energy* **2016,** *41,* 5230–5233. doi:10.1016/j.ijhydene.2016.01.108
30. Huang, X.; Chang, S.; Lee, W. S. V.; Ding, J.; Xue, J. M. *J. Mater. Chem. A* **2017,** *5,* 18176–18182. doi:10.1039/c7ta03023a
31. Wang, Y.; Williamson, N.; Dawson, R.; Bimbo, N. *J. Appl. Electrochem.* **2023,** *53,* 877–892. doi:10.1007/s10800-022-01817-4
32. Barauskienė, I.; Laukaitis, G.; Valatka, E. *J. Electroanal. Chem.* **2023,** *950,* 117880. doi:10.1016/j.jelechem.2023.117880
33. Liu, Y.; Zhang, K.; Zhang, D.; Dong, W.; Jiang, T.; Zhou, H.; Li, L.; Mao, B. *J. Energy Storage* **2021,** *41,* 102844. doi:10.1016/j.est.2021.102844
34. Yan, H.; Zhang, D.; Xu, J.; Lu, Y.; Liu, Y.; Qiu, K.; Zhang, Y.; Luo, Y. *Nanoscale Res. Lett.* **2014,** *9,* 424. doi:10.1186/1556-276x-9-424
35. Wang, J.; Zhao, Z.; Shen, C.; Liu, H.; Pang, X.; Gao, M.; Mu, J.; Cao, F.; Li, G. *Catal. Sci. Technol.* **2021,** *11,* 2480–2490. doi:10.1039/d0cy02333g
36. Faid, A. Y.; Barnett, A. O.; Seland, F.; Sunde, S. *Electrochim. Acta* **2020,** *361,* 137040. doi:10.1016/j.electacta.2020.137040
37. Salunkhe, P.; A V, M. A.; Kekuda, D. *Mater. Res. Express* **2020,** *7,* 016427. doi:10.1088/2053-1591/ab69c5
38. Huang, W.; Ding, S.; Chen, Y.; Hao, W.; Lai, X.; Peng, J.; Tu, J.; Cao, Y.; Li, X. *Sci. Rep.* **2017,** *7,* 5220. doi:10.1038/s41598-017-05528-1
39. Koushik, D.; Jošt, M.; Dučinskas, A.; Burgess, C.; Zardetto, V.; Weijtens, C.; Verheijen, M. A.; Kessels, W. M. M.; Albrecht, S.; Creatore, M. *J. Mater. Chem. C* **2019,** *7,* 12532–12543. doi:10.1039/c9tc04282b
40. Lu, S.; Hummel, M.; Gu, Z.; Gu, Y.; Cen, Z.; Wei, L.; Zhou, Y.; Zhang, C.; Yang, C. *Int. J. Hydrogen Energy* **2019,** *44,* 16144–16153. doi:10.1016/j.ijhydene.2019.04.191
41. Kuang, Y.; Feng, G.; Li, P.; Bi, Y.; Li, Y.; Sun, X. *Angew. Chem.* **2016,** *128,* 703–707. doi:10.1002/ange.201509616
42. Wang, C.; Li, Y.; Wang, X.; Tu, J. *J. Electron. Mater.* **2021,** *50,* 5072–5080. doi:10.1007/s11664-021-09053-w
43. Cheng, J.; Yang, X.; Yang, X.; Xia, R.; Xu, Y.; Sun, W.; Zhou, J. *Fuel Process. Technol.* **2022,** *229,* 107174. doi:10.1016/j.fuproc.2022.107174
44. Dhandapani, B.; Jagannathan, M.; AlSalhi, M. S.; Aljaafreh, M. J.; Prasad, S. *Colloids Surf., A* **2020,** *603,* 125194. doi:10.1016/j.colsurfa.2020.125194
45. Wu, M.-Y.; Da, P.-F.; Zhang, T.; Mao, J.; Liu, H.; Ling, T. *ACS Appl. Mater. Interfaces* **2018,** *10,* 17896–17902. doi:10.1021/acsami.8b02691
46. Laursen, A. B.; Patraju, K. R.; Whitaker, M. J.; Retuerto, M.; Sarkar, T.; Yao, N.; Ramanujachary, K. V.; Greenblatt, M.; Dismukes, G. C. *Energy Environ. Sci.* **2015,** *8,* 1027–1034. doi:10.1039/c4ee02940b
47. Li, J.; Yan, M.; Zhou, X.; Huang, Z.-Q.; Xia, Z.; Chang, C.-R.; Ma, Y.; Qu, Y. *Adv. Funct. Mater.* **2016,** *26,* 6785–6796. doi:10.1002/adfm.201601420
48. Xu, R.; Wu, R.; Shi, Y.; Zhang, J.; Zhang, B. *Nano Energy* **2016,** *24,* 103–110. doi:10.1016/j.nanoen.2016.04.006
49. Zhao, G.; Rui, K.; Dou, S. X.; Sun, W. *Adv. Funct. Mater.* **2018,** *28,* 1803291. doi:10.1002/adfm.201803291
50. Muthukutty, B.; Doan, T. C.; Yoo, H. *Environ. Res.* **2024,** *241,* 117655. doi:10.1016/j.envres.2023.117655
51. Haile, D. T.; Cobet, M.; Ulbricht, C.; Mayr, F.; Leeb, E.; Hailegnaw, B.; Yohannes, T.; Sariciftci, N. S.; Workneh, G. A. *J. Phys. Chem. C* **2024,** *128,* 5443–5452. doi:10.1021/acs.jpcc.4c00006
52. Gong, M.; Wang, D.-Y.; Chen, C.-C.; Hwang, B.-J.; Dai, H. *Nano Res.* **2016,** *9,* 28–46. doi:10.1007/s12274-015-0965-x
53. Zhang, R.; Zhu, R.; Li, Y.; Hui, Z.; Song, Y.; Cheng, Y.; Lu, J. *Nanoscale* **2020,** *12,* 23851–23858. doi:10.1039/d0nr07126a
54. Meng, X.; Ouyang, Y.; Wu, H.; Huang, H.; Wang, F.; Wang, S.; Jiang, M.; Zhang, L. Y. *J. Colloid Interface Sci.* **2021,** *586,* 200–207. doi:10.1016/j.jcis.2020.10.084
55. Xia, T.; Zhou, L.; Gu, S.; Gao, H.; Ren, X.; Li, S.; Wang, R.; Guo, H. *Mater. Des.* **2021,** *211,* 110165. doi:10.1016/j.matdes.2021.110165
56. Chen, J.; Ha, Y.; Wang, R.; Liu, Y.; Xu, H.; Shang, B.; Wu, R.; Pan, H. *Nano-Micro Lett.* **2022,** *14,* 186. doi:10.1007/s40820-022-00933-2
57. Bruno, L.; Battiato, S.; Scuderi, M.; Priolo, F.; Terrasi, A.; Mirabella, S. *Int. J. Hydrogen Energy* **2022,** *47,* 33988–33998. doi:10.1016/j.ijhydene.2022.08.005

License and Terms

The definitive version of this article is the electronic one which can be found at:
https://doi.org/10.3762/bjnano.16.63

BEILSTEIN JOURNAL OF NANOTECHNOLOGY

Functional bio-packaging enhanced with nanocellulose from rice straw and cinnamon essential oil Pickering emulsion for fruit preservation

Tuyen B. Ly[1], Duong D. T. Nguyen[2], Hieu D. Nguyen[2], Yen T. H. Nguyen[1],
Bup T. A. Bui[2], Kien A. Le[1] and Phung K. Le[*3]

Full Research Paper

Open Access

Address:
[1]Institute for Tropical Technology and Environmental Protection, Ho Chi Minh City, Vietnam, [2]Faculty of Chemical Engineering, Ho Chi Minh City University of Technology (HCMUT), VNU-HCM, Ho Chi Minh City, Vietnam and [3]CIRTECH Institute, HUTECH University, Ho Chi Minh City, Vietnam

Email:
Phung K. Le[*] - ltk.phung@hutech.edu.vn

* Corresponding author

Keywords:
cinnamon essential oil; fruit preservation; Pickering emulsion; polyvinyl alcohol

Beilstein J. Nanotechnol. **2025,** *16,* 1234–1245.
https://doi.org/10.3762/bjnano.16.91

Received: 15 February 2025
Accepted: 16 July 2025
Published: 04 August 2025

This article is part of the thematic issue "Emerging technologies and nanomaterials for sustainability".

Guest Editor: V. V. Pham

Abstract

Biopackaging materials are gaining significant attention compared to traditional synthetic polymers thanks to their biodegradable and biocompatible nature to be used in food, pharmaceutical, and cosmetic industries. The current major gaps in research regarding these biopackaging materials are their low mechanical strength and the introduction of functional additives to enhance their range of applications. In this paper, a biopackaging material is formulated using polyvinyl alcohol with glycerol as a plasticizer, rice straw-derived nanocellulose as a mechanical property enhancer and cinnamon essential oil Pickering emulsion as the main functional ingredient for strawberry preservation. With the combination of nanocellulose and Pickering emulsion, this study finds that the packaging material exhibits good heat-resistance, mechanical, and water-barrier properties. At an emulsion concentration as low as 10% (v/w) in the casting solution, high UV absorbance capacity (up to 100% UVC), high antibacterial activity (92.4% *Escherichia coli* inhibition), and good antioxidative properties (up to 43% DPPH radical scavenging) were observed. These bioactive properties and the inherent moisture barrier property of the packaging material are utilized for strawberry preservation with a significant preservation time of 21 days compared to control samples that start to grow a white fungus on day 11. This combination of biopackaging with a naturally derived functional additive is proven to be effective in preserving fruits, especially easily spoiled ones like strawberries.

Introduction

Biopackaging materials are alternative materials to traditional oil-based plastic packaging that help mitigate environmental and health concerns relating to food preservation. They are used particularly in the food, pharmaceutical, and cosmetic sectors thanks to their good mechanical properties, high biocompatibility, and biodegradability [1-3]. Polyvinyl alcohol (PVA) has been shown to provide better biodegradability compared to other polymers such as polyethylene, polyvinyl chloride, and polystyrene [4-6] due to its secondary alcohol groups being susceptible to enzymatic oxidation and its water solubility enhancing microbial access [7]. PVA also exhibits superior biocompatibility as evidenced by its high safety threshold (LD_{50} of 15–20 $g{\cdot}kg^{-1}$), low systemic absorption, absence of mutagenic effects, and established medical applications, making it a reliable choice for biopackaging without concerns of harmful degradation byproducts [8,9]. One problem is that the hydrophilic structure of PVA gives it a high water-solubility, water uptake, and worse mechanical properties [10,11]. Different filler and nanomaterials including silica [12-14], graphene [15,16], and metals [17,18] have been added to PVA to develop composite materials with superior properties.

Compared to other inorganic nanomaterials, nanocellulose (NC) has been noted to be a highly potential sustainable and bio-based filler that can be obtained from otherwise wasted agricultural byproducts like rice straw [11,19]. NC can enhance polymer matrix properties, including tensile strength, elasticity, and thermal stability, due to its high surface area, hydroxy groups forming hydrogen bonds, and excellent dispersion within the matrix [20,21]. This improvement is attributed to interaction between hydroxy groups in NC and PVA, effectively reinforcing the nanofiber structure and providing better resistance to moisture-induced degradation [22]. Studies have shown that the addition of NC can significantly enhance the mechanical properties of PVA where tensile strength has been reported to increase from around 20 MPa to well over 30 MPa [23,24]. Similarly, the water vapor permeability has also been reported to change. It generally decreases with the incorporation of nanocellulose [24], thereby preventing the drying out of the fruits to be preserved, which can greatly reduce their quality [25].

One factor to be considered with this reduced permeability is that the trapped moisture with the inherent highly nutritious components of the fruits can also inversely introduce the growth of microbials, thereby facilitating the spoiling process [26]. This pushes recent research to focus on the incorporation of bioactive ingredients to introduce antimicrobial and antioxidation properties that can offer extended shelf life [27-29]. Essential oils are great candidates and possess a variety of bioactive properties while maintaining a high biocompatibility [30]. Cinnamon essential oil (CEO) is one of the best-known essential oils with strong activity against a range of Gram positive and Gram negative bacteria thanks to the cinnamic aldehyde and eugenol content in its composition [31-33]. The effectiveness of incorporating CEO in the preservation of fruits has been demonstrated. The preservation of mangoes was extended by 7 days [34] and the color of persimmons was maintained up to 63 days in cold storage [35].

The major challenge of using CEO is its hydrophobic nature, which prevents it from blending with the biopackaging casting solution, and its volatile and unstable structure, which can lead to significant loss of efficacy over time [36]. Encapsulation strategies, like Pickering emulsions (PEs) stabilized by bio-based particles, address these challenges [37]. Nanocellulose is a promising candidate for stabilizing Pickering emulsions because of its high surface area, nanoscale dimensions, and amphiphilic nature [20]. This not only improves the dispersibility of essential oils in biopolymer matrices but also enhances the overall compatibility and performance of the biopackaging material [22]. Our previous research has demonstrated that nanocellulose can effectively encapsulate CEO into a PE with small particle sizes (<700 nm), high stability, and strong antimicrobial and enhanced DPPH inhibition properties [38].

This study represents the first attempt to integrate rice straw-derived nanocellulose both as a biopackaging reinforcing filler and as a carrier for cinnamon essential oil Pickering emulsions (PE-CEO) into a single biopackaging material. While earlier studies have focused on either nanocellulose as a reinforcement or Pickering emulsions for bioactive delivery, their combined potential in scalable solutions has not been explored. By integrating nanocellulose and essential oils, biopackaging can achieve superior mechanical strength, enhanced bioactivity, and greater environmental sustainability. This synergy paves the way for scalable, eco-friendly solutions that align with industrial demands for highly functional packaging materials. To validate its real-world applicability, the biopackaging was tested on strawberry, a nutritious fruit that is highly susceptible to microbial contamination and mold growth [39] to highlight its potential to extend shelf life and improve postharvest quality. The findings indicate that this bioactive film could serve as an effective alternative to conventional packaging, offering both sustainability and enhanced food safety [30].

Results and Discussion

Physicochemical properties

FTIR spectroscopy (Figure 1a) was used to study the PVA/glycerol biopackaging (BP), NC-reinforced BP (rBP), and PE-CEO-containing rBP (rCBP) composite films. BP exhibited characteristic peaks at 3330 cm^{-1} (O–H stretching), 2900 cm^{-1} (C–H stretching), and 1420 cm^{-1} (C–H bending), which align with the chemical structure of PVA [22,24]. When NC was added, the O–H stretching peak became broader and shifted slightly to 3315 cm^{-1}, which can be attributed to the hydrogen bonding between PVA and NC [24]. For rCBP, additional peaks appeared

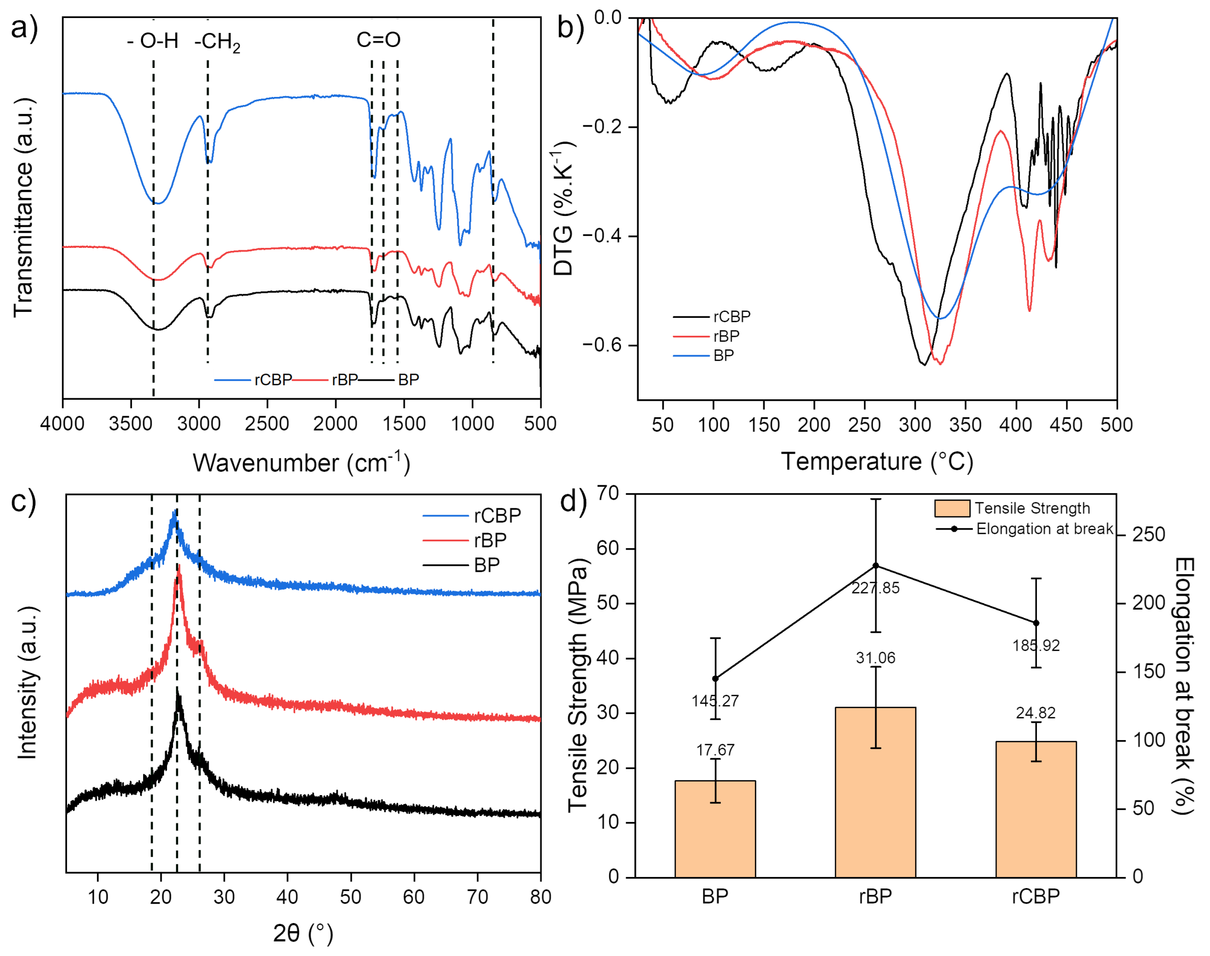

Figure 1: Effect of NC and PE-CEO on properties of biopackaging materials. (a) FTIR spectra, (b) DTG, (c) XRD, and (d) tensile strength and elongation at break.

at 1510 and 1745 cm^{-1}, corresponding, respectively, to the aromatic rings and C=O stretching of cinnamaldehyde of CEO [31]. The little difference found between rCBP and rBP suggests a low effect of CEO on the biopackaging, which can be explained either by the low concentration of CEO or the trapping effect of the polymer matrix on CEO [31].

XRD analysis (Figure 1c) shows that all biopackaging samples exhibit only large peaks at around 22° and 26°, which correspond to the (101) and (200) planes of the PVA structure [40]. It is to note that a slight peak shift to higher angles can be seen for rBP compared to BP, which indicates a decrease in interplanar spacing, suggesting that NC has infiltrated the PVA lattice structure. For rCBP, with the addition of PE-CEO that has a larger particle size (≈700 nm [38]), the peaks were shifted towards lower angles and the peak intensity was visibly lower. This may be related to the disruption of the crystalline structure of PVA after encapsulation of essential oil. For rBP and rCBP, which also contains NC, a small rise in the XRD signal can be seen at around 18°, which may be from the (110) plane of the Iβ cellulose crystalline phase [32].

Differential thermogravimetry (DTG) results (Figure 1b) revealed three distinct stages of weight loss. The first stage (30–130 °C) was attributed to water evaporation, consistent with the hydrophilic nature of PVA [41]. The second stage (260–380 °C) involved polymer chain degradation and volatile compound release [42]. At temperatures above 380 °C, carbonaceous residues decomposed. The addition of NC shifted the degradation onset temperature to a higher range, indicating improved thermal stability. This could be due to the rigid nature of NC particles, which enhance the structural integrity of the composite, delaying its decomposition [24]. CEO did not significantly alter the thermal degradation pattern, confirming that its incorporation did not compromise the thermal stability of the samples. These findings indicate that PVA-NC films are thermally suitable for applications like food packaging, where moderate temperature resistance is required.

Figure 1c illustrates the mechanical properties of biopackaging films, including tensile strength and elongation at break. The incorporation of NC significantly enhances the tensile strength of the films by more than 40%, reaching 31.06 MPa, due to the reinforcing effect of nanocellulose within the polymer matrix [41]. The presence of PE-CEO slightly decreases tensile strength and elongation at break to 24.82 MPa and 190%, respectively [43].

FTIR spectra of the biopackaging films containing different concentrations of CEO are shown in Figure 2a. The characteristic peaks confirm the presence of functional groups associated with PE-CEO and polymer interactions. The broad absorption band around 3300 cm^{-1} corresponds to O–H stretching vibrations, indicating hydrogen bonding between the biopolymer and PE-CEO components [24]. The intensity of the peaks at 1730 cm^{-1} (C=O stretching from ester or carboxyl groups) and 1600 cm^{-1} (C=C stretching of aromatic rings) changes with increasing PE-CEO concentration, suggesting interactions between PE-CEO and the polymer network [44]. These variations indicate successful incorporation of PE-CEO, which could influence the physicochemical properties of the films.

Thermogravimetric analysis (TGA) (Figure 2c) shows how increasing the PE-CEO concentration may affect the thermal stability of the sample. At lower PE-CEO concentration, almost no variation between the rCBP samples can be observed. At 10% (v/w) PE-CEO concentration, a notable decrease in mass can be observed, which is attributed to the high volatility of CEO and the fact that the high oil concentration in the biopackaging matrix makes it harder to fully load and encapsulate CEO. All biopackaging samples maintain masses of more than 50 wt % at up to 300 °C, indicating that these biopackaging are thermally suitable for applications like food packaging where moderate temperature resistance is required.

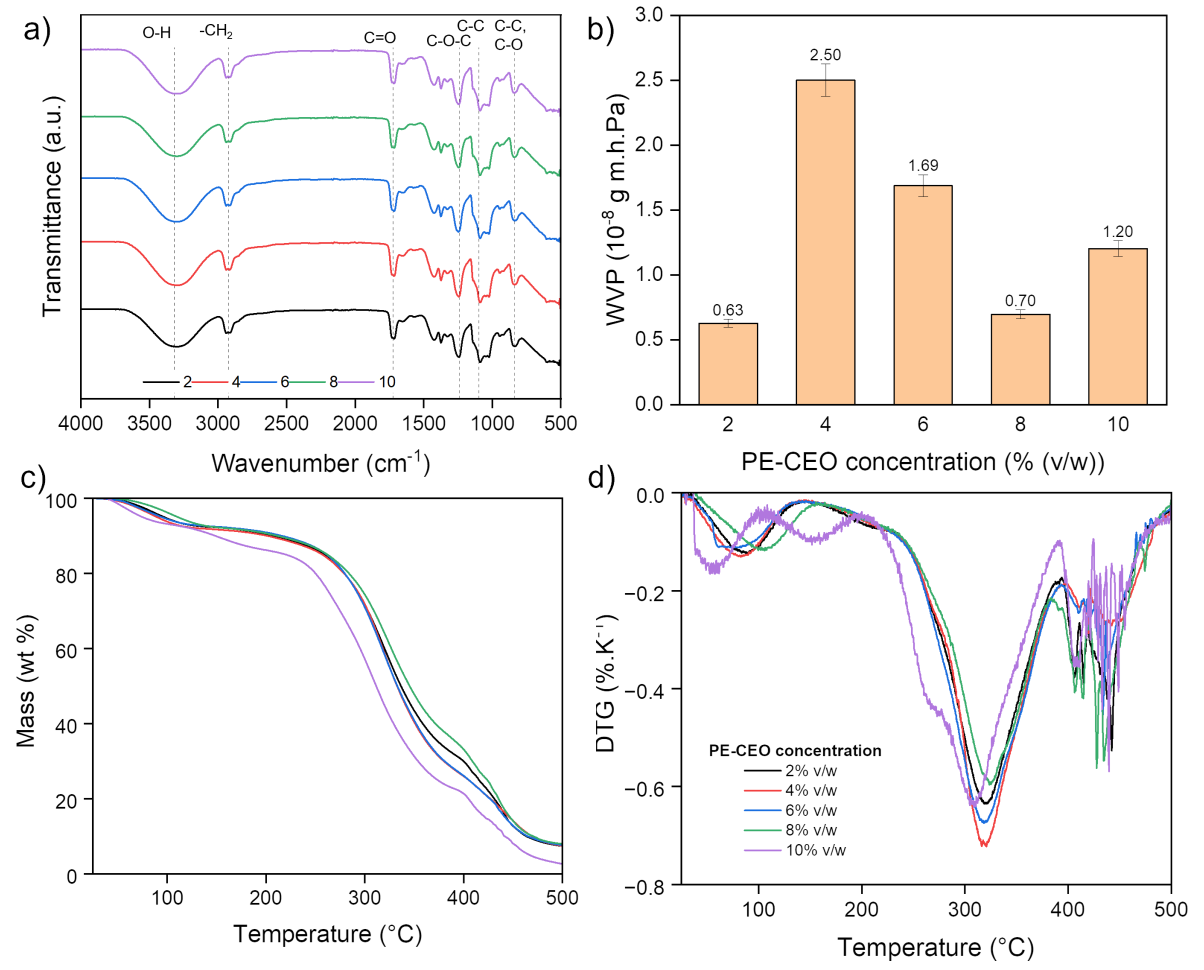

Figure 2: Effect of cinnamon essential oil Pickering emulsion concentration (2%, 4%, 6%, 8%, and 10% (v/w)) on properties of biopackaging materials. (a) FTIR spectra, (b) water vapor permeability, (c) TGA, and (d) DTG.

The effect of CEO concentration on water vapor permeability (WVP) of the biopackaging films is illustrated in Figure 2b. WVP is a critical factor for packaging applications, influencing barrier properties against moisture transmission. The results show that adding CEO reduces WVP values compared to the control. At 4% (v/w) PE-CEO, WVP decreases by approximately 23.5%, reaching 4.12×10^{-12} $g \cdot m^{-1} \cdot s^{-1} \cdot Pa^{-1}$ due to increased hydrophobicity and reduced polymer chain mobility [43]. When CEO content exceeds 8%, WVP slightly increases to 5.27×10^{-12} $g \cdot m^{-1} \cdot s^{-1} \cdot Pa^{-1}$, likely due to structural heterogeneity and phase separation within the polymer matrix [45]. These findings suggest that an optimal PE-CEO concentration exists to balance water resistance and mechanical stability, making PE-CEO-infused films promising candidates for biopackaging applications requiring controlled moisture permeability.

The surface morphology of the biopackaging materials was examined using scanning electron microscopy (SEM) (Figure 3). As shown in our previous research, nanocellulose in suspension has a size of around 20–30 nm and a length below 300 nm, and size increase due to structural collapse would be seen upon drying [24,46]. A SEM image of the nanocellulose sample is given in Figure 3a. After freeze-drying, some coagulation occurred, increasing the size of the sample to reach ≈4 µm in diameter and ≈1 µm in length.

Pure BP films (Figure 3b) exhibited a relatively smooth surface with visible small pores, indicative of weak intermolecular interactions. The incorporation of NC into the PVA matrix significantly reduced surface roughness and void formation, suggesting enhanced structural integrity due to the strong hydrogen bonding between NC and PVA (Figure 3c) [22]. The addition of CEO further modified the film structure, forming a more compact and homogenous surface, which likely contributed to improved mechanical properties and moisture resistance (Figure 3d) [31].

Bioactive properties

The DPPH radical scavenging (Figure 4a) showed a linear increase in scavenging activity with increasing CEO concentration, reaching a maximum of 43% at 10% (v/w) CEO incorporation. This trend suggests a direct correlation between the phenolic content of CEO and its ability to inhibit DPPH free radicals [47]. The antioxidative performance of the films aligns with previous studies on essential oil-infused biopolymer matrices, confirming their potential to enhance food packaging stability by preventing oxidative degradation [48].

With increasing CEO concentration, transmittance decreased significantly in the UV region (300–400 nm) (Figure 4b), demonstrating strong UV blocking capability [49]. The transmittance even dropped to near zero in the UVC range (280–315 nm). Above 400 nm, the transmittance was higher but remained below 100%, highlighting the dual function of PE-CEO in absorbing harmful UV rays while partially limiting visible light transmission (Figure 4d). This makes rCBP ideal for preserving light-sensitive products such as fruits and vegetables, protecting them from photodegradation and extending their shelf life [24]. This effect can be attributed to the presence of cinnamaldehyde and other phenolic compounds in CEO, which act as natural UV absorbers [50].

The antimicrobial properties of the biopackaging were assessed by a time-kill assay against *E. coli* and *S. aureus* after 24 h of exposure (Figure 4c,e). rBP exhibited slight inhibitions of *E. coli* and *S. aureus* (<20%): This can be due to the presence of hydroxy groups in PVA, which can disrupt hydrogen bonds and dissolve the peptidoglycan membranes of the bacteria [51]. CBP showed a drastic time-kill effect of more than 90% for both types of bacteria, attributed to the potent antibacterial functional groups in CEO (cinnamaldehyde and eugenol) [33,52].

The release of CEO from the films was studied over time (Figure 5a). The release pattern had two phases, namely, a fast initial release of 42% within the first 100 min, followed by a slower phase up to 300 min. The fast release happened because some CEO was near the surface of the film, while the slower phase was controlled by how CEO moved through the polymer.

Mass loss and appearance of the strawberry samples when covered by the biopackaging material are presented in Figure 5b,c. Strawberry is in the focus of this research since its moist and soft structure can support the growth of microorganisms, making them spoil as early as 1–2 days after harvest without any processing [39]. Several attempts have been made that could extend strawberry preservation only up to 6, 9, and 10 days, respectively, with PVA/chitosan/1,8-cineole/cyclodextrin [53], PVA with lids [54], and modified atmosphere polypropylene [55]. In this research, without any biopackaging, the strawberry would grow moldy right on day 11 and become dryer and reduced in size, which led to the fastest decrease in mass. In contrast, at no or very low concentration of CEO (up to 2% (v/w)), the time until fungal growth was extended to day 15, which is due to the bioactive properties of CEO. When increasing the CEO concentration to 6% and 10% (v/w), no fungal growth was recorded up to day 21. It is important to note that at low CEO concentrations, the biopackaging acts as a moisture barrier to prevent moisture escape from the sample, making the sample wet and foggy at day 21. At higher CEO concentrations,

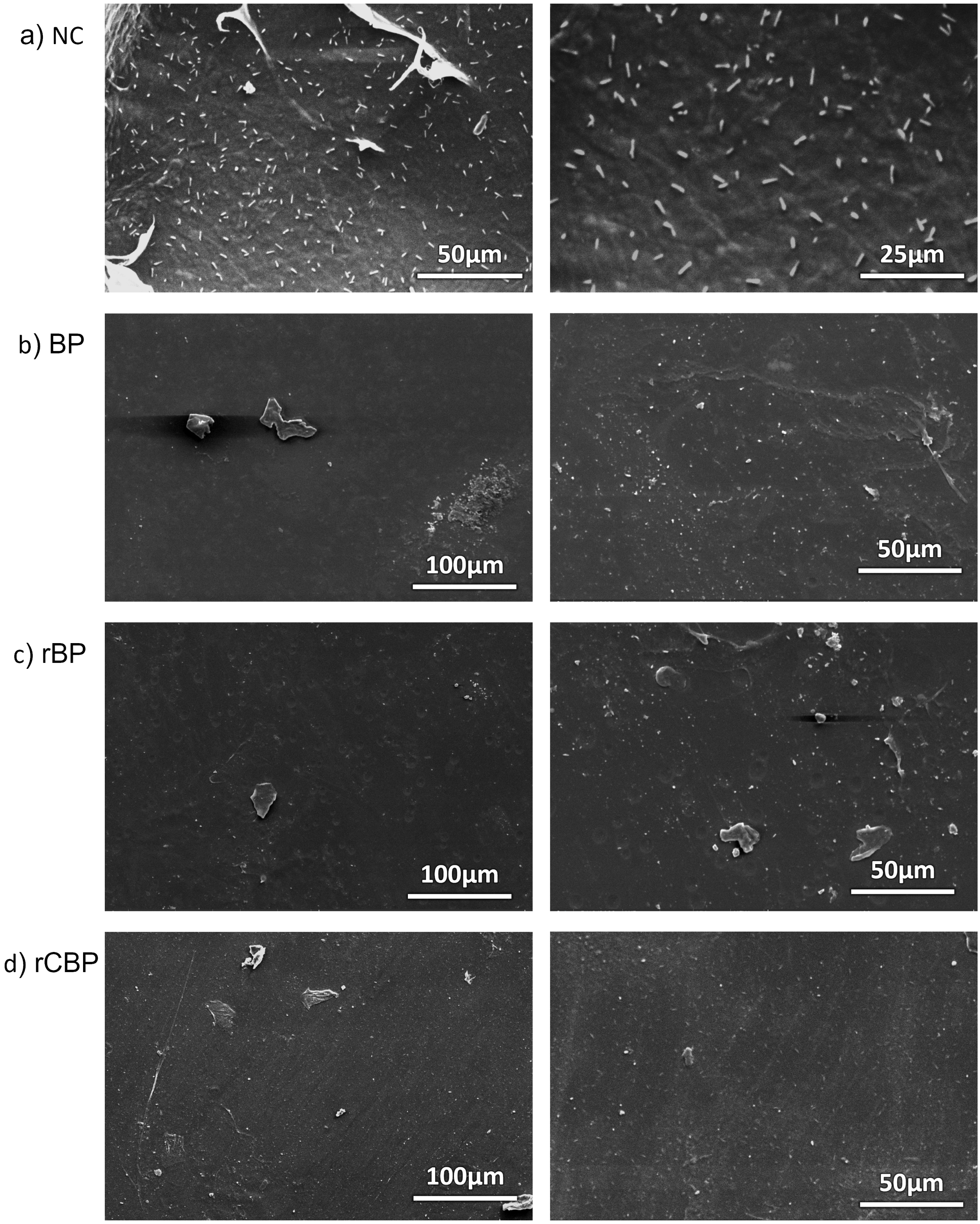

Figure 3: SEM images of the samples. (a) Nanocellulose (NC), (b) biopackaging (BP), (c) NC-reinforced biopackaging (rBP), and (d) reinforced biopackaging with PE-CEO at 6% (v/w) (rCBP).

the biopackaging enables moisture escape to further prevent the proliferation of fungi and contaminations. This led to slightly higher mass loss upon preservation in these samples. All in all, these results showed that rCBP biopackaging materials are effective in extending the strawberry preservation time up to 21 days.

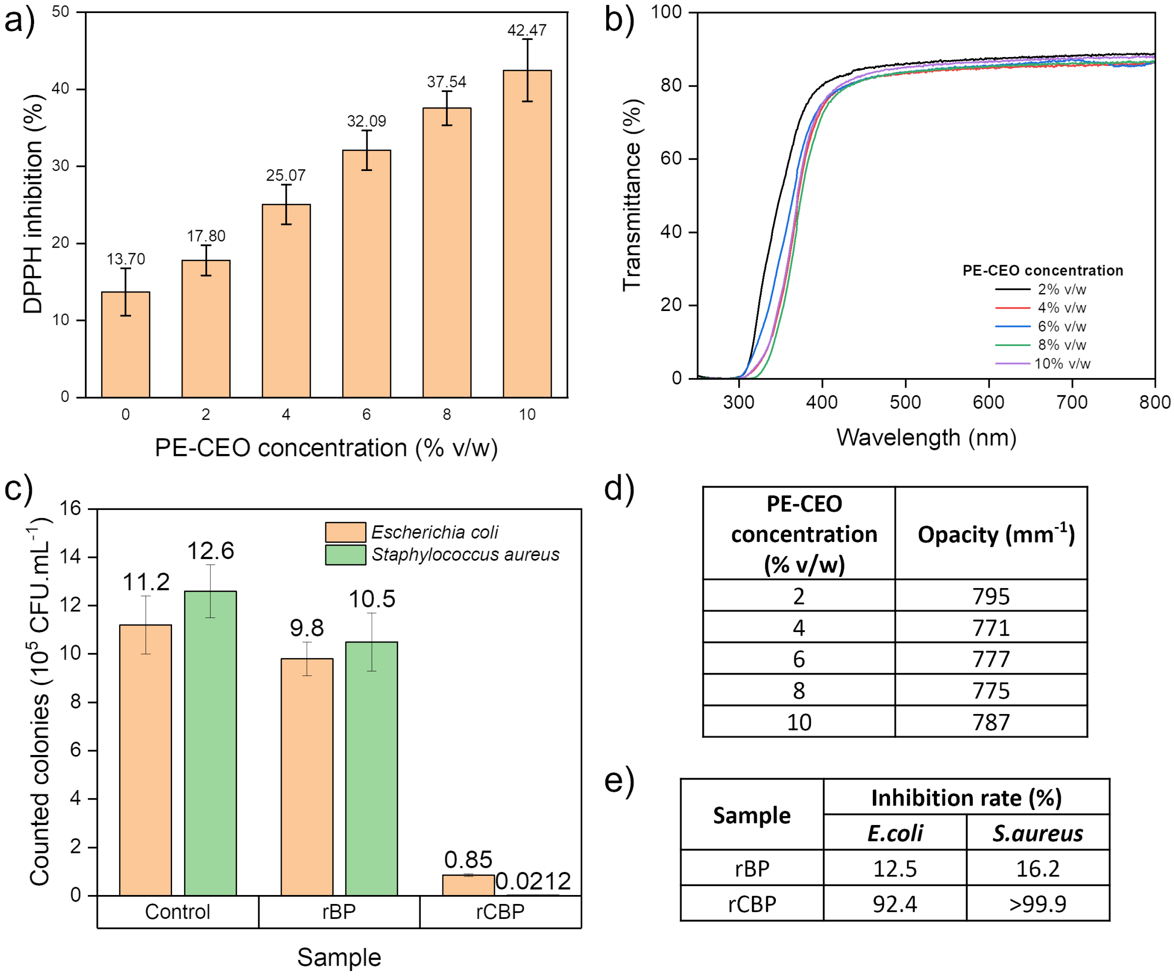

PE-CEO concentration (% v/w)	Opacity (mm^{-1})
2	795
4	771
6	777
8	775
10	787

Sample	Inhibition rate (%)	
	E.coli	***S.aureus***
rBP	12.5	16.2
rCBP	92.4	>99.9

Figure 4: Bioactive properties of the sample. (a) DPPH scavenging activity, (b) UV–vis transmittance, and (d) opacity at different PE-CEO concentrations (2%, 4%, 6%, 8%, and 10%(v/w)). (c) Counted colonies and (e) inhibition rate from time-kill analysis using rCBP samples at 10% (v/w) PE-CEO after 24 h against *E. coli* and *S. aureus*.

Conclusion

This study successfully developed an innovative biopackaging material by integrating rice straw-derived NC and cinnamon essential oil stabilized within a Pickering emulsion (PE-CEO) into a polyvinyl alcohol matrix. The incorporation of NC has been shown to enhance thermal stability, mechanical strength, and water vapor barrier property of the films, while the addition of PE-CEO imparted strong UV blocking, antimicrobial, and antioxidative properties. TGA and mechanical strength tests confirmed that NC improves the structural integrity. The controlled release of CEO helped to ensure prolonged bioactive effects, providing a dual-function material suitable for food preservation applications. The resulting films demonstrated their practical potential by extending the shelf life of strawberries to 21 days, compared to 11 days for unwrapped samples, therefore highlighting the potential of combining renewable materials and natural functional additives to create scalable, eco-friendly packaging solutions.

Experimental

Materials

Rice straw used for NC synthesis was provided by Loc Troi Group from An Giang province, Viet Nam. Cinnamon essential oil (CEO) was obtained from pure *Cinnamomum verum* bark through steam distillation by Notessen Co. Ltd. (Viet Nam) and exhibited a cinnamaldehyde content greater than 96%. All chemicals, including sulfuric acid (H_2SO_4), polyvinyl alcohol (PVA), and glycerin ($C_3H_8O_3$), were obtained from commercial sources and used as received.

Material synthesis

Nanocellulose synthesis process

Rice straw served as the source material for nanocellulose production. Following a previously established procedure [46], two alkaline pretreatment steps and a bleaching stage were used to extract cellulose from the straw. In the first acid hydrolysis step, the cellulose was treated with 62% H_2SO_4 solution at a

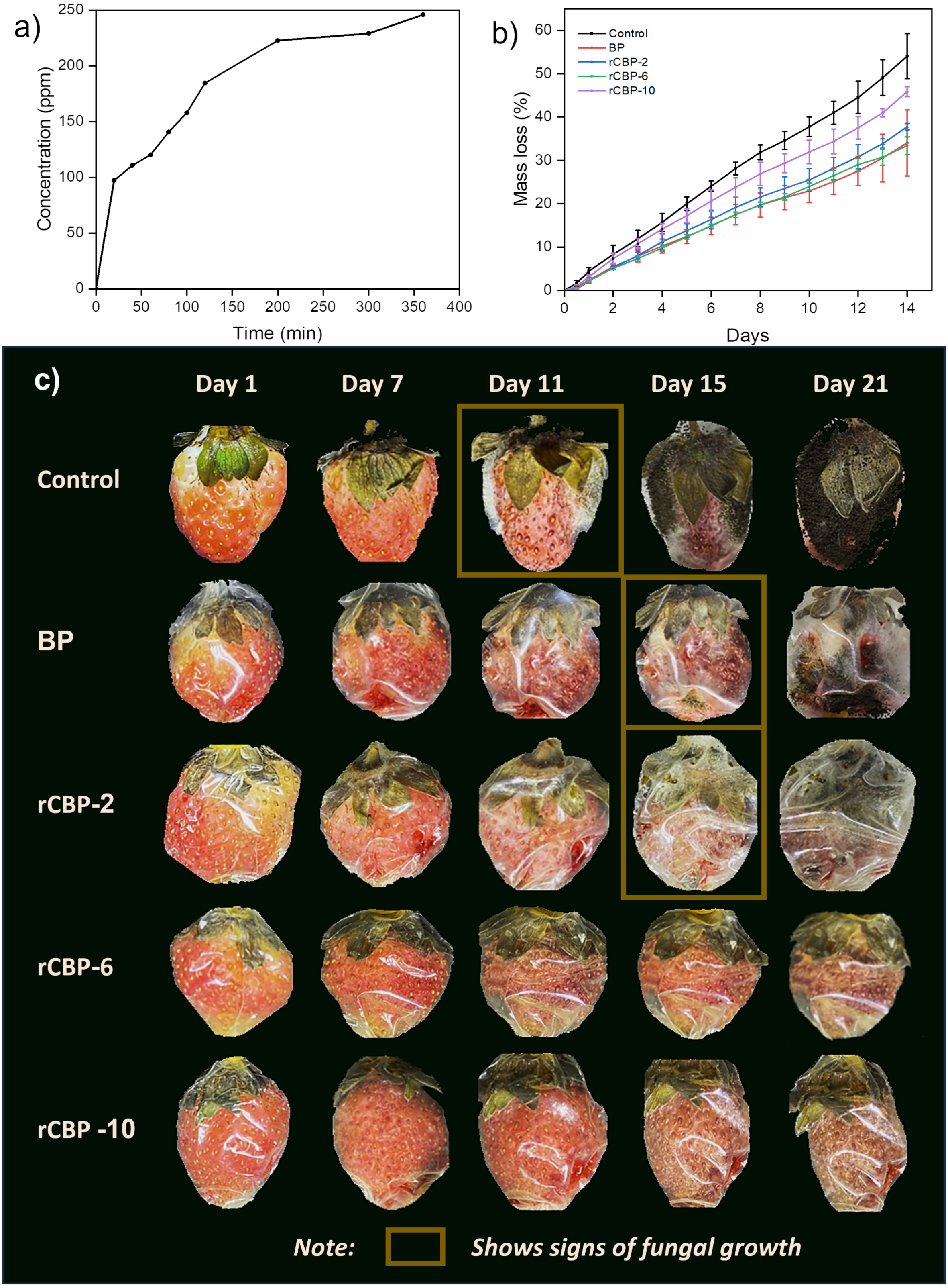

Figure 5: Results on strawberry preservation. (a) Release profile of CEO from rCBP-10, (b) mass loss record by days, and (c) appearance of the fruits after 1, 7, 11, 15, and 21 days of preservation for control (commercial PVC), BP, and reinforced biopackaging with PE-CEO (rCBP) at different concentrations (2%, 6%, and 10% (v/w)).

solid-to-liquid ratio of 1:12 ($g \cdot mL^{-1}$), continuously stirred at a temperature of 40–42 °C for 2 h. The reaction was then quenched by 10-fold dilution of the solution. The solution was washed by centrifugation three times and filtered through a 10 µm nylon mesh filter membrane. In the neutralization step, the solution was neutralized by dialysis with deionized water, which was replaced every 6 h, and sonicated using a Hielscher UP400St ultrasonic homogenizer (Germany) to create the NC suspension. Our previous research has stated that the size of the NC crystals was around 20–30 nm in width and 300 nm in length [24,46]. The NC concentration in the suspension was analyzed by dripping 3 mL of the suspension onto a pre-dried Petri dish. Subsequent drying was performed in a convection oven at 60 °C until a constant weight was achieved. The NC content was then determined by applying Equation 1:

$$\%m_{\mathrm{NC}} = (m_2 - m_0)/(m_1 - m_0), \tag{1}$$

where m_0 represents the mass of the dried petri dish, m_1 is the mass recorded after adding the suspension, and m_2 is the mass measured after the sample had dried.

Stabilization of oil-in-water Pickering emulsions using nanocellulose

The cinnamon essential oil Pickering emulsions (PE-CEO) were prepared by combining essential oil at 15% (v/v) with nanocellulose suspensions at 0.6% (w/v). The mixture of essential oil and nanocellulose suspensions was then sonicated using a Hielscher UP400St ultrasonic homogenizer (Germany). The sonication process was conducted at a power of 200 W with each cycle consisting of 2 min of sonication followed by 2 min of rest for a total of six cycles, corresponding to a total sonication time of 12 min.

Preparation of essential oil Pickering emulsion containing biopackaging

PVA was dispersed in water at 6% (w/v) using a magnetic stirrer with heating at 80 °C for 3 h and 1 mL of glycerol was added to create the biopackaging (BP) film-forming solution [24]. NC suspension at a $m_{\mathrm{NC}}/m_{\mathrm{PVA}}$ ratio of 6% (w/w) was added to form the NC-reinforced BP solution (rBP). PE-CEO was added at $m_{\mathrm{PE}}/m_{\mathrm{PVA}}$ ratios of 2%, 4%, 6%, 8%, and 10% (v/w) for the corresponding NC-reinforced PE containing biopackaging (rCPB-2, rCPB-4, rCPB-6, rCPB-8 and rCPB-10). The film solution was then sonicated in a water bath to remove any bubbles and cast onto a mold and dried at 70 °C for 12 h. All concentrations were based on the mass of PVA.

Characterization

Physicochemical properties

Fourier transform infrared spectroscopy (FTIR) spectra were recorded in the range of 4000–500 cm^{-1} using a Bruker ALPHA II spectrometer (Germany) at a spectral resolution of 4 cm^{-1}.

Thermal stability was determined using thermogravimetric analysis (TGA) and differential thermogravimetric analysis (DTG). Samples were heated from 25 to 500 °C at a rate of 10 $K \cdot min^{-1}$ under N_2 atmosphere (50 $mL \cdot min^{-1}$) in a METTLER TOLEDO 3+ Large furnace (Switzerland).

X-ray diffraction (XRD) was performed using an Aeris Minerals Edition from PANalytical (UK) with Co radiation at 40 kV. Biopackaging samples were clipped on a 16 mm holder and the measurement was performed using a 1/8° diffraction slit.

Mechanical strength was determined at room temperature using a Testometric X350 testing machine (UK) following the ASTM D882 standard. Testing was performed at a crosshead speed of 50 $mm \cdot min^{-1}$ using a 1 N load cell on 1 cm × 7 cm specimens at room temperature.

Water vapor permeability (WVP) was measured using a modified ASTM E96/E96M-16 method. 90 mm diameter biopackaging samples were wrapped around cups containing 40 mL of distilled water and sealed with plastic lids with a 50 mm diameter opening. The weight of each cup was recorded every hour for 8 h to calculate the water vapor transmission rate (WVTR) and repeated three times. The water vapor transmission rate (WVTR) was calculated based on the weight loss over time (Equation 2), and WVP was subsequently determined using (Equation 3):

$$\mathrm{WVTR} = G/(t \cdot A), \tag{2}$$

where WVTR is the water vapor transmission rate ($g \cdot h^{-1} \cdot m^{-2}$), G is the change in mass (g), t is the test duration (h), and A is the test area (m^2).

$$\mathrm{WVP} = (\mathrm{WPTR} \cdot L)/\Delta P = (\mathrm{WVTR} \cdot L)/(S(R_1 - R_2)), \tag{3}$$

where WVP is the water vapor permeability of the sample ($g \cdot m^{-1} \cdot h^{-1} \cdot Pa^{-1}$), L is the sample thickness (m), ΔP is the vapor pressure difference (Pa), S is the saturation vapor pressure at the test temperature (Pa), R_1 is the relative humidity inside the dish, and R_2 is the relative humidity at the cup.

The surface morphology of the biopackaging materials (BP, rBP, and rCBP) was observed using a scanning electron microscope (SEM), model Primas E (US). The samples were coated with Pt for 30 s prior to measurement.

Bioactive properties

UV absorption. Transparency and UV absorption of the films were determined using UV–vis spectroscopy in the wavelength range of 250–700 nm on a 754 STECH INTERNATIONAL spectrophotometer (China). Five samples (1 × 4 cm^2) were measured with transparency and UV protection assessed by measuring transmittance at 600 nm and 280 nm, respectively. The opacity of the biopackaging is calculated based on its absorbance at 600 nm and its thickness as (Equation 4).

$$\text{opacity} = \frac{\text{Ab}_{600}}{t}, \qquad (4)$$

where Ab_{600} represents the absorbance at 600 nm and t is the biopackaging thickness [49].

Antimicrobial properties. The antimicrobial activity of the films was evaluated using a time-kill method. *Escherichia coli* ATCC 25922 and *Staphylococcus aureus* ATCC 29213 were grown in tryptic soy broth and standardized to a concentration of approximately 1.5×10^8 CFU·mL^{-1} (McFarland 0.5). Prior to analysis, the test films (BP, rBP, and rCBP) were sterilized under UV light for 5 min using a 30 W UVC lamp at a distance of 15 cm. Semicircle biopackaging samples (roughly 55 cm^2, from half a Petri dish) were added to the microbial suspensions in saline water and incubated for 24 h. A control tube without the film was prepared in parallel. After 24 h of incubation at 37 °C, serial dilutions were prepared and plated on Mueller–Hinton Agar (MHA) and colony-forming units (CFU) were counted to determine the antimicrobial activity of the films. Inhibition rates were calculated according to

$$I(\%) = \frac{\text{CC}_{\text{control}} - \text{CC}_{\text{sample}}}{\text{CC}_{\text{control}}}, \qquad (5)$$

where $\text{CC}_{\text{control}}$ is the cell count of the control tube substance and $\text{CC}_{\text{sample}}$ is the cell count of the sample after 24 h.

Antioxidation properties. The antioxidant capacity of the samples was assessed using the 1,1-diphenyl-2-picrylhydrazyl (DPPH) radical scavenging assay. Exactly 1.00 g of biopackaging samples were added into 1.8 mL of 80% methanol. Afterwards, 3.2 mL of 0.1 mM DPPH solution was added to ensure that the absorbance of the control was above 0.6, and the samples were kept in the dark for 30 min. Measurements was performed using a 754 STECH INTERNATIONAL (China) UV–vis spectrophotometer at 517 nm. The DPPH radicals scavenging ability was calculated using (Equation 6):

$$I(\%) = \frac{A_{\text{control}} - \left(A_{\text{sample}} - A_{\text{color}}\right)}{A_{\text{control}}}, \qquad (6)$$

where A_{control} is the absorbance of the sample without the test substance, A_{sample} is the absorbance of the sample containing both the test substance and DPPH, and A_{color} is the absorbance of the sample containing the test substance without DPPH.

Controlled release profile. The controlled release of CEO from the films was evaluated every 20 min over 380 min by soaking exactly 1 g of film sample into 10% (v/v) ethanol solutions. The released CEO was measured by analyzing the CEO concentration in the solution through the absorbance at 290 nm using a 754 STECH INTERNATIONAL spectrophotometer following a previously established CEO standard curve [38].

Strawberry preservation

Strawberries were chosen for this study. Unripe strawberries, slightly green in color, were selected and soaked in 80% ethanol to eliminate potential microbial contamination on the outer surface before storage. The strawberries were wrapped in a layer of biopackaging and stored under the same refrigeration conditions at 10 °C. The weight of each strawberry, including its packaging, was recorded on the first day of the experiment. Daily photographs and weight measurements were taken to monitor changes in mass and appearance. The experiment was carried out for a period of 21 days, which is the final time where all strawberries were covered with a white layer of fungi.

Acknowledgements

We acknowledge the support from HUTECH University and Institute for Tropical Technology and Environmental Protection for this study.

Author Contributions

Tuyen B. Ly: conceptualization; data curation; formal analysis; methodology; visualization; writing – original draft; writing – review & editing. Duong D. T. Nguyen: conceptualization; investigation; writing – original draft. Hieu D. Nguyen: conceptualization; investigation; writing – original draft. Yen T. H. Nguyen: conceptualization; investigation; writing – original draft. Bup T. A. Bui: conceptualization; investigation; writing – original draft. Kien A. Le: funding acquisition; methodology; resources; supervision; writing – review & editing. Phung K. Le: funding acquisition; methodology; resources; supervision; writing – review & editing.

ORCID® iDs

Tuyen B. Ly - https://orcid.org/0000-0001-5655-9709
Phung K. Le - https://orcid.org/0000-0003-0570-3154

Data Availability Statement

All data that supports the findings of this study is available in the published article and/or the supporting information of this article.

References

1. Hadidi, M.; Jafarzadeh, S.; Forough, M.; Garavand, F.; Alizadeh, S.; Salehabadi, A.; Khaneghah, A. M.; Jafari, S. M. *Trends Food Sci. Technol.* **2022,** *120,* 154–173. doi:10.1016/j.tifs.2022.01.013
2. de Oliveira, W. F.; Sales Albuquerque, P. B.; Ribeiro Rodrigues, N. E.; dos Santos Silva, P. M.; Kennedy, J. F.; dos Santos Correia, M. T.; Breitenbach Barroso Coelho, L. C. *Carbohydr. Polym. Technol. Appl.* **2024,** *7,* 100407. doi:10.1016/j.carpta.2023.100407
3. Cho, C.; Kobayashi, T. *Curr. Opin. Green Sustainable Chem.* **2021,** *27,* 100413. doi:10.1016/j.cogsc.2020.100413
4. Yang, S.-S.; Wu, W.-M.; Pang, J.-W.; He, L.; Ding, M.-Q.; Li, M.-X.; Zhao, Y.-L.; Sun, H.-J.; Xing, D.-F.; Ren, N.-Q.; Yang, J.; Criddle, C. S.; Ding, J. *J. Cleaner Prod.* **2023,** *428,* 139423. doi:10.1016/j.jclepro.2023.139423
5. Peng, B.-Y.; Chen, Z.; Chen, J.; Yu, H.; Zhou, X.; Criddle, C. S.; Wu, W.-M.; Zhang, Y. *Environ. Int.* **2020,** *145,* 106106. doi:10.1016/j.envint.2020.106106
6. Dong, D.; Guo, Z.; Yang, X.; Dai, Y. *Environ. Pollut.* **2024,** *342,* 123034. doi:10.1016/j.envpol.2023.123034
7. Chandra, R. *Prog. Polym. Sci.* **1998,** *23,* 1273–1335. doi:10.1016/s0079-6700(97)00039-7
8. DeMerlis, C. C.; Schoneker, D. R. *Food Chem. Toxicol.* **2003,** *41,* 319–326. doi:10.1016/s0278-6915(02)00258-2
9. Lithner, D.; Nordensvan, I.; Dave, G. *Environ. Sci. Pollut. Res.* **2012,** *19,* 1763–1772. doi:10.1007/s11356-011-0663-5
10. Mahardika, M.; Masruchin, N.; Amelia, D.; Ilyas, R. A.; Septevani, A. A.; Syafri, E.; Hastuti, N.; Karina, M.; Khan, M. A.; Jeon, B.-H.; Sari, N. H. *RSC Adv.* **2024,** *14,* 23232–23239. doi:10.1039/d4ra04205k
11. Alvarado, M. C. *Food Bioeng.* **2024,** *3,* 189–209. doi:10.1002/fbe2.12086
12. Bisht, N.; Verma, A.; Chauhan, S.; Singh, V. K. *J. Vinyl Addit. Technol.* **2021,** *27,* 920–932. doi:10.1002/vnl.21865
13. Mukherjee, A.; Panda, S.; Jeelani, P. G.; Mossa, A.-T.; Chidambaram, R. Biodegradable polymers/silica nanocomposites: Applications in food packaging. *Nanotechnology Applications for Food Safety and Quality Monitoring;* Academic Press: London, UK, 2023; pp 395–414. doi:10.1016/b978-0-323-85791-8.00001-x
14. Lara, B. R. B.; de Andrade, P. S.; Guimarães Junior, M.; Dias, M. V.; Alcântara, L. A. P. *J. Polym. Environ.* **2021,** *29,* 2397–2408. doi:10.1007/s10924-020-02033-x
15. Zeng, L.; Zhu, Z.; Sun, D.-W. *Crit. Rev. Food Sci. Nutr.* **2022,** *62,* 3705–3722. doi:10.1080/10408398.2022.2054937
16. Kishore Mohanta, Y.; Biswas, K.; Mahanta, S.; Muthupandian, S. *Graphene-Based Nanomaterials;* CRC Press: Boca Raton, FL, USA, 2023. doi:10.1201/9781003300540
17. Gasti, T.; Hiremani, V. D.; Kesti, S. S.; Vanjeri, V. N.; Goudar, N.; Masti, S. P.; Thimmappa, S. C.; Chougale, R. B. *J. Polym. Environ.* **2021,** *29,* 3347–3363. doi:10.1007/s10924-021-02123-4
18. Gómez-Espinoza, D.; Gonzalez-Calderon, J. A.; Rivera-Vázquez, R.; Aguirre-Mancilla, C. L.; Delgado-Alvarado, E.; Herrera-May, A. L.; Pérez-Pérez, M. C. I. *Antioxidants* **2024,** *13,* 1031. doi:10.3390/antiox13091031
19. Kargarzadeh, H.; Huang, J.; Lin, N.; Ahmad, I.; Mariano, M.; Dufresne, A.; Thomas, S.; Gałęski, A. *Prog. Polym. Sci.* **2018,** *87,* 197–227. doi:10.1016/j.progpolymsci.2018.07.008
20. Phanthong, P.; Reubroycharoen, P.; Hao, X.; Xu, G.; Abudula, A.; Guan, G. *Carbon Resour. Convers.* **2018,** *1,* 32–43. doi:10.1016/j.crcon.2018.05.004
21. Dufresne, A. *Mater. Today* **2013,** *16,* 220–227. doi:10.1016/j.mattod.2013.06.004
22. Hakalahti, M.; Salminen, A.; Seppälä, J.; Tammelin, T.; Hänninen, T. *Carbohydr. Polym.* **2015,** *126,* 78–82. doi:10.1016/j.carbpol.2015.03.007
23. Khatun, M. A.; Sultana, S.; Islam, Z.; Kabir, M. S.; Hossain, M. S.; Nur, H. P.; Chowdhury, A. M. S. *Results Eng.* **2023,** *17,* 101031. doi:10.1016/j.rineng.2023.101031
24. Nguyen, Y. T. H.; Ly, T. B.; Bui, B. A. T.; Le, P. K. *Chem. Eng. Trans.* **2023,** *106,* 493–498. doi:10.3303/cet23106083
25. Long, J.; Zhang, W.; Zhao, M.; Ruan, C.-Q. *Carbohydr. Polym.* **2023,** *321,* 121267. doi:10.1016/j.carbpol.2023.121267
26. Ayala-Zavala, J. F.; Del-Toro-Sánchez, L.; Alvarez-Parrilla, E.; González-Aguilar, G. A. *J. Food Sci.* **2008,** *73,* R41–R47. doi:10.1111/j.1750-3841.2008.00705.x
27. Oun, A. A.; Shin, G. H.; Rhim, J.-W.; Kim, J. T. *Food Packag. Shelf Life* **2022,** *34,* 100991. doi:10.1016/j.fpsl.2022.100991
28. Haghighi, H.; Licciardello, F.; Fava, P.; Siesler, H. W.; Pulvirenti, A. *Food Packag. Shelf Life* **2020,** *26,* 100551. doi:10.1016/j.fpsl.2020.100551
29. Bhavaniramya, S.; Vishnupriya, S.; Al-Aboody, M. S.; Vijayakumar, R.; Baskaran, D. *Grain Oil Sci. Technol.* **2019,** *2,* 49–55. doi:10.1016/j.gaost.2019.03.001
30. Li, C.; Li, L.; Feng, Z.; Guan, L.; Lu, F.; Qin, H.-M. *Food Chem.* **2021,** *357,* 129746. doi:10.1016/j.foodchem.2021.129746
31. Mirarab Razi, S.; Motamedzadegan, A.; Shahidi, A.; Rashidinejad, A. *Food Hydrocolloids* **2018,** *82,* 268–277. doi:10.1016/j.foodhyd.2018.01.013
32. Kandhola, G.; Djioleu, A.; Rajan, K.; Labbé, N.; Sakon, J.; Carrier, D. J.; Kim, J.-W. *Bioresour. Bioprocess.* **2020,** *7,* 19. doi:10.1186/s40643-020-00302-0
33. Kaskatepe, B.; Kiymaci, M. E.; Suzuk, S.; Erdem, S. A.; Cesur, S.; Yildiz, S. *Ind. Crops Prod.* **2016,** *81,* 191–194. doi:10.1016/j.indcrop.2015.11.058
34. Pan, Q.; Zhou, C.; Yang, Z.; Wang, C.; He, Z.; Liu, Y.; Song, S.; Chen, Y.; Xie, M.; Li, P. *Int. J. Biol. Macromol.* **2023,** *235,* 123914. doi:10.1016/j.ijbiomac.2023.123914
35. Hasan, M. U.; Singh, Z.; Shah, H. M. S.; Azhar, M. R.; Afrifa-Yamoah, E.; Woodward, A. *Food Chem.* **2025,** *486,* 144660. doi:10.1016/j.foodchem.2025.144660
36. Yu, W.; Gilbert, R. G.; Fox, G. P. *Food Hydrocolloids* **2020,** *100,* 105423. doi:10.1016/j.foodhyd.2019.105423
37. Hakobyan, K.; Noble, B. B.; Xu, J. *Prog. Polym. Sci.* **2023,** *147,* 101754. doi:10.1016/j.progpolymsci.2023.101754
38. Ly, T. B.; Bui, B. T. A.; Nguyen, Y. T. H.; Le, K. A.; Tran, V. T.; Le, P. K. *Int. J. Biol. Macromol.* **2024,** *276,* 134084. doi:10.1016/j.ijbiomac.2024.134084
39. Bhat, R.; Stamminger, R. *J. Food Process Eng.* **2015,** *38,* 536–554. doi:10.1111/jfpe.12184

40. Tang, C.-M.; Tian, Y.-H.; Hsu, S.-H. *Materials* **2015,** *8,* 4895–4911. doi:10.3390/ma8084895
41. Sun, Q.; Zhao, X.; Wang, D.; Dong, J.; She, D.; Peng, P. *Carbohydr. Polym.* **2018,** *181,* 825–832. doi:10.1016/j.carbpol.2017.11.070
42. Nguyen, T. H. M.; Abueva, C.; Ho, H. V.; Lee, S.-Y.; Lee, B.-T. *Carbohydr. Polym.* **2018,** *180,* 246–255. doi:10.1016/j.carbpol.2017.10.032
43. Ma, X.; Chatterton, D. E. W. *Food Hydrocolloids* **2021,** *119,* 106853. doi:10.1016/j.foodhyd.2021.106853
44. Pilipenko, I. M.; Korzhikov-Vlakh, V. A.; Zakharova, N. V.; Urtti, A.; Tennikova, T. B. *Carbohydr. Polym.* **2020,** *248,* 116764. doi:10.1016/j.carbpol.2020.116764
45. Shi, H.; Wan, Y.; Li, O.; Zhang, X.; Xie, M.; Nie, S.; Yin, J. *Food Hydrocolloids* **2020,** *101,* 105524. doi:10.1016/j.foodhyd.2019.105524
46. Ly, T. B.; Tran, N. T. T.; Pham, C. D.; Nguyen, D. D. B.; Mai, P. T.; Le, P. K. *Bioresour. Technol. Rep.* **2024,** *25,* 101804. doi:10.1016/j.biteb.2024.101804
47. Kallel, I.; Hadrich, B.; Gargouri, B.; Chaabane, A.; Lassoued, S.; Gdoura, R.; Bayoudh, A.; Ben Messaoud, E. *Evidence-Based Complementary Altern. Med.* **2019,** 1–11. doi:10.1155/2019/6498347
48. von Borries-Medrano, E.; Jaime-Fonseca, M. R.; Aguilar-Méndez, M. A.; García-Cruz, H. I. *Food Hydrocolloids* **2018,** *83,* 485–496. doi:10.1016/j.foodhyd.2018.03.009
49. Pham, C. D.; Truong, T. M.; Ly, T. B.; Le, P. K. *Waste Biomass Valorization* **2024,** *15,* 1881–1894. doi:10.1007/s12649-023-02353-8
50. Cox, H. J.; Li, J.; Saini, P.; Paterson, J. R.; Sharples, G. J.; Badyal, J. P. S. *J. Mater. Chem. B* **2021,** *9,* 2918–2930. doi:10.1039/d0tb02379e
51. Phattarateera, S.; Sangthongdee, M.; Subsomboon, T.; Threepopnatkul, P. *Ind. Crops Prod.* **2024,** *211,* 118214. doi:10.1016/j.indcrop.2024.118214
52. Syafiq, R.; Sapuan, S. M.; Zuhri, M. R. M. *J. Mater. Res. Technol.* **2021,** *11,* 144–157. doi:10.1016/j.jmrt.2020.12.091
53. Cheng, C.; Min, T.; Luo, Y.; Zhang, Y.; Yue, J. *Food Chem.* **2023,** *418,* 135652. doi:10.1016/j.foodchem.2023.135652
54. Seglina, D.; Krasnova, I.; Strautina, S.; Kalnina, I.; Gailite, I.; Dukalska, L. *Acta Hortic.* **2013,** *981,* 665–670. doi:10.17660/actahortic.2013.981.106
55. Nielsen, T.; Leufven, A. *Food Chem.* **2008,** *107,* 1053–1063. doi:10.1016/j.foodchem.2007.09.025

License and Terms

BEILSTEIN JOURNAL OF NANOTECHNOLOGY

Enhancing the photoelectrochemical performance of BiOI-derived $BiVO_4$ films by controlled-intensity current electrodeposition

Huu Phuc Dang*[1], Khanh Quang Nguyen[2], Nguyen Thi Mai Tho[3] and Tran Le[4,5]

Full Research Paper

Open Access

Address:
[1]Faculty of Fundamental Science, Industrial University of Ho Chi Minh City, Ho Chi Minh City, Vietnam, [2]Advanced Materials and Applications Research Group (AMA), HUTECH University, 475A Dien Bien Phu Street, Binh Thanh District, Ho Chi Minh City 700000, Vietnam, [3]Faculty of Chemical Engineering, Industrial University of Ho Chi Minh City, Ho Chi Minh City, Vietnam, [4]Faculty of Physics & Engineering Physics, VNUHCM-University of Science, Ho Chi Minh City, Vietnam and [5]Vietnam National University, Ho Chi Minh City, Vietnam

Email:
Huu Phuc Dang* - danghuuphuc@iuh.edu.vn

* Corresponding author

Keywords:
BiOI; $BiVO_4$; electrodeposition; photoelectrochemical water splitting

Beilstein J. Nanotechnol. **2025,** *16,* 1289–1301.
https://doi.org/10.3762/bjnano.16.94

Received: 24 February 2025
Accepted: 18 July 2025
Published: 07 August 2025

This article is part of the thematic issue "Emerging technologies and nanomaterials for sustainability".

Guest Editor: H. Nguyen Xuan

Abstract

This study investigates the fabrication of $BiVO_4$ photoanodes using a controlled-intensity current electrodeposition method to improve their photoelectrochemical (PEC) performance. The impact of varying the deposition current density and $VO(acac)_2$ concentration was systematically analyzed to optimize the crystallinity, surface morphology, and electronic properties of the films. Subsequently, an electrochemical deposition method was developed to facilitate the uniform distribution of V_2O_5 among Bi–O–I flakes to homogeneously enhance the conversion reaction. The XRD pattern confirms the monoclinic scheelite $BiVO_4$ structure with dominant (121) and (004) peaks. FESEM imaging revealed that the different deposition conditions influenced the surface morphologies of the BiOI and $BiVO_4$ films. Photocurrent density measurements showed that $BiVO_4$(326) achieved 1.2 $mA·cm^{-2}$ at 1.23 V vs RHE, representing a significant enhancement compared to the other samples. The surface hole injection efficiency was measured to be 47%, whereas the incident photon-to-current efficiency reached a peak of 18.1% at 420 nm. The applied bias photon-to-current efficiency of $BiVO_4$(326) was also superior to that of the samples fabricated with lower current density, highlighting the benefits of the optimized electrodeposition conditions for the former.

Introduction

In the context of the increasing global energy demand, the development of renewable and sustainable energy sources has become a top priority in science and technology [1,2]. Photoelectrochemical (PEC) water-splitting systems hold significant promises for converting abundant solar energy into chemical fuels, such as hydrogen [3,4]. However, their widespread application is still limited by material challenges, including insufficient light absorption, high electron–hole recombination rates, and poor stability under operating conditions [5,6]. Among various semiconductor materials, bismuth vanadate ($BiVO_4$) has attracted considerable interest due to its strong visible light absorption, moderate bandgap (≈2.4 eV), high theoretical photocurrent density (≈7.5 mA·cm^{-2}), and chemical stability in aqueous environments [7-9]. Nevertheless, $BiVO_4$ suffers from intrinsic drawbacks such as low charge carrier mobility, limited conductivity, and rapid recombination of photogenerated charge carriers, which severely restrict its PEC performance [10-12].

Various strategies have been explored to overcome these challenges and optimize the structural, electronic, and surface properties of $BiVO_4$ [13,14]. Hydrothermal synthesis has been used to produce highly crystalline $BiVO_4$ films with large surface areas; for instance, Yun He et al. [15] reported flower-like $BiVO_4$ photoanodes achieving a photocurrent density of 0.81 mA·cm^{-2} at 1.23 V vs RHE. However, the hydrothermal method often requires high temperatures and prolonged reaction times, and offers limited control over film thickness. Alternatively, Liu et al. [16] employed RF sputtering with a single $BiVO_4$ target, but the volatility of Bi in a vacuum environment often led to an imbalanced Bi/V ratio, requiring precise regulation of oxygen partial pressure. Gong et al. [17] utilized DC co-sputtering of Bi and V targets to produce $BiVO_4$ thin films at high deposition rates; however, this method resulted in irregular grain structures and significant material defects, limiting the PEC performance improvements. Electrodeposition has emerged as a promising low-cost and scalable technique for $BiVO_4$ film fabrication, offering better control over film morphology and crystallinity under mild conditions. Kim et al. [18] reported that $BiVO_4$ films fabricated via electrodeposition achieved a maximum photocurrent density of 1.4 mA·cm^{-2} at 1.23 V vs RHE. These films exhibited a three-dimensional nanoporous structure that facilitated charge carrier transport; however, their uneven porosity and high charge recombination rates hindered their PEC performance improvement. McDonald and Choi [19] introduced a facile electrodeposition method based on *p*-benzoquinone reduction to fabricate ultrathin BiOI films, which could be thermally converted into porous $BiVO_4$ photoanodes. This approach yielded electrodes with enhanced PEC activity, achieving a photocurrent density of approximately 1.25 mA·cm^{-2} at 0.5 V vs RHE in neutral phosphate buffer under AM1.5G illumination. This study highlighted the potential of BiOI-derived $BiVO_4$ as a template-guided route for improving water oxidation performance. However, the use of a constant-potential deposition technique presents limitations in controlling the film thickness, morphology, and uniformity, which are crucial for consistent $BiVO_4$ performance after conversion. Variability in the BiOI film quality remains a significant challenge, affecting the reproducibility and optimization of the final photoanodes.

Building on these limitations, in this study, we introduce a novel controlled-intensity current electrodeposition method to precisely tailor the deposition conditions of BiOI and subsequently optimize its conversion to $BiVO_4$. By systematically adjusting the deposition current density and vanadium precursor concentration, we achieved fine control over the crystallinity, grain size, porosity, and optical properties of the resulting films. This level of tunability leads to substantial improvements in PEC performance. Our method offers a higher degree of control over both the intermediate BiOI layer and the final $BiVO_4$ structure, thereby enabling enhanced charge separation and surface reaction kinetics. Furthermore, this approach provides a deeper understanding of the relationship between the synthesis parameters and PEC activity, while presenting a scalable and reproducible route for fabricating high-performance $BiVO_4$ photoanodes.

Experimental

Material

Bismuth nitrate pentahydrate ($Bi(NO_3)_3·5H_2O$, 99.9%, Sigma-Aldrich) and vanadyl acetylacetonate ($VO(acac)_2$, 98%, Sigma-Aldrich) were used as Bi and V sources, respectively. Potassium iodide (KI, 99.5%, Sigma-Aldrich) was used for the initial deposition of BiOI. *p*-Benzoquinone ($C_6H_4O_2$, 98%, Sigma-Aldrich) was used as a redox mediator in the electrodeposition process. Nitric acid (HNO_3, 65%, Merck) and sodium hydroxide (NaOH, 99%, Sigma-Aldrich) were used to adjust the pH during deposition. Ethanol (C_2H_5OH, 99.9%, Merck) and deionized (DI) water were used for cleaning and dilution, respectively. Fluorine-doped tin oxide (FTO) glass substrates (7 Ω·sq^{-1}, Pilkington) served as the conductive support for electrodeposition.

Fabrication of $BiVO_4$ photoanodes

The $BiVO_4$ film was deposited using electrochemical deposition. A solution of 0.2962 g $Bi(NO_3)_3$ dissolved in 50 mL distilled water was ultrasonicated for 30 min. Subsequently, 400 mM KI and 5% HNO_3 were added to adjust the pH to 2. Additionally, 50 mM *p*-benzoquinone (0.2 g) was dissolved in 10 mL of ethanol via ultrasonication for 30 min and added to the solution. The FTO glass substrates were cleaned with ethanol and distilled water via sequential ultrasonication. The BiOI film was electrochemically deposited onto the FTO substrate at various current deposition intensities (14, 22, and 32 mA) using a reference electrode saturated with Ag/AgCl and platinum foil at various potentials vs Ag/AgCl. This process was adapted from the *p*-benzoquinone-based method reported by McDonald and Choi [19], in which benzoquinone serves as a redox mediator for BiOI formation. However, unlike the original study, which applied constant potential conditions, our method employs a variable current-controlled deposition strategy. This approach enables the fine-tuning of the nucleation and growth behavior of BiOI flakes, resulting in enhanced control over the thickness, grain structure, and uniformity, which are key factors that influence the subsequent $BiVO_4$ conversion and PEC performance. Then, a 0.2 M $VO(acac)_2$ solution in ethanol was coated onto the BiOI film via spin coating with two different volumes of solution (0.4 μL and 0.6 μL). The BiOI film (1 cm × 1 cm) with the $VO(acac)_2$ layer was annealed at 450 °C for 2 h. Finally, the $BiVO_4$ electrode was rinsed with 1 M NaOH to remove excess V_2O_5 from the surface, followed by rinsing with distilled water and drying at room temperature. The photoanode $BiVO_4$ was named $BiVO_4(xy)$, where x indicates the current intensity for BiOI deposition, and y denotes the vanadium precursor volume (x = 14, 22, 32; y = 4, 6).

Note on $BiVO_4$(144) sample exclusion

The $BiVO_4$(144) sample was excluded from the detailed photoelectrochemical (PEC) and comparative analyses because of its poor film uniformity and significantly lower performance metrics. Preliminary characterizations showed that the film exhibited inhomogeneous coverage and an inconsistent PEC response, which could lead to misleading interpretations when comparing the material trends. Therefore, these samples were not included in subsequent analyses to maintain the clarity and consistency of the dataset.

Characteristics of materials

X-ray diffraction (XRD, Bruker D8 Advance) and Raman spectroscopy (LabRAM Odyssey Semiconductor) were used to analyze the crystal structures of photoanodes. UV–vis absorption spectra were obtained using a Cary 60 spectrophotometer. X-ray photoelectron spectroscopy (XPS, VG ESCALAB250) was employed to determine the chemical states of each photoanode. All photoanode morphologies were examined using field-emission transmission electron microscopy (FESEM, Hitachi SU8010).

Photoelectrochemical measurements

PEC experiments were performed in a conventional three-electrode cell using an electrochemical workstation (CHI650E, CH Instruments, USA). The three electrodes included a working electrode ($BiVO_4$ photoelectrode, 1.0 × 1.0 cm^2), counter electrode (Pt plate), and reference electrode (Ag/AgCl). The electrolyte used in the photoelectrochemical measurements was 0.50 M Na_2SO_4 (pH 5.6), and the xenon lamp was 300 W (PLS-SXE 300C, 100 $mW \cdot cm^{-2}$) equipped with an AM1.5G filter to simulate solar light conditions. Linear sweep voltammetry (LSV) measurements were performed by scanning the potential from −0.6 to 1.2 V (vs Ag/AgCl), at a scan rate of 0.05 $V \cdot s^{-1}$. In the LSV test, the light source illuminated the sample from the back of the FTO glass. Under AM1.5G illumination, electrochemical impedance spectroscopy (EIS) measurements were performed at an open-circuit voltage, covering a frequency spectrum from 1 Hz to 10 kHz. Mott–Schottky curves were recorded at a frequency of 1 kHz in a dark light.

Applied bias photo to current efficiency

The applied bias photon-to-current efficiencies (ABPEs) of the different photoanodes were determined using [20]:

$$\mathrm{ABPE}(\%) = 100 \times \frac{J_\mathrm{p} \times \left(E_\mathrm{rev}^{\mathrm{o}} - E_\mathrm{app}\right)}{I_\mathrm{o}}, \qquad (1)$$

where J_p is the photocurrent density ($mA \cdot cm^{-2}$) obtained from the LSV curve, I_o is the incident light intensity of the solar simulator (100 $mW \cdot cm^{-2}$), and $E_\mathrm{rev}^{\mathrm{o}}$ is the standard reversible potential for the water-splitting reaction (1.23 V).

Incident photon-to-current conversion efficiency

From the excitation at wavelengths of 300–900 nm at 0.5 V, the incident photon-to-current conversion efficiency (IPCE) was evaluated using a chopped monochromator with a 150 W Xe lamp as the simulated light source (developed by HS Technologies, Korea).

$$\mathrm{IPCE}(\%) = \frac{J \times 1240}{\lambda \times P_\mathrm{light}} \times 100\%, \qquad (2)$$

where P_light is the power density of monochromatic light acquired at a given wavelength, and J is the photocurrent density ($mA \cdot cm^{-2}$) under illumination at a wavelength ($mW \cdot cm^{-2}$).

Results and Discussion

Structural analysis (XRD)

X-ray diffraction (XRD) measurements were conducted to investigate the crystal structures of the $BiVO_4$ photoanodes under various deposition conditions ($BiVO_4$(146), $BiVO_4$(224), $BiVO_4$(226), $BiVO_4$(324), and $BiVO_4$(326)), as shown Figure 1. The diffraction peaks of all photoanodes matched those of monoclinic $BiVO_4$ (JCPDS PDF #14-0688) and fluorine-doped tin oxide (FTO) substrate (JCPDS PDF #46-1088) [21-23]. The peaks at approximately 28.9°, 30.6°, 34.6°, and 35.2° were assigned to the (110), (121), (040), (200), and (002) planes of monoclinic $BiVO_4$, respectively. Notably, the (121) plane exhibited the highest intensity across all samples, which

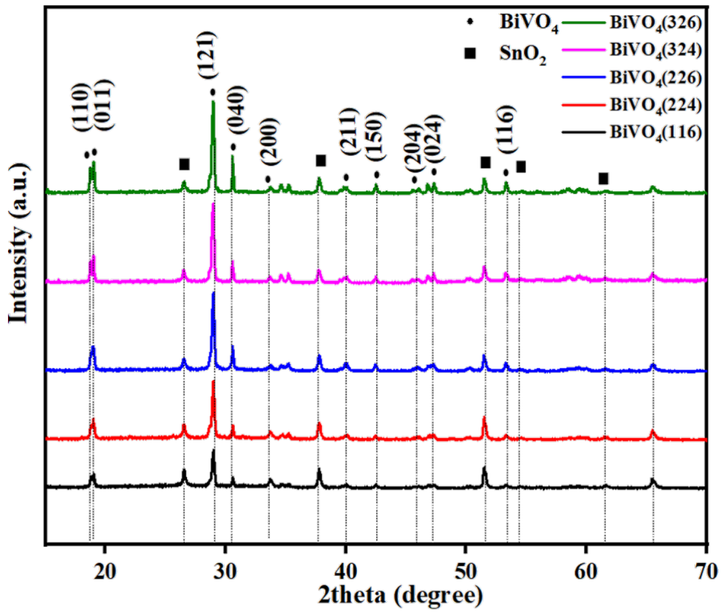

Figure 1: (a) XRD patterns of BiVO$_4$(146), BiVO$_4$(224), BiVO$_4$(226), BiVO$_4$(324), and BiVO$_4$(326) photoanodes.

aligns with its high refractive index and superior photocatalytic properties owing to the enhanced adsorption and deionization of water molecules in the structure. Additionally, the (040) peak intensity exhibited a systematic increase at higher electrodeposition current densities, suggesting preferential growth along the crystallographic direction. Higher deposition currents influence ion migration rates and nucleation kinetics, potentially leading to a preferential orientation along the (040) plane. The intensity and sharpness of the peaks increased with increasing current density and VO(acac)$_2$ concentration, indicating improved crystallinity and potentially larger grain sizes of the films. This variation in crystallographic properties is expected to influence PEC performance by affecting charge transport and surface reaction kinetics. The average crystallite size (grain size) of the BiVO$_4$ films was estimated using the Scherrer equation based on the full width at half maximum (FWHM) of the (121) diffraction peak.

The Scherrer equation to calculate average crystallite size (grain size) [24,25] is

$$D = \frac{k\lambda}{\beta\cos\theta}, \tag{3}$$

where λ is the X-ray wavelength, θ is the Bragg angle in radians, β is the full width at half maximum of the peak in radians, *D* is the particle size, and *k* is a constant with a value of 0.9.

As shown in Table 1, an increase in the deposition current and VO(acac)$_2$ concentration led to narrower peak widths and larger crystallite sizes, indicating an improved crystalline quality. BiVO$_4$(326) exhibited the largest average crystallite size (≈40 nm), consistent with the enhanced PEC per-

Table 1: Estimated crystallite sizes of BiVO$_4$ photoanodes (from the Scherrer equation).

Sample	2θ– (121) Peak	FWHM (β) (°)	Crystallite size *D* (nm)	Estimated particle size (FESEM) (nm)	Notes
BiVO$_4$(146)	28.76	0.32	25.1	≈400–500	large, irregular particles
BiVO$_4$(224)	28.82	0.29	27.6	≈300–400	rougher morphology
BiVO$_4$(226)	28.88	0.26	30.8	≈250–350	more uniform particles
BiVO$_4$ (324)	28.94	0.23	34.9	≈300–450	larger, loosely packed
BiVO$_4$(326)	28.99	0.20	40.1	≈200–300	densely packed, porous

formance and reduced lattice strain observed in the Raman analysis.

Morphological characterization (FESEM)

Field-emission scanning electron microscopy (FESEM) images highlighted the evolution of the surface morphology under different fabrication conditions. The transition from two-dimensional plate-like BiOI crystals to three-dimensional $BiVO_4$ particles was accompanied by the formation of submicrometer-scale voids, indicative of grain growth and recrystallization during the annealing process (Figure 2a,c,e). At lower current densities (e.g., $BiVO_4$(146)), the $BiVO_4$ films exhibited larger and more irregular particles with relatively low surface coverage (Figure 2b). In contrast, higher current densities (e.g., $BiVO_4$(324) and $BiVO_4$(326)) resulted in more uniform and closely packed particles, along with visible submicrometer-scale voids (Figure 2f,g). This morphology maximizes the active surface area available for photoelectrochemical reactions. Additionally, the observed submicrometer voids, which were more prominent in films deposited with larger $VO(acac)_2$ volumes, suggested improved charge separation and transport pathways. These voids facilitate the diffusion of the reactants and products, reducing the recombination rates and enhancing the water-splitting efficiency. The finer particle sizes and increased porosity, as observed for $BiVO_4$(326), align with the optical and Raman results, highlighting the impact of the optimized deposition parameters on PEC performance. The FESEM images also revealed that the films prepared at higher current densities exhibited well-defined grain boundaries, which correlated with the reduced lattice strain observed in the Raman spectra. These structural features are critical for improving the electronic and catalytic properties of $BiVO_4$ photoanodes.

To complement the XRD-derived crystallite sizes, the particle sizes were estimated from the FESEM images. As shown in Table 1, the particle size trends do not perfectly follow the crystallite size evolution. For instance, $BiVO_4$(326) exhibits the largest crystallite size (≈40 nm) but has smaller surface particle aggregates (200–300 nm) than $BiVO_4$(324). This mismatch arises because the particles observed via SEM are often composed of multiple crystalline grains. This distinction suggests that while the crystallite size governs the internal crystalline quality and carrier mobility, the particle size affects the surface area and interface kinetics. Ideally, a material such as $BiVO_4$(326) with both large crystallites and small, porous particles offers superior PEC performance owing to improved charge transport and enhanced surface reaction sites.

Optical properties (UV–vis)

UV–vis absorption spectroscopy (Figure 3) showed that $BiVO_4$ samples absorb visible light, with absorption edges between 502 and 541 nm and optical bandgaps between 2.46 and 2.30 eV (Figure 3b). Bandgap values were determined using Tauc plots for indirect allowed transitions, based on $(\alpha h\nu)^2 \propto (h\nu - E_g)$, where α is the absorption coefficient, h is Planck's constant, ν is the frequency, and E_g is the bandgap energy. The $(\alpha h\nu)^2$ values plotted against the photon energy determined E_g at the absorption edge intersection, as shown Figure 3b. Samples prepared with higher electrodeposition currents and larger $VO(acac)_2$ amounts exhibited redshifted absorption edges, indicating enhanced light harvesting due to improved crystallinity and reduced disorder. XRD and Raman spectroscopy confirmed these improvements through stronger peaks, suggesting fewer defects. The decrease in the bandgap (≈0.16 eV) is consistent with research linking oxygen vacancies to band tailing in $BiVO_4$ films [26]. Besides, Figure 3a shows that the $BiVO_4$(326) and $BiVO_4$(324) samples have absorption that goes beyond 520 nm, with some absorption still measurable up to about 650 nm. This sub-bandgap absorption occurs because of the creation of mid-gap states, mainly caused by missing oxygen atoms and structural issues that arise during high-current electrodeposition or when using higher amounts of the $VO(acac)_2$ precursor. The redshifted tails indicate that there are special energy states in the material that allow it to absorb light even at energies lower than those normally expected. The $BiVO_4$(326) sample, in particular, exhibited the most pronounced tailing, consistent with its enhanced photoelectrochemical performance. The evidence suggests an optimal concentration of oxygen vacancies that broadens light absorption while avoiding excessive recombination of the charge carriers. In contrast, $BiVO_4$(146) has a clear absorption edge and very little tailing, indicating that it has fewer defects but does not absorb light well beyond 520 nm. These findings match other studies that connect oxygen vacancies to the spread of light absorption and smaller optical bandgaps in $BiVO_4$ [26].

Vibrational properties (Raman)

The Raman spectra (Figure 4) corroborated the XRD findings, displaying characteristic peaks of monoclinic $BiVO_4$ at 219, 329, 370, 712, and 830 cm^{-1} [27]. These bands correspond to the vibrational modes associated with the VO_4^- tetrahedral structure, which directly affects the electronic properties of the material [28]. The band at 830 cm^{-1}, assigned to the symmetric stretching of the V–O bond [29], appears in samples prepared at higher current densities and larger $VO(acac)_2$ volumes. This observation suggests that improved crystallinity enhances the structural uniformity of the VO_4^- tetrahedra, leading to more efficient charge-transfer pathways. Furthermore, the appearance of sharper and more intense Raman peaks with increasing deposition parameters indicates a reduction in the structural defects and lattice strain. The vibrational modes at 329 cm^{-1} and 370 cm^{-1}, corresponding to the asymmetric and symmetric

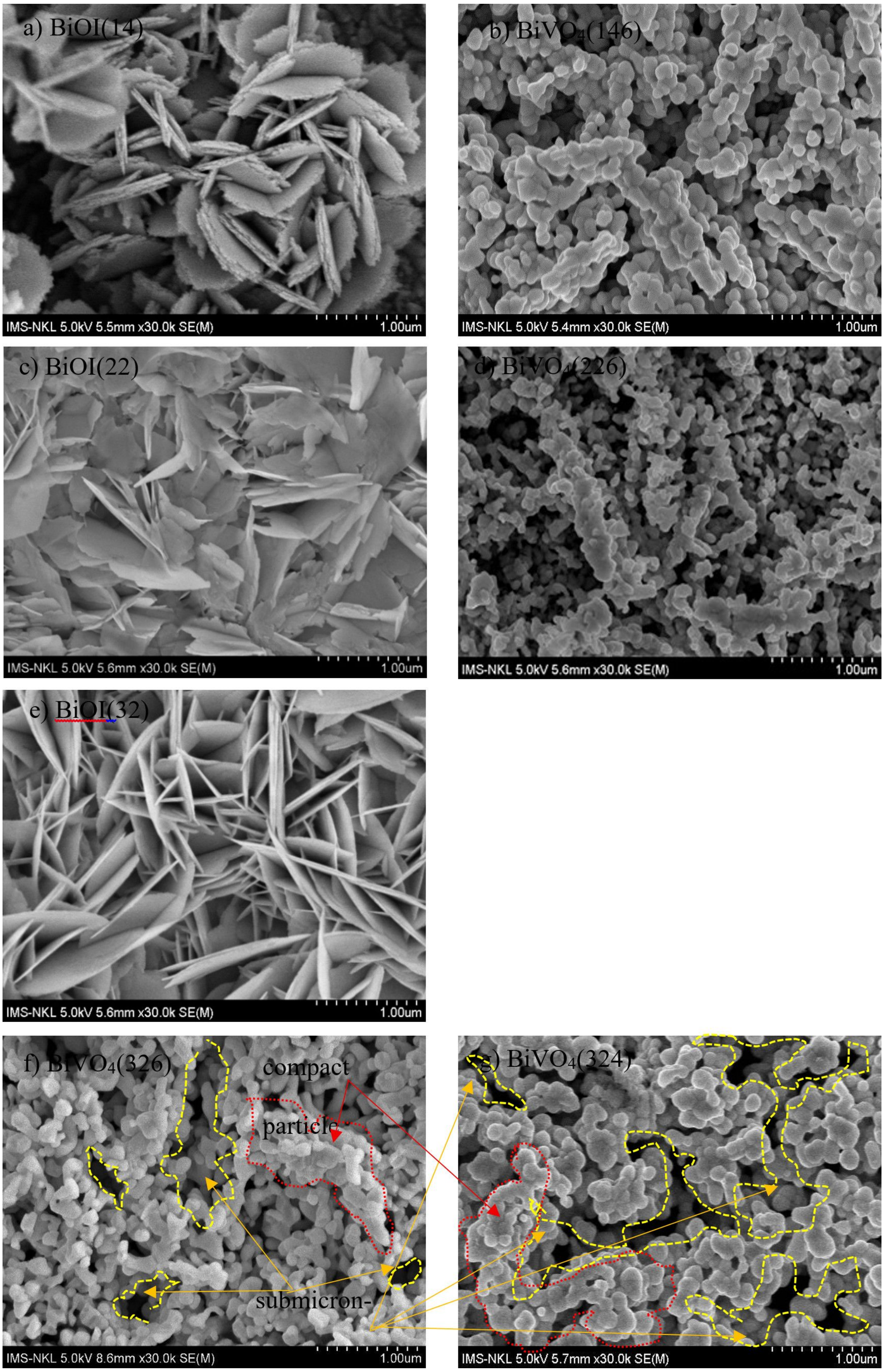

Figure 2: FESEM images of (a), (c), and (e) BiOI film under various intensities of current deposition, and (b) $BiVO_4$(146), (d) $BiVO_4$(226), (f) $BiVO_4$(326), and (g) $BiVO_4$(324) films.

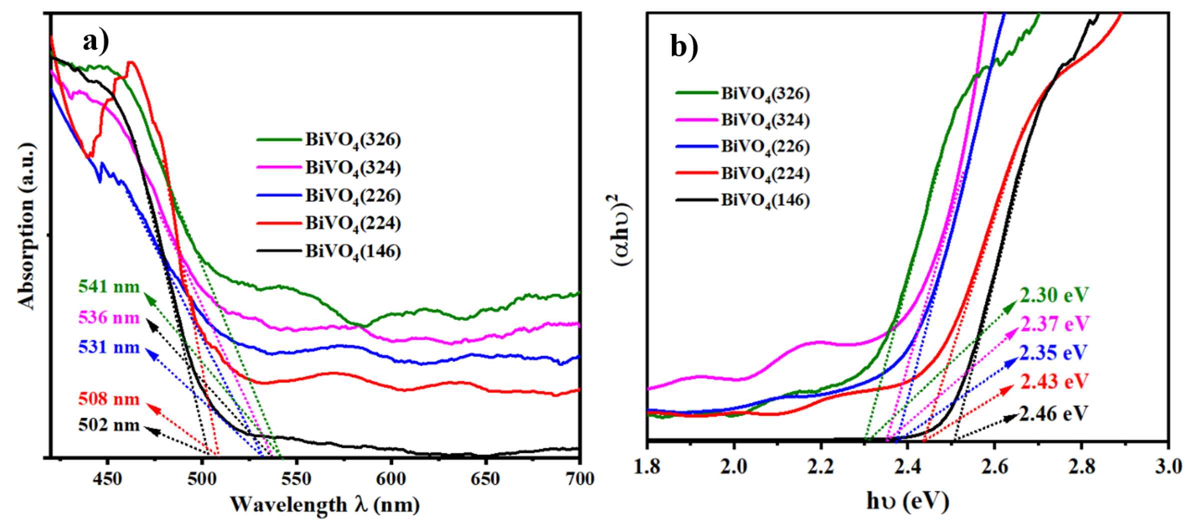

Figure 3: (a) UV–vis spectrum, (b) bandgap energies of $BiVO_4$(146), $BiVO_4$(224), $BiVO_4$(226), $BiVO_4$(324), and $BiVO_4$(326) photoanodes. Minor fluctuations above 500 nm are due to light scattering from porous films.

deformations of the V–O bond [30,31], respectively, showed a strong correlation with XRD-derived grain size variations. Larger grains typically result in fewer grain boundaries, reducing phonon scattering and enhancing vibrational coherence. Raman spectra also provide insights into the influence of fabrication conditions on surface chemistry. The relative intensities of the peaks suggest that higher deposition currents promote the formation of active crystal facets, which are critical for PEC performance. These results align with the enhanced photoelectrochemical activity observed for $BiVO_4$(326), as the improved vibrational characteristics reflect more efficient light absorption and charge separation.

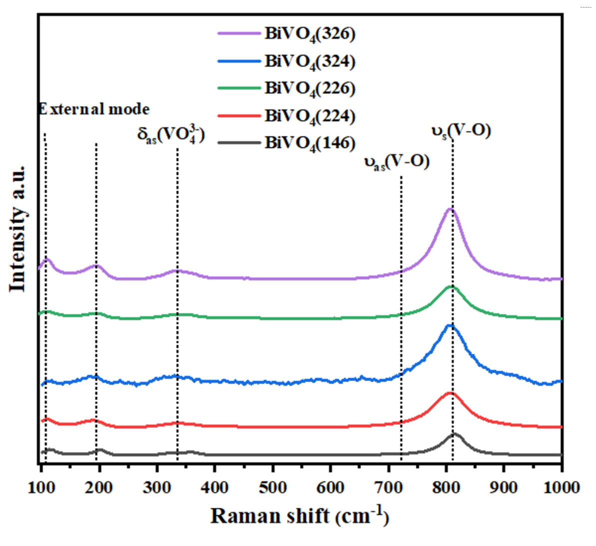

Figure 4: Raman spectrum of $BiVO_4$(146), $BiVO_4$(224), $BiVO_4$(226), $BiVO_4$(324), and $BiVO_4$(326) photoanodes.

Photoelectrochemical performance

Linear sweep voltammetry (LSV) was used to evaluate the water-splitting efficiency of the photoelectrochemical (PEC) system in a 0.50 M Na_2SO_4 solution (pH 5.6) under AM1.5G illumination (100 mW·cm^{-2}). The optimal PEC performance was achieved for the $BiVO_4$(326) sample, synthesized using a current intensity of 32 mA and $VO(acac)_2$ precursor volume of 0.6 µL. As shown in Figure 5a, this sample exhibited the highest photocurrent density of 1.2 mA·cm^{-2} at 1.23 V vs RHE, indicating efficient photoelectrochemical activity. This superior performance can be attributed to the combined effects of enhanced crystallinity, film morphology, and preferential crystal orientation. As shown in the XRD patterns (Figure 1), $BiVO_4$(326) displays the most intense (121) and (040) diffraction peaks among all the samples, suggesting preferred growth along these planes, which are known to facilitate efficient charge separation and transport. Previous studies have reported that the (121), (040), and (010) facets of monoclinic $BiVO_4$ contribute to enhanced photocatalytic activity by serving as active sites for oxidation and reduction reactions [32,33]. In particular, the large surface area of the (010) facet is associated with the effective suppression of charge recombination. Although other samples also exhibited these orientations, the relatively higher (121)/(040) intensity ratio and sharper peaks for $BiVO_4$(326) indicate improved structural ordering, which, together with its more porous and interconnected morphology (Figure 2), likely promotes better carrier mobility and PEC efficiency.

The ABPE curves (Figure 5b) demonstrate that $BiVO_4$(326) achieved the highest efficiency of 0.4% at 0.8 V vs RHE, compared to the lower efficiencies of the other samples. This

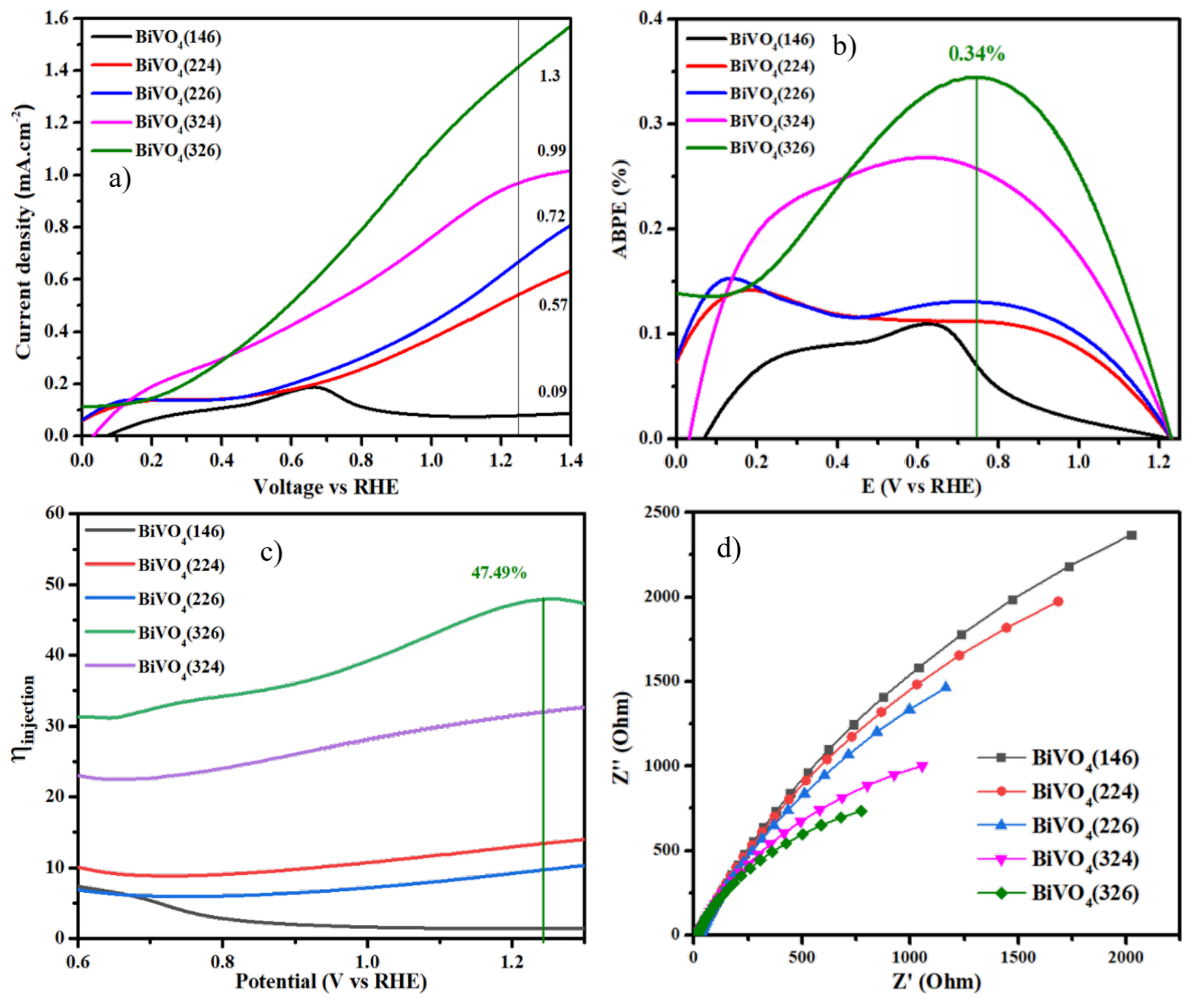

Figure 5: (a) LSV curves, (b) ABPE curves, (c) hole injection efficiency ($\eta_{surface}$) curves, and (d) EIS plots for each photoanode.

improvement is attributed to the synergistic effects of enhanced light absorption, reduced charge recombination, and increased charge transport efficiency, which are facilitated by the optimized fabrication parameters.

To investigate the influence of different chemical components on charge separation within the $BiVO_4$ bulk and surface charge transfer, LSV experiments were conducted in a 0.50 M Na_2SO_4 (pH 5.6) solution with 1 M Na_2SO_3 as a hole scavenger (Figure 5c). The hole injection efficiency was calculated as the ratio of the photocurrent density values obtained with and without the Na_2SO_3 hole scavenger. The hole injection efficiency of the $BiVO_4$(326) photoanode at 1.23 V vs RHE was 47%, which was higher than that under other conditions. This indicates that the formation of films with larger surface areas reduces the charge recombination rate and facilitates faster charge transfer rates.

AC impedance measurements were performed on the photoanodes to assess their charge transfer capabilities. As shown in Figure 5d, $BiVO_4$(326) exhibited a smaller impedance arc under illumination, indicating a minimal charge-transfer resistance. This is favorable for the rapid utilization of photogenerated holes in water oxidation reactions. Overall, these results demonstrate that the optimized $BiVO_4$(326) configuration provides improved photocatalytic activity by enhancing charge transport, reducing recombination, and maximizing the active surface area for efficient PEC water splitting.

The LSV results revealed that the photoanodes fabricated at higher current densities and larger $VO(acac)_2$ volumes (e.g., $BiVO_4$(326)) exhibited the highest photocurrent density at 1.23 V vs RHE, reaching 1.2 mA·cm^{-2}. This is nearly 4.9 times higher than that of $BiVO_4$(146). The enhanced photocurrent density correlated with the increased crystallinity, optimized grain size, and improved surface area observed in the XRD, Raman, and FESEM analyses, which collectively improved charge separation and transport. The chopped illumination data (Figure 6a) confirmed stable photoresponses with minimal decay over time, indicating the high photostability of the optimized photoanodes.

The IPCE measurements (Figure 6b) over the wavelength range of 300–500 nm showed that $BiVO_4$(326) exhibited a peak IPCE value of 18.1%, which was significantly higher than the 8.9% of $BiVO_4$(146). This increase is consistent with the improved optical absorption and structural properties, as well as the reduced electron–hole recombination rates observed in the Raman and UV–vis analyses.

The long-term photoelectrochemical stability of the optimized $BiVO_4$(326) photoanode was evaluated using chronoamperometry under continuous AM1.5G illumination at 1.23 V vs RHE in 0.50 M Na_2SO_4 electrolyte (Figure 6c). The photocurrent density initially peaked at approximately 1.6 $mA \cdot cm^{-2}$ and stabilized quickly at ≈1.2 $mA \cdot cm^{-2}$, maintaining this value consistently for 600 min (10 h) of operation. This stable behavior demonstrates the excellent PEC durability of the $BiVO_4$(326) photoanode and confirms the robustness of its structural and surface properties under prolonged operational conditions. The stability is attributed to the optimized crystallinity, reduced recombination, and uniform morphology achieved through controlled-intensity current electrodeposition.

The PEC performance of $BiVO_4$(326) was benchmarked against similar studies employing hydrothermal synthesis, direct electrodeposition, and BiOI-derived conversion methods. As summarized in Table 2, our sample achieved a photocurrent density

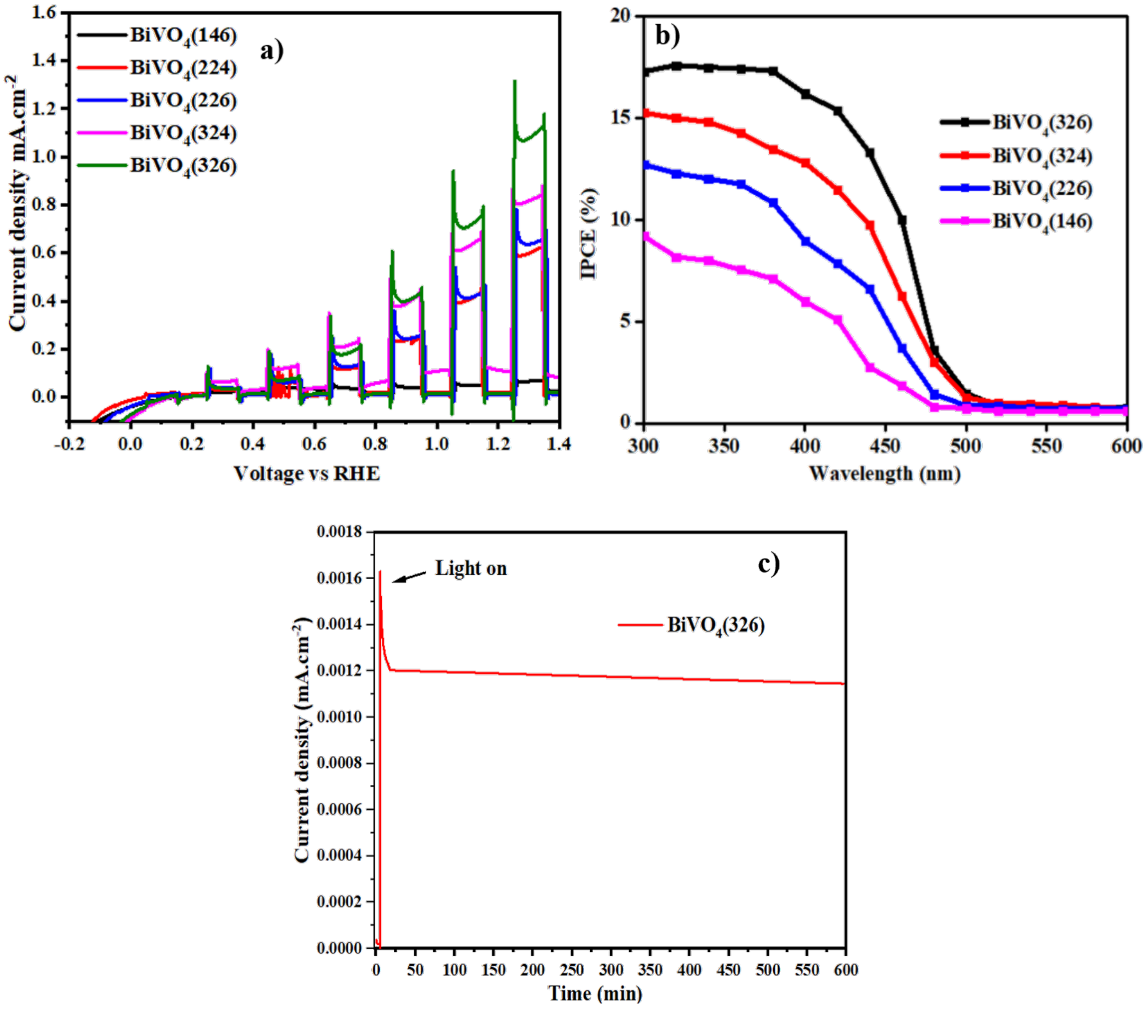

Figure 6: (a) LSV curves under chopped illumination, (b) IPCE curves for each photoanode, and (c) chronoamperometry curve of $BiVO_4$(326) measured at 1.23 V vs RHE under continuous AM1.5G illumination in 0.50 M Na_2SO_4 for 600 min.

Table 2: Summary of recent single-layer $BiVO_4$ photoanodes and their PEC performance.

Study	Method	Photocurrent density (mA/cm^2)	Stability (duration)	Notes	Ref
McDonald and Choi, (2012)	BiOI-derived $BiVO_4$ (simple electrodeposition)	≈1.25 @ 0.5 V	not reported	BiOI precursor, no stability test	[19]
Kim et al. (2014)	electrodeposition of $BiVO_4$	≈1.4 @ 1.23 V	not reported	nanoporous $BiVO_4$	[18]
Yun He et al. (2017)	hydrothermal $BiVO_4$	≈0.81 @ 1.23 V	few minutes	flower-like $BiVO_4$, high recombination	[15]
Mohamed et al. (2021)	electrodeposition (needle-like nanoflower)	≈0.32	not reported	petal-like morphology, 7 min ED time	[21]
Fuentes-Camargo et al. (2020)	pulse plating of Bi, then conversion to $BiVO_4$	≈0.35	stable and reusable	focused on pollutant degradation under Xe lamp	[34]
Pelissari et al. (2021)	SILAR (5 cycles), annealed	1.95	not reported	highly optimized multilayer thin film	[29]
Qiuhang Lu et al. (2022)	RF magnetron sputtering ($BiVO_4$ target)	≈2.1	not reported	precise thickness control, but lower crystallinity	[35]
this work	controlled-intensity BiOI → $BiVO_4$ (electrodeposition)	1.2	600 min stable	tuned crystallinity, porosity, and facet orientation	

of 1.2 mA·cm^{-2} at 1.23 V vs RHE, which is comparable to or better than the values reported for other $BiVO_4$-based photoanodes. Notably, this performance was achieved under mild synthesis conditions and was supported by excellent long-term stability (600 min), which many previous reports do not provide. The enhanced performance in our study can be attributed to the optimized grain structure, controlled crystallinity, and superior film uniformity achieved via the controlled-intensity current electrodeposition of BiOI.

Surface chemical composition (XPS)

X-ray photoelectron spectroscopy (XPS) was employed to investigate the surface chemical states and composition of the $BiVO_4$ photoanodes, focusing on the optimized $BiVO_4$(326) sample. The survey spectrum (Figure 7a) confirmed the presence of Bi, V, and O, which is consistent with the $BiVO_4$ structure. High-resolution Bi 4f spectra (Figure 7b) show a characteristic doublet at binding energies of 159.0 eV (Bi $4f_{7/2}$) and 164.2 eV (Bi $4f_{5/2}$), corresponding to Bi^{3+} in the monoclinic phase of $BiVO_4$ [36,37]. The V 2p region (Figure 7d) exhibits peaks at 516.2 eV (V $2p_{3/2}$) and 524.1 eV (V $2p_{1/2}$), indicating the presence of V^{5+} species associated with the $VO_4{}^{3-}$ tetrahedra [38,39]. The Bi 4f and V 2p spectra remained unchanged after testing, confirming chemical and structural stability of the electrode during long-term PEC operation. The O 1s spectrum (Figure 7c) was deconvoluted into two main peaks: the dominant peak at 530.1 eV is attributed to lattice oxygen (O^{2-}), while the broader shoulder around 531.8 eV corresponds to surface hydroxy groups and oxygen vacancies [40-42]. Notably, post-PEC testing revealed an increase in the intensity of the oxygen vacancy-related component, suggesting the formation or activation of surface defects during prolonged photoelectrochemical operation. These oxygen vacancies are known to play a crucial role in enhancing charge separation and facilitating surface water oxidation reactions, thereby contributing to improved catalytic performance [43]. The post-stability XPS analysis also showed that $BiVO_4$(326) was chemically stable and that oxygen vacancies helped maintain its long-term photoelectrochemical activity.

Conclusion

This study demonstrates the successful synthesis of high-performance $BiVO_4$ photoanodes through controlled-intensity current electrodeposition, emphasizing the critical role of fabrication conditions on the structural, optical, and photoelectrochemical properties. XRD and Raman analyses confirmed the enhanced crystallinity and reduced lattice strain in the samples prepared under higher current densities and greater $VO(acac)_2$ volumes, which correlated with improved charge transport and reduced recombination losses. UV–vis absorption spectroscopy and FESEM imaging revealed that the optimized conditions led to better light-harvesting capabilities and enhanced surface area owing to finer particle morphologies and increased porosity of the photocatalysts. XPS analysis highlighted the presence of oxygen vacancies and well-defined chemical states, further contributing to the improved catalytic activity and charge separation. Photochemical measurements demonstrated that the $BiVO_4$(326) sample achieved the highest photocurrent density of 1.2 mA·cm^{-2} at 1.23 V vs RHE, a surface hole injection efficiency of 47%, and a peak IPCE of 18.1%, outperforming the

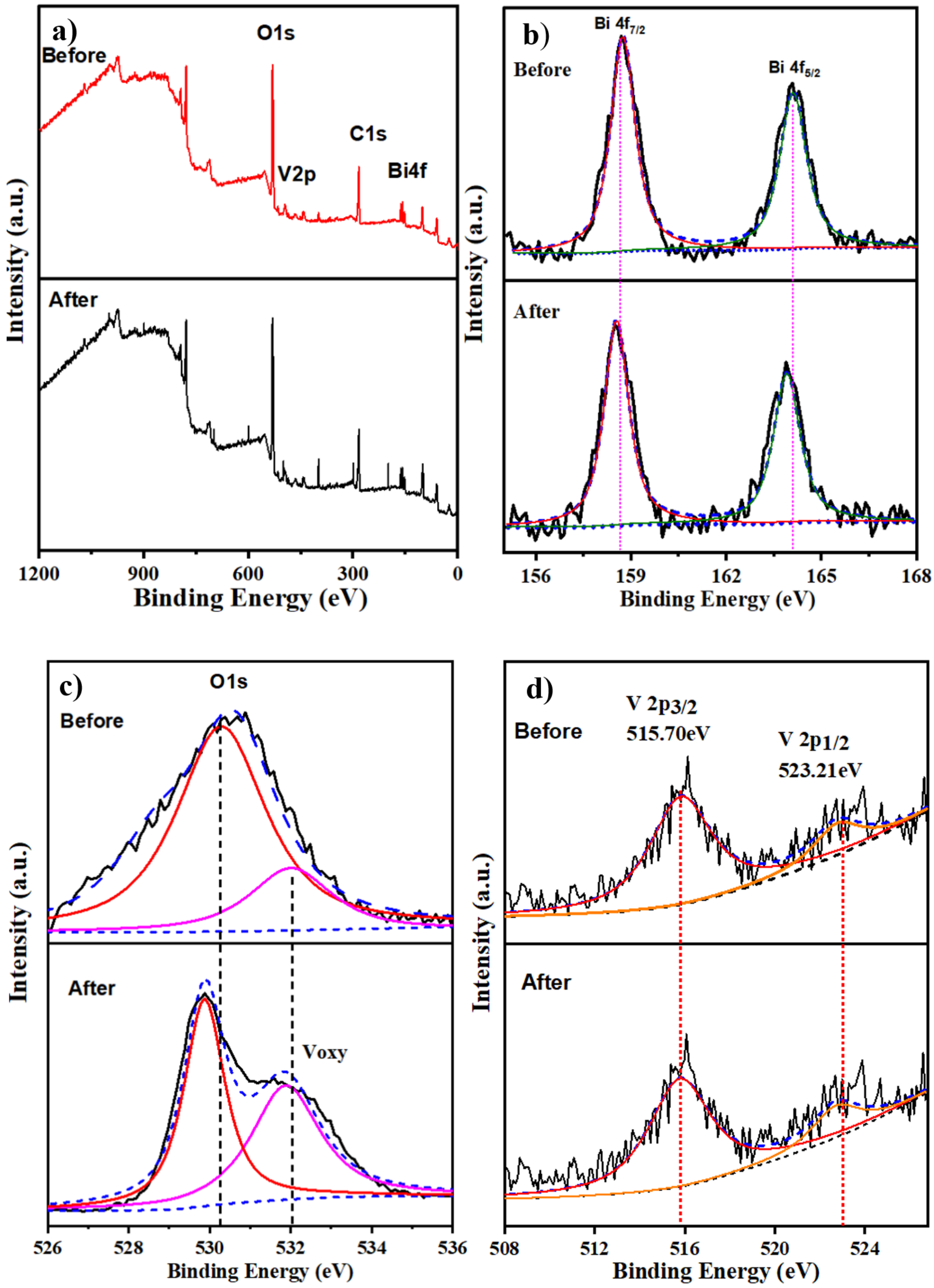

Figure 7: X-ray photoelectron spectroscopy (XPS) analysis of the $BiVO_4$(326) photoanode before and after PEC stability testing in 30 min (0.5 M Na_2SO_4). (a) XPS view scans of survey spectrum and high-resolution spectra of (b) Bi 4f, (c) O 1s, and (d) V 2p.

other samples. These results highlight the synergistic effects of an improved crystalline structure, optimized morphology, and enhanced electronic properties. This study provides a comprehensive understanding of the interplay between fabrication parameters and PEC performance, paving the way for efficient BiVO-based photoanodes for solar-driven water-splitting applications.

Conflict of Interest

The authors declare that they have no competing interests that could influence the work reported in this study.

Author Contributions

Huu Phuc Dang: conceptualization; methodology; project administration; writing – review & editing. Khanh Quang

Nguyen: data curation. Nguyen Thi Mai Tho: data curation; formal analysis. Tran Le: writing – original draft.

ORCID® iDs

Huu Phuc Dang - https://orcid.org/0000-0002-8982-0421
Tran Le - https://orcid.org/0000-0002-7762-4888

Data Availability Statement

Data generated and analyzed during this study is available from the corresponding author upon reasonable request.

References

1. Haji Yassin, S. N.; Sim, A. S. L.; Jennings, J. R. *Nano Mater. Sci.* **2020,** *2,* 227–234. doi:10.1016/j.nanoms.2019.10.003
2. Chong, M. N.; Jin, B.; Chow, C. W. K.; Saint, C. *Water Res.* **2010,** *44,* 2997–3027. doi:10.1016/j.watres.2010.02.039
3. Galán-González, A.; Sivan, A. K.; Hernández-Ferrer, J.; Bowen, L.; Di Mario, L.; Martelli, F.; Benito, A. M.; Maser, W. K.; Chaudhry, M. U.; Gallant, A.; Zeze, D. A.; Atkinson, D. *ACS Appl. Nano Mater.* **2020,** *3,* 7781–7788. doi:10.1021/acsanm.0c01325
4. Kim, K.; Moon, J. H. *ACS Appl. Mater. Interfaces* **2018,** *10,* 34238–34244. doi:10.1021/acsami.8b11241
5. Han, H.; Choi, H.; Mhin, S.; Hong, Y.-R.; Kim, K. M.; Kwon, J.; Ali, G.; Chung, K. Y.; Je, M.; Umh, H. N.; Lim, D.-H.; Davey, K.; Qiao, S.-Z.; Paik, U.; Song, T. *Energy Environ. Sci.* **2019,** *12,* 2443–2454. doi:10.1039/c9ee00950g
6. Eidsvåg, H.; Bentouba, S.; Vajeeston, P.; Yohi, S.; Velauthapillai, D. *Molecules* **2021,** *26,* 1687. doi:10.3390/molecules26061687
7. Hajra, P.; Kundu, S.; Maity, A.; Bhattacharya, C. *Chem. Eng. J.* **2019,** *374,* 1221–1230. doi:10.1016/j.cej.2019.06.014
8. Wang, J.; Ma, Q.; Wei, Y.; Guo, Y.; Li, H.; Song, H.; Sun, W.; Li, X. *Mol. Catal.* **2024,** *561,* 114154. doi:10.1016/j.mcat.2024.114154
9. Tian, K.; Jin, L.; Mahmood, A.; Yang, H.; An, P.; Zhang, J.; Ji, Y.; Li, Y.; Li, D.; Liu, S.; Yan, J. *Adv. Funct. Mater.* **2024,** *34,* 2410548. doi:10.1002/adfm.202410548
10. Trześniewski, B. J.; Smith, W. A. *J. Mater. Chem. A* **2016,** *4,* 2919–2926. doi:10.1039/c5ta04716a
11. Wang, S.; He, T.; Yun, J.-H.; Hu, Y.; Xiao, M.; Du, A.; Wang, L. *Adv. Funct. Mater.* **2018,** *28,* 1802685. doi:10.1002/adfm.201802685
12. Kang, B.; Bilal Hussain, M.; Cheng, X.; Peng, C.; Wang, Z. *J. Colloid Interface Sci.* **2022,** *626,* 146–155. doi:10.1016/j.jcis.2022.06.095
13. Seabold, J. A.; Choi, K.-S. *J. Am. Chem. Soc.* **2012,** *134,* 2186–2192. doi:10.1021/ja209001d
14. Smilyk, V. O.; Fomanyuk, S. S.; Kolbasov, G. Y.; Rusetskyi, I. A.; Vorobets, V. S. *Res. Chem. Intermed.* **2019,** *45,* 4149–4161. doi:10.1007/s11164-019-03897-y
15. He, Y.; Li, L.; Fan, W.; Zhang, C.; Leung, M. K. H. *J. Alloys Compd.* **2018,** *732,* 593–602. doi:10.1016/j.jallcom.2017.10.153
16. Liu, J.; Tajima, K.; Abdellaoui, I.; Islam, M. M.; Ikeda, S.; Sakurai, T. *Energies (Basel, Switz.)* **2021,** *14,* 2122. doi:10.3390/en14082122
17. Gong, H.; Freudenberg, N.; Nie, M.; van de Krol, R.; Ellmer, K. *AIP Adv.* **2016,** *6,* 045108. doi:10.1063/1.4947121
18. Kim, T. W.; Choi, K.-S. *Science* **2014,** *343,* 990–994. doi:10.1126/science.1246913
19. McDonald, K. J.; Choi, K.-S. *Energy Environ. Sci.* **2012,** *5,* 8553. doi:10.1039/c2ee22608a
20. Dolai, S.; Maiti, P.; Ghorai, A.; Bhunia, R.; Paul, P. K.; Ghosh, D. *ACS Appl. Mater. Interfaces* **2021,** *13,* 438–448. doi:10.1021/acsami.0c16972
21. Mohamed, N. A.; Arzaee, N. A.; Mohamad Noh, M. F.; Ismail, A. F.; Safaei, J.; Sagu, J. S.; Johan, M. R.; Mat Teridi, M. A. *Ceram. Int.* **2021,** *47,* 24227–24239. doi:10.1016/j.ceramint.2021.05.134
22. Li, Y.-l.; Liu, Y.; Hao, Y.-j.; Wang, X.-j.; Liu, R.-h.; Li, F.-t. *Mater. Des.* **2020,** *187,* 108379. doi:10.1016/j.matdes.2019.108379
23. Senasu, T.; Youngme, S.; Hemavibool, K.; Nanan, S. *J. Solid State Chem.* **2021,** *297,* 122088. doi:10.1016/j.jssc.2021.122088
24. Sundaresan, A.; Bhargavi, R.; Rangarajan, N.; Siddesh, U.; Rao, C. N. R. *Phys. Rev. B* **2006,** *74,* 161306. doi:10.1103/physrevb.74.161306
25. Arda, L. *J. Magn. Magn. Mater.* **2019,** *475,* 493–501. doi:10.1016/j.jmmm.2018.11.121
26. Zafar, Z.; Yi, S.; Li, J.; Li, C.; Zhu, Y.; Zada, A.; Yao, W.; Liu, Z.; Yue, X. *Energy Environ. Mater.* **2022,** *5,* 68–114. doi:10.1002/eem2.12171
27. Lopes, O. F.; Carvalho, K. T. G.; Macedo, G. K.; de Mendonça, V. R.; Avansi, W.; Ribeiro, C. *New J. Chem.* **2015,** *39,* 6231–6237. doi:10.1039/c5nj00984g
28. Peng, Z.; Su, Y.; Ennaji, I.; Khojastehnezhad, A.; Siaj, M. *Chem. Eng. J.* **2023,** *477,* 147082. doi:10.1016/j.cej.2023.147082
29. Pelissari, M. R. d. S.; Azevedo Neto, N. F.; Camargo, L. P.; Dall'Antonia, L. H. *Electrocatalysis* **2021,** *12,* 211–224. doi:10.1007/s12678-021-00641-2
30. Gao, Y.; Zhao, W.; Tian, Z.; Zhang, L.; Teng, Z.; Li, N.; Ge, L. *ACS Appl. Energy Mater.* **2023,** *6,* 4342–4353. doi:10.1021/acsaem.3c00326
31. Yang, J.; Tao, Z.; Zhao, Q.; Li, J.; Liu, G. *J. Alloys Compd.* **2025,** *1010,* 177461. doi:10.1016/j.jallcom.2024.177461
32. Chen, S.; Huang, D.; Xu, P.; Gong, X.; Xue, W.; Lei, L.; Deng, R.; Li, J.; Li, Z. *ACS Catal.* **2020,** *10,* 1024–1059. doi:10.1021/acscatal.9b03411
33. Tan, H. L.; Tahini, H. A.; Wen, X.; Wong, R. J.; Tan, X.; Iwase, A.; Kudo, A.; Amal, R.; Smith, S. C.; Ng, Y. H. *Small* **2016,** *12,* 5295–5302. doi:10.1002/smll.201601536
34. Fuentes-Camargo, I.; Carrera-Crespo, J. E.; Vazquez-Arenas, J.; Romero-Ibarra, I.; Rodríguez, J. L.; Lartundo-Rojas, L.; Cardoso-Martínez, J. *J. Phys. Chem. C* **2020,** *124,* 1421–1428. doi:10.1021/acs.jpcc.9b09898
35. Lu, Q.; Ding, L.; Li, J.; Wang, N.; Ji, M.; Wang, N.; Chang, K. *Int. J. Hydrogen Energy* **2024,** *71,* 1142–1150. doi:10.1016/j.ijhydene.2024.04.168
36. Radzi, A. A. S. M.; Safaei, J.; Teridi, M. A. M. *Nano-Struct. Nano-Objects* **2019,** *18,* 100274. doi:10.1016/j.nanoso.2019.100274
37. Bai, W.; Zhou, Y.; Peng, G.; Wang, J.; Li, A.; Corvini, P. F.-X. *Appl. Catal., B* **2022,** *315,* 121606. doi:10.1016/j.apcatb.2022.121606
38. Mohamed, N. A.; Safaei, J.; Ismail, A. F.; Khalid, M. N.; Mohd Jailani, M. F. A.; Noh, M. F. M.; Arzaee, N. A.; Zhou, D.; Sagu, J. S.; Teridi, M. A. M. *Mater. Res. Bull.* **2020,** *125,* 110779. doi:10.1016/j.materresbull.2020.110779
39. Guan, Y.; Gu, X.; Deng, Q.; Wang, S.; Li, Z.; Yan, S.; Zou, Z. *Inorg. Chem.* **2023,** *62,* 16919–16931. doi:10.1021/acs.inorgchem.3c02622
40. Xu, H.; Fan, W.; Zhao, Y.; Chen, B.; Gao, Y.; Chen, X.; Xu, D.; Shi, W. *Chem. Eng. J.* **2021,** *411,* 128480. doi:10.1016/j.cej.2021.128480

41. Wang, Y.; Zhang, J.; Balogun, M.-S.; Tong, Y.; Huang, Y. *Mater. Today Sustainability* **2022,** *18,* 100118. doi:10.1016/j.mtsust.2022.100118
42. Wu, J.-M.; Chen, Y.; Pan, L.; Wang, P.; Cui, Y.; Kong, D.; Wang, L.; Zhang, X.; Zou, J.-J. *Appl. Catal., B* **2018,** *221,* 187–195. doi:10.1016/j.apcatb.2017.09.031
43. Fernández-Climent, R.; Giménez, S.; García-Tecedor, M. *Sustainable Energy Fuels* **2020,** *4,* 5916–5926. doi:10.1039/d0se01305f

License and Terms

The definitive version of this article is the electronic one which can be found at:
https://doi.org/10.3762/bjnano.16.94